Development of the first compact model for ultra-fast UTC (Uni-travelling carrier) photodiodes towards monolithic integration of photonic and nanoelectronic technologies

Djeber Guendouz

▶ **To cite this version:**

Djeber Guendouz. Development of the first compact model for ultra-fast UTC (Uni-travelling carrier) photodiodes towards monolithic integration of photonic and nanoelectronic technologies. Electronics. Université de Bordeaux, 2022. English. NNT : 2022BORD0296 . tel-03892817

HAL Id: tel-03892817

https://theses.hal.science/tel-03892817

Submitted on 10 Dec 2022

HAL is a multi-disciplinary open access archive for the deposit and dissemination of scientific research documents, whether they are published or not. The documents may come from teaching and research institutions in France or abroad, or from public or private research centers.

L'archive ouverte pluridisciplinaire **HAL**, est destinée au dépôt et à la diffusion de documents scientifiques de niveau recherche, publiés ou non, émanant des établissements d'enseignement et de recherche français ou étrangers, des laboratoires publics ou privés.

université de BORDEAUX

THESE PRESENTEE POUR OBTENIR
LE GRADE DE

DOCTEUR DE L'UNIVERSITE DE BORDEAUX

ECOLE DOCTORALE DES SCIENCES PHYSIQUES ET DE L'INGENIEUR

SPECIALITE ELECTRONIQUE

Présentée et soutenue publiquement par

Djeber GUENDOUZ

Le 8 novembre 2022

Development of the first compact model for ultra-fast UTC (Uni-travelling carrier) photodiodes towards monolithic integration of photonic and nanoelectronic technologies

Directrice de thèse : **Cristell MANEUX**

Co-directeur : **Patrick MOUNAIX**

Co-encadrant : **Chhandak MUKHERJEE**

Membres du jury :

Mme. MANEUX Cristell	Professeur, Université de Bordeaux.	Directrice de thèse
M. MOUNAIX Patrick	Directeur de recherche, IMS, Université de Bordeaux.	Co-directeur
M. MUKHERJEE Chhandak	Chargé de recherche, IMS, Université de Bordeaux.	Co-encadrant
M. KALLFASS Ingmar	Professeur, Université de Stuttgart.	Rapporteur
M. ROZEAU Olivier	Docteur, Ingénieur de recherche, CEA-Leti.	Rapporteur
M. RENAUD Cyril	Professeur, Université Collège de Londres.	Président
M. CAILLAUD Christophe	Docteur, Ingénieur de recherche, IIIV-Lab.	Examinateur
Mme. DENG Marina	Maître de conférences, Université de Bordeaux.	Examinateur
M. BOLOGNESI Colombo	Professeur, ETH Zürich.	Invité

Université de Bordeaux
Laboratoire de l'Intégration du Matériau au Systèmes
UMR CNRS 5218, F-33400 Talence, France

Abstract - EN

In the current era of information technology, we are witnessing a tremendous increase in global internet and mobile traffic. Continuous innovation in optical communication technologies have contributed significantly to the enhancement of high-speed data traffic. However, the continuous demand for bandwidth requires the designing and implementation of new circuits and systems capable of supporting the rising need of data traffic. In wireless communications, traditional radio frequency communication technologies face significant challenges to meet the increase in bandwidth requirements. Hence, the higher RF bands, including millimeter wave (0.3-100 GHz) and terahertz (0.1-10 THz), which offer greater bandwidths, must be exploited to support future ultra-fast wireless communication systems to support the expected data traffic. High bandwidth receivers with less complex architectures, are hence essential in optical communications. Efficient, compact, low-power transmitters and receivers will be key elements in the implementation of high-performance wireless communication systems. A viable and efficient solution to this challenges comes in the form of monolithic optoelectronic integrated circuits (OEICs). Uni-Traveling Carrier Photodiodes (UTC-PDs) are key components for OEICs, and have been widely studied for ultrafast optoelectronic applications. High performances have been reported, demonstrating bandwidths of over 600 GHz. As a first step towards the development of OEI circuits and systems, a unified modelling and co-designing solution must be implemented. In this context, we propose a scalable, compact and multi-physics model for the UTC-PDs. The model is written in Verilog-A and is compatible with existing electronic circuit design methodology/tool/flow. The model is developed based on the physics of carrier transport in the UTC-PDs. To validate the model, we performed electro-optical characterizations on the UTC-PDs. On-wafer optoelectronic characterizations were performed at the IMS laboratory for the first time, thanks to the measurement setup that we developed during this thesis. The complete validation of the compact model has been performed against measurements under a wide range of operating conditions (bias and frequency) on UTC-PD technologies on InP substrates provided by three different foundries. We have also developed de-embedding methods for the test structures and a parameter extraction flow for the proposed UTC-PD compact model. The compact model has been validated first against DC and RF on-wafer measurements up to 67 GHz and 110 GHz without optical illumination. Next, responsivity under different optical powers and bandwidth measurements up to 67 GHz, were performed on UTC-PDs and were also validated against the compact model simulations. This model has demonstrated excellent versatility and scalability for the three types of UTC-PDs studied in this work, for several geometries and over a wide range of bias conditions. The proposed modelling framework is comprehensive, accurate and physics-based, while remaining compatible with the existing electronic circuit design infrastructure.

***Keywords**: optical communication, wireless communication, millimeter waves (mm-Waves), Terahertz (THz), optoelectronic integrated circuits (OEICs), Uni-Traveling Carrier Photodiodes (UTC-PDs), compact modelling, circuit design and on-wafer RF characterization, S-parameter measurements.*

Résumé - FR

À l'ère des technologies de l'information, nous assistons à une augmentation spectaculaire du trafic Internet et mobile mondial. L'innovation dans les technologies de communication optique a contribué de manière significative à la transmission de données à haut débit. Cependant, la demande continue de bande passante nécessite la conception et la réalisation de nouveaux circuits et systèmes capables de supporter la demande croissante de trafic de données. En ce qui concerne les communications sans fil, les technologies traditionnelles de communication par radiofréquence sont confrontées à des défis importants pour répondre à l'augmentation des besoins en bande passante. Les bandes RF supérieures, notamment les ondes millimétriques (0,3-100 GHz) et les Térahertz (0,1-10 THz) offrent des largeurs de bande plus importantes et doivent être exploitées pour prendre en charge les communications sans fil ultrarapides. Les futurs systèmes de communication devront supporter le trafic de données attendu. Des récepteurs à large bande passante et à l'architecture moins complexe sont donc essentiels dans les communications optiques. Des émetteurs et des récepteurs efficaces, compacts et de faible consommation seront un élément clé de la mise en œuvre de systèmes de communication sans fil à haute performance. Les circuits optoélectroniques intégrés (COEIs) de façon monolithiques constituent une solution viable et efficace à ce défi. Dans les COEIs, les photodiodes à porteur unique (UTC-PD) représentent des composants clés qui ont été largement étudiés pour les applications optoélectroniques ultrarapides. Des performances élevées ont été rapportées, démontrant des bandes passantes de plus de 600 GHz. Comme première étape vers le développement de circuits et de systèmes OEIC, une solution unifiée de modélisation et de co-conception doit être mise en œuvre. Dans cette perspective, nous proposons un modèle évolutif, compact et multi-physique pour l'UTC-PD. Le modèle est écrit en Verilog-A et est compatible avec la méthodologie/outil/flux de conception de circuits électroniques existants. Le modèle est développé sur la base des équations de transport des porteurs de charges dans l'UTC-PD. Afin de valider le modèle, nous avons effectué des caractérisations électro-optiques sur les UTC-PDs. La caractérisation optoélectronique on-wafer a été réalisée pour la première fois dans le laboratoire IMS, grâce à la mise en œuvre d'un banc de mesure que nous avons développé durant cette thèse. La validation complète du modèle compact par rapport aux mesures effectuées sur technologies UTC-PD de trois fondeurs différents dans une large gamme de conditions de fonctionnement (polarisation et fréquence) a été réalisée. Des méthodes de *de-embedding* adaptées et un flux d'extraction des paramètres du modèle compact UTC-PD proposé ont été étudiés. Les comportements DC et RF, sans illumination, de ce modèle compact ont été validés par des mesures sur plaquette jusqu'à 67 GHz et 110 GHz sur trois technologies UTC-PD développées sur des substrats InP. De même, des mesures de largeur de bande, jusqu'à 67 GHz, ont été effectuées et ont également été validées par rapport à la simulation du modèle compact. Ce modèle a démontré une excellente polyvalence et une évolutivité pour les trois types d'UTC-PDs étudiées, pour plusieurs géométries et sur une large gamme de conditions de polarisation. Le cadre de modélisation

proposé est complet, précis et basé sur la physique, tout en étant compatible avec l'infrastructure de conception de circuits électroniques existante.

Mots clés: communication optique, communication sans fil, ondes millimétriques (mm-Waves), Térahertz (THz), circuits optoélectronique intégré (COEIs), photodiodes à transport unipolaire (UTC-PDs), modélisation compacte, conception de circuit and caractérisation RF sur plaquette, mesures de paramètres S.

Acknowledgments

Je tiens tout d'abord à remercier ma directrice de thèse, le professeur Cristell MANEUX, mon co-directeur de thèse Dr. Patrick MOUNAIX et mon co-encadrant de thèse Dr. Chhandak MUKHERJEE, de m'avoir donné l'opportunité de travailler sur un sujet aussi intéressant. Je leur adresse également mes remerciements pour leurs efforts et leur soutien tout au long de cette aventure. Sans eux, cette thèse n'aurait pas vu le jour.

Je tiens également à remercier le Dr. Olivier ROZEAU et le professeur Ingmar KALLFASS pour avoir accepté de rapporter ce travail de thèse, ainsi que le professeur Cyril RENAUD, le Dr. Christophe CAILLAUD et le professeur Colombo BOLOGNESI pour avoir accepté d'examiner ce travail.

Je tiens à remercier Dr. Marina DENG qui a contribué à la réussite de cette thèse. Je la remercie également de m'avoir toujours apporté une énergie positive.

Je remercie Magali DE MATOS, l'ingénieur de la plateforme NANOCOM pour les caractérisations RF et je la remercie de partager son expertise. Je remercie également Frédéric FAUQUET, l'ingénieur de la plateforme ATLAS pour son aide dans la mise en place du banc de mesure, ainsi que pour sa gentillesse, son soutien et ses encouragements.

Un remerciement spécial à mes amis et collègues de bureau : Marine, Barnabé, Adrien, Quentin, Jean-Baptiste, Matthieu, Florent, Thomas, Margaux, Ruben, Mingming, Justin, Yifan, Houssem, Bixente, Lucas et Marco. Vous êtes l'une des raisons pour lesquelles j'ai aimé mon travail à l’IMS. Cela a été un grand plaisir. Je les remercie pour m'avoir encouragé et soutenu chaque fois que j'en avais besoin. Je les remercie aussi pour toutes les superbes activités extraprofessionnelles.

Je remercie tous mes amis, pour leur soutien tout au long de cette thèse, en particulier Oussama et Mohamed Sadek pour leur amitié inconditionnelle, et aussi Frédéric, Sadia, Hicham, Abderrahmane, Khaled, Anis, Ibrahim, Younes, Mohamed, Oussama et Younes.

Enfin, je remercie toute ma famille. En particulier mes parents, mes frères et ma sœur : Amine, Fatima, Youcef et Abdelbar. Je les remercie pour leurs soutiens constants durant les trois années de mon travail de doctorat.

Contents

List of Acronyms

ADC Analog Digital Converter

BER Bit Error Rate

BiCMOS Bipolar Complementary Metal Oxide Semiconductor

BPSK Binary Phase Shift Keying

CMOS Complementary Metal Oxide Semiconductor

CPW CoPlanar Waveguide

DFB Distributed Feedback Laser

DSP Digital Signal Processing

DUT Device Under Test

EOS Electro-Optical Sampling

FC/APC Ferrule Connector/Angled Physical Contact

FDTD Finite Difference Time Domain

GbE Gigabit Ethernet

GSG Ground Signal Ground

HiCUM High Current Model

IC Integrated Circuit

IoE Internet of Everything

LO Local Oscillator

LPF Low-pass Filter

LRRM Load Reflect Match

LTLM Linear Transfer Length Method

LWP Light Wave Probe

MZM Mach-Zehnder Modulator

OEIC OptoElecronic Integrated Circuit

OOK On-Off Keying

PAM Pulse Amplitude Modulation

PIC Photonic Integrated Circuit

QAM Quadrature Amplitude Modulation

QPSK Quadrature Phase Shift Keying

RMS Root Mean Square

SCR Space Charge Region

SEM Scanning Electron Microscopy

SMU Source Measure Unit

SNR Signal to Noise Ratio

SOA Semiconductor Optical Amplifier

SOI Silicon On Insulator

SOLT Short Open Load Thru

SPICE Simulation Program with Integrated Circuit Emphasis

TIA Transimpedance Amplifier

VCCS Voltage Controlled Current Source

VNA Vector Network Analyzer

WDM Wavelength Division Multiplexing

List of Tables

List of Figures

Introduction

Motivation

In the era of Internet of Everything (IoE), we are experiencing rapid global surge in internet and mobile traffic. In the internet world, the continual emergence of new applications such as multiple video streaming platforms, online cloud storage, and even the predicted Metaverse, where the physical, virtual, and augmented realities merge, are extremely data-intensive.

The optical fiber technology has been in use since the 1980s for long distance and very high speed data transmissions [1], and is now widely used in short-distance communication networks as well. Over the past three decades, this technology has immensely contributed to the development of optoelectronic systems (photonic and electronic components assembled together), paving the way for integrated optical transceivers and high-speed optical modulators capable of meeting the growing demand in data rate and bandwidth. Communication standards in optical networks have evolved from 10 to 100 Gigabit Ethernet (GbE) over the past 30 years [2]. In 2017, the 400 GbE standard was approved by the IEEE P802.3bs committee and is expected to be adopted rapidly in the next few years [3].

However, the increasing demand for bandwidth requires the design and fabrication of new circuits and systems capable of supporting such a large flow of information. Monolithically integrated optoelectronic circuits (OEIC) are considered as one of the promising solutions to address the upcoming challenges related to the evolution of information technologies. Indeed, monolithic integration of electronic and photonic devices allows for the shortest possible interconnections, thus minimizing the distance and electronic propagation losses within the device, especially at very high operating frequencies, and achieves better performances over hybrid circuits [4]. Co-integration also reduces the circuit sizes and manufacturing costs [5].

In the world of wireless communication, radio communication is predominant. Due to the growth of data traffic, radio and optical communications have converged although they remain two distinct means of communication, mainly due to their relative positions on the electromagnetic spectrum [6]. Currently, there is an observable transition in radio technologies from millimeter (mm-Waves) to Terahertz (THz) waves, as they offer very high data rate traffic at large available bandwidths (tens to hundreds of GHz). Depending on the application, the appropriate carrier frequency or the frequency band is chosen [7].

The expected data rate for wireless communications in mainstream market is expected to reach 100 Gbps and higher in the coming years (see Figure 0.1) [8], which requires larger bandwidths. Obviously, the use of a carrier frequency in the THz range (0.1-10 THz) will be mandatory when the minimum bandwidth reaches several tens of GHz. Moreover, a large number of discrete terminals and a dense mesh of small radio cells are required to provide ubiquitous, broadband wireless access. All of these requirements can be met on one hand by

using of fiber-optic radio (RoF) techniques, which involve the use of optical devices and techniques to generate, modulate, and transmit mm-Waves and THz signals, and on the other hand by monolithic OEICs that achieve optimal performances compared to hybrid circuits/systems.

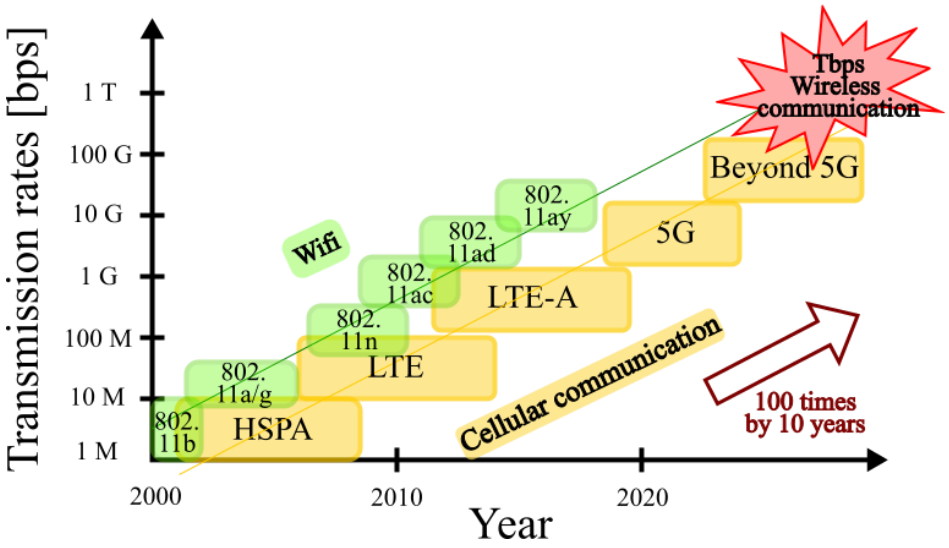

Figure 0.1. Evolutionary trend of wireless communication technologies and the transmission rate [8].

Monolithic OEICs are, therefore, a key element for future communication technologies, either for optical fiber communication or for very high speed wireless communication. The design and simulation of monolithic OEICs and systems heavily rely on the accuracy of compact models for the components of these circuits [9]. Therefore, it is essential to have computationally efficient and physics-based compact models that are compatible with existing software tools and SPICE design flow. With that in mind, we have started developing a compact modeling framework for photonic devices complementary to electronic device compact models. In this context, one of the major and timely contributions this thesis makes to the field of integrated optoelectronic circuit design is to propose a comprehensive compact model for the uni-traveling carrier photodiodes (UTC-PD), a key component in OEICs.

Overview of the thesis

This thesis is organized in four chapters; as a context, we first review the challenges and design perspectives for advanced communication technologies, then we describe the design concept of monolithic OEICs and their potential to meet the challenges of future communication technologies. Next, we investigate different UTC-PD technologies and present the associated multi-scale compact modelling framework and finally we discuss the performances achieved by these devices along with experimental results and model validation.

The **first chapter** of this thesis starts with a general discussion on the progresses made in optical and wireless communication. Next, the principal challenges are discussed and the notable demonstrations of new concepts and technologies for photonics and OEICs are presented. Finally, potential technologies such as monolithic OEICs are detailed and discussed.

The **second chapter** starts with a brief history of the development of UTC-PDs, followed by a discussion on the performances of this technology compared to other photodiodes used in communication and the main advancements achieved for this device. Next, we discuss the fundamental modelling techniques for this photonic component and the importance of SPICE compact modelling for the design of OEICs. Finally, the theoretical basis of our compact model and its representation by an electrical equivalent circuit and formulation of model equations are detailed.

The **third chapter** is devoted to the description of the electro-optical measurement setup that has been developed during the course of this work. An overview of the equipment used are provided. Finally, a summary of the characterization and extraction protocols for the device parameters is presented.

The **fourth chapter** presents the results obtained to validate the compact model against experimental data from different UTC-PD technologies under test. A parameter extraction protocol has been proposed and followed in order to ensure an accurate extraction of the intrinsic parameters of the device. The first step is focused on applying de-embedding methods that we have proposed and that are better adapted in our case compared to the techniques reported in the literature. The intrinsic device data are then used to extract the compact model parameters. Finally, the chapter concludes with the presentation of extensive validation of the developed compact model, particularly for the principal figures of merit, the dark current and the bandwidth, of the studied UTC-PDs.

Finally the manuscript is concluded by a summary of the overall efforts of this thesis. Prospects for future work are also discussed.

Chapter 1: Photodiodes in communication systems

This chapter is divided into two main parts that categorize modern photonic systems, communication networks using optical link and wireless networks. In the section detailing the optical link, we focus on the configuration of an optical link and more specifically on the front end of the receiver module that include the photodiode (PD) and the Transimpedance amplifier (TIA). We also discuss the potential for monolithic integration of these devices to take advantage of the maximum potential of the optical fiber technology. We conclude this part by discussing prospects of OEICs based on InP substrate.

The second part is dedicated to wireless communication systems and specifically to the future vision of deploying very high speed communication in the mm-Wave and THz range. In this section we present the state-of-the-art on wireless links in the mm-Wave and THz range. We conclude this section by presenting a few notable demonstrations of integrated optoelectronic circuits for wireless communication along with their prospects for potential monolithic integration.

1.1 High speed optical communication

The number of applications and services is constantly increasing in today's ever evolving domain of information technology. Big Data, multiple video streaming platforms and online cloud storage are just a few of the many applications that require high data rates while ensuring low power consumption. To keep up with the ever-growing need in global data traffic, communication standards have evolved from 10 Gbps data transfer systems to 400 Gbps and are looking to go even higher in the coming years. Supporting and managing such dense data traffic have been made possible by the fiber-based interconnection and transmission systems developed over the years. In this section, we first present the basics of optical data transmission. Then, we focus on the data reception module i.e. the receiver, and particularly on its front end which is composed of the PD and TIA. Finally, we discuss on pertinent demonstrations of monolithic OEIC receivers and present the perspectives.

1.1.1 Optical transmission

1.1.1.1 Generic system

Optical links using fiber optics have dominated short- and long-distance interconnections because of their high bandwidth, immunity to electromagnetic interference and low attenuation over long distances.

Figure 1.1 shows a basic optical communication link for the transmission and reception of information. In the transmission part, electrical data is converted into data stream by a Mach-

Zehnder Modulator (MZM), carried on an optical carrier generated by a laser. The optical information is then transported through a fiber in the case of long-distance communications and for data centers, or through waveguides in the case of very short-range interconnections, e.g. from chip to chip or intra-chip communications.

In the receiver part, a photodetector (photodiode, for example) detects and converts the optical data into an equivalent electrical current. A trans-impedance amplifier (TIA) amplifies and converts this current into a voltage signal to be processed next.

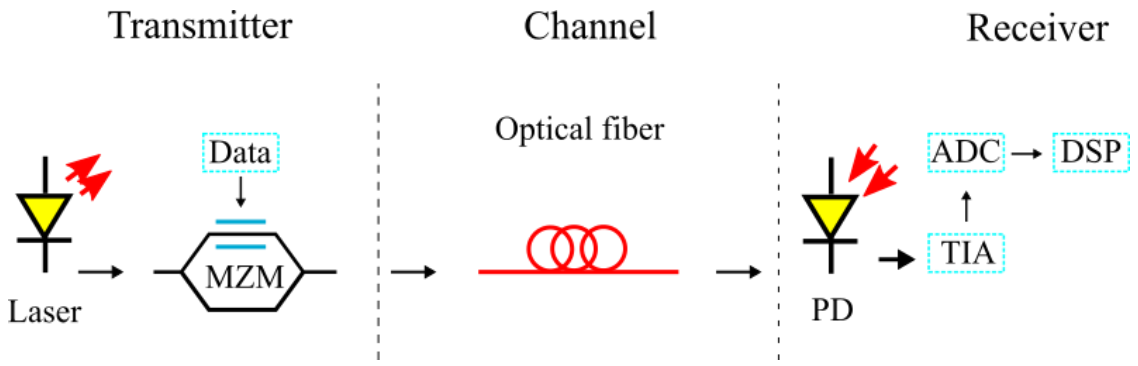

Figure 1.1. Schematic of an optical fiber link.

The sensitivity of an optical receiver is the minimum incident optical power required at the receiver for the decision circuits to recover data at a reference bit error rate (BER) and it is one of the most important figures of merit. The bit error rate is a fraction of the number of bits that were incorrectly decoded. In general, a BER of 10^{-12} is desired in optical receivers [10].

In the example shown in Figure 1.1, the transmitting and receiving operations process serial data in a single flow, for example at 10 Gbps. To transmit higher data rates in the C-band range (1530-1565 nm), which has a bandwidth of 4 THz, wavelength division multiplexing technology has been developed (Figure 1.2). This technological feature is used possibly partly due to the very low attenuation (≈0.2 dB/km) of optical fibers over a very wide bandwidth, and partly due to the fact that the bandwidth of an optical fiber is much higher than that of an optoelectronic devices [10].

Wavelength division multiplexing (WDM) technology allows the transmission of many signals (up to a hundred [11]) in the same fiber by assigning a specific wavelength (a channel)

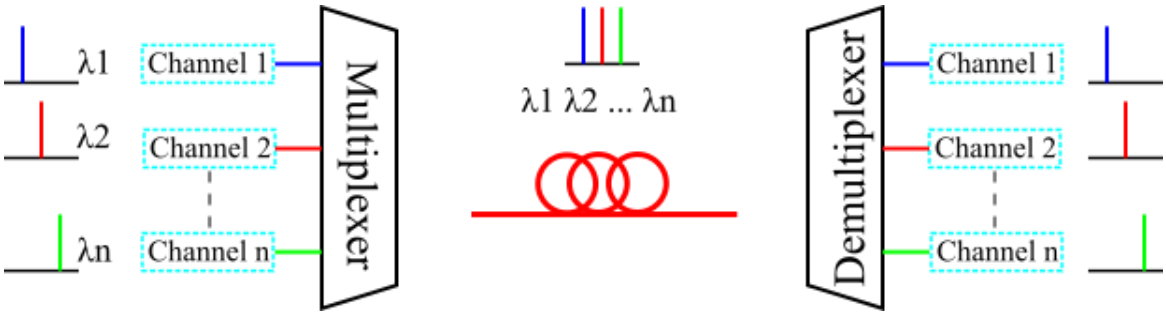

Figure 1.2. Schematic of an optical fiber transmission using wavelength division multiplexing technology.

to each signal. Very high data rates (several Tbit/s) can thus be transmitted over distances of more than a thousand kilometers in a single fiber.

1.1.1.2 Modulation Formats

In digital telecommunication systems, information is coded in the form of symbols. Depending on the modulation format used, a symbol will encode one or more bits. The rate which devices or circuits can support is expressed in bauds (or symbols/s), and can thus be different from the rate of transported information which is expressed in bit/s [10].

Binary On-Off Keying (OOK) modulation is the simplest and most widely used format in short-haul fiber optic data communication systems. It imposes less stringent signal-to-noise ratio requirements than other higher modulation format orders, and thus lower noise requirements. OOK is simply a binary method of signaling, with "0" generally corresponding to no signal or low optical power, and "1" corresponding to a high signal power or a signal pulse. However, this means that the bit rate is the same as the baud rate. Therefore, for data rates of 100 Gbps, a bandwidth of about 50 GHz is required, which can be very difficult to achieve due to bandwidth limitations. In order to transmit more data in a limited bandwidth canal, digital M-ary modulation schemes are thereby used, and the most common of these schemes is 4-levels pulse amplitude modulation (PAM-4). Compared to OOK modulation (which can be considered as PAM-2 modulation), PAM-4 modulation transmits twice the information for the same bandwidth, however, sacrificing the signal-to-noise ratio (SNR) and at the cost of increased complexity of the coding and decoding blocks in the transceivers.

The variation in the phase of the signal can also be used to achieve the same data rate as OOK modulation, by coding the information on two opposite phase states of the light (0/π).

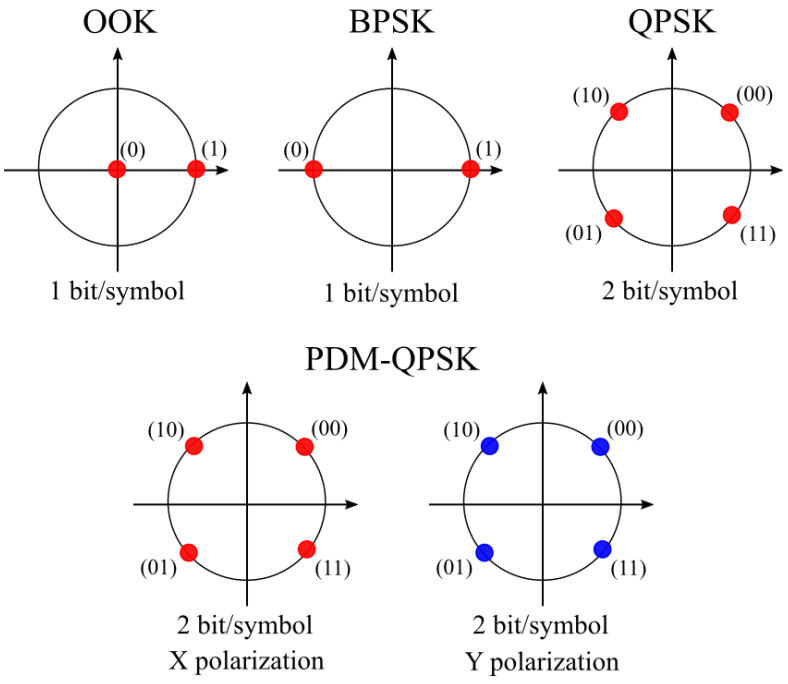

Figure 1.3. Illustration of the main modulation formats with the associated constellation.

This technique is called Binary Phase Shift Keying (BPSK) modulation. It is possible to transmit double the information per symbol of a light pulse, by combining two orthogonal BPSK signals in phase. It is then possible to code binary states using four states composed of phases (for example 45°, 135°, -45° and -135°). This is called Quadrature Phase Shift Keying (QPSK), where each state carries the information of 2 bits (1 per BPSK signal). The various states can be visualized as complex numbers on a constellation diagram, in which the x-axis represents the real component (I, "In Phase"), and y-axis stands for the imaginary component (Q, "Quadrature") [12]. This constellation is then representative of the modulation of a signal as illustrated in Figure 1.3.

One of the evolved versions of this format is the modulation in phase multiplexed quadrature or Polarization-Division Multiplexing Quadrature Phase-Shift Keying (PDM-QPSK), formed by the recombination of two QPSK signals, depending on perpendicular polarizations of the modes TE or TM (Transverse Electric or Transverse Magnetic). In the output of such a modulator, one obtains a symbol constellation (Baud) containing 4 bits of information (2 for each QPSK signal). Thus, for a speed of modulation of 25 Gbaud, one obtains an effective flow of 100 Gbps.

By combining two orthogonal 4-levels modulations, it is possible to generate even more binary states. The constellation obtained then comprises 2^4=16 states, which makes it possible to code 4 bits per symbol. This modulation format is thus called 16-QAM, for Quadrature Amplitude Modulation. Additionally, the number of states can be increased to 32, or even 64, by multiplying the modulation levels.

1.1.2 Toward monolithic OEIC: receivers

The continuous increase in data traffic has created an increasing demand for bandwidth. Ethernet throughput has evolved at a very rapid rate, from 10 to 100 gigabits Ethernet (100 GbE), over the past 30 years [13]. In 2017, the 400 GbE standard was approved by the IEEE P802.3bs committee and is expected to be rapidly adopted in the next few years [3]. Depending on the interface link (client and or data center interface), the adopted architecture of the transmitters and receivers and modulation formats can be more or less complex.

Since this PhD thesis focuses mainly on the compact modelling and characterization of photodiodes and more precisely of UTC-PDs, we have chosen to emphasize on their implementation for designing OEICs such as optical receivers. With that in mind, in what follows, we present and discuss a few demonstrations of the hybrid integration of PD and TIA (receiver front end) and then we illustrate their potential for monolithic integration.

1.1.2.1 Hybrid integrated receivers

The receivers can be fabricated using a III-V technology platform based on an InP substrate, the CMOS or BiCMOS platform on a silicon substrate or through hybrid integration, involving PDs on III-V substrate along with TIA and other electronic devices built on CMOS or BiCMOS platform. These basic modules can be integrated together in several ways. Historically, these devices are designed and optimized independently before being assembled into the final circuit. For example, in the optical receiver, the PD and TIA can be fabricated individually and then assembled by wire bonding (Figure 1.4) or flip chips. Thus, the photonic and electronic devices are connected electrically by wire bonds or flip chips [9], [14].

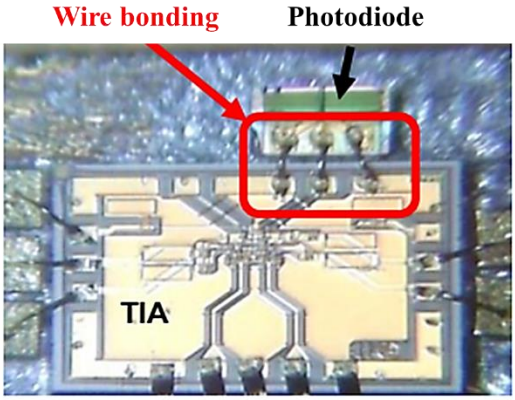

Figure 1.4. Microphotograph of an optical receiver where the photonic (PD) and the electronic (TIA) blocks are assembled by wire bonding [9].

Hybrid assembly has the advantage of optimizing the performance of each component through the selection of appropriate semiconductor platforms for manufacturing. However, their limitations become apparent when bit rate exceeds 50 Gbps, caused by parasitic interconnections [15]. At higher data rates, monolithic integration, where the photonic, analog electronic, and the digital receiver components are fabricated on a single substrate in the same process flow, appears to be the most promising approach. We discuss it in more details in the next section with demonstrations reported in the literature.

1.1.2.2 Monolithic integrated receiver

Monolithic integration of electronic and photonic devices provides the shortest possible interconnects, resulting in better signal quality and better performance over hybrid circuits. Co-integration also reduces circuit size and manufacturing cost. Monolithic integration eliminates capacitive, resistive, and inductive parasitic interconnects that impair performance and add complexity in the final stages of IC design where careful parasitic modelling must be considered [16].

The intrinsic drawback of monolithic integration is its poor ability to optimize the performance of each device independently. For example, the fabrication process used for electronics may not be optimal for photonic devices.

a. InP platform

Photonic integrated circuits (PICs) are mainly based on III-V semiconductor materials on InP substrate platform, used especially because of the direct bandgap material that are essential to achieve laser sources and high efficiency optical amplifiers. For photodetectors, $In_xGa_{1-x}As$ alloy demonstrates strong optical absorption at telecommunication wavelengths. Moreover, the high electron velocity in InP enables high sensitivity and wide bandwidth photodetectors (PD). InGaAsP and InGaAlAs quaternary alloys, epitaxially grown on InP substrates, permit flexible bandgap engineering for telecommunication wavelengths, allowing active/passive integration on a single chip. They also provide efficient modulation of optical signals based on electro-optical and free carrier effects [17].

Generic integration platforms based on InP have been proposed and developed over the last decade to reduce the cost and throughput time for developing PICs. Also, generic InP-based foundries based on industrial series of multi-project wafers have been established in Europe, offering low-cost access to the fabrication of application-specific PICs [17].

The monolithic integration of p-i-n PDs and transistors (HEMT, HBT) in III-V on InP substrates dates back to the mid 1990's [18]–[21]. For instance, in 1996 Bell labs reported a monolithic integrated receiver on an Fe:InP substrate [15]. Figure 1.5 shows the schematic of the cross section of that receiver. It consists of a p-i-n PD connected to an n-p-n HBT which operates as a TIA. In this configuration, light is injected from beneath through the substrate. As shown in Figure 1.5, the p-i-n PD and the HBT share the first three layers above the substrate. Specifically, they share the base-collector junction. The Bell Labs group reported a 3 dB bandwidth of 10.4 GHz with a total power dissipation of 92 mW.

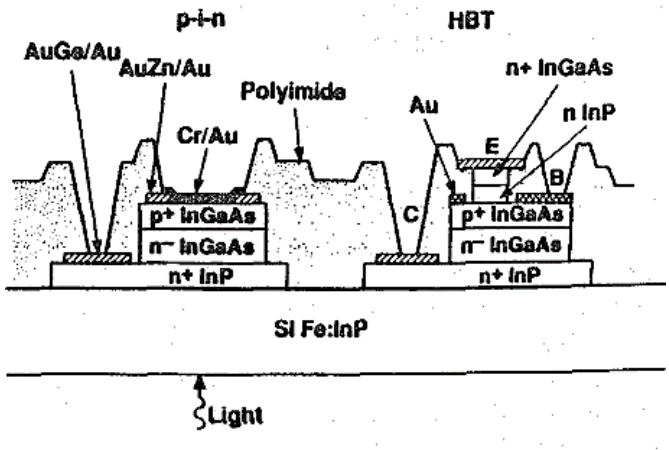

Figure 1.5. Cross sectional view of a monolithic OEIC composed of p-i-n PD and HBT [15].

Works on monolithic integration of InP-based receivers thus continued until the early 2000s. A fully packaged optical receiver module based on monolithic integration of single p-i-n photodiodes and heterojunction bipolar transistors (HBTs) was also reported [22]. In 2000, the optical receiver module demonstrated a clear eye diagram for data rates of 40 Gbps at a wavelength of 1550 nm [22].

Since these achievements, however, research in monolithic integration on InP platform has somewhat considerably slowed down. This could be due to several possible reasons: (i) the existing need for data throughput is already met by the more mature CMOS and BiCMOS technologies, which offer high efficiency and higher integration densities, hence the growing academic and industrial interest in silicon photonics, a competing electro-photonic integration technology that will be discussed in the next section; (ii) The performances of devices, such as a photodetector or a TIA, are often sacrificed when implemented using a single and common fabrication process. Therefore, a hybrid assembly by wire or flip chip interconnections is preferred, which is currently being used in the industry operating at 25 Gbps [23].

With the tremendous increase in data traffic, it has thus become imperative to re-evaluate the possibility of reviving monolithic integration of electronics and photonics based on III-V materials.

b. Silicon platform

Due to the indirect band gap of group IV semiconductors (silicon and germanium), it is challenging to build true monolithic electro-photonic circuits, especially when it comes to active devices (lasers and amplifiers). However, when it comes to passive photonic devices, the integration of Germanium (Ge) in the CMOS process enables photodiodes with responsivities as attractive as those of III-V-based photodetectors. This is because Ge has excellent absorption for the visible to near infrared wavelengths. Additionally, it exhibits higher electron and hole mobilities compared to silicon.

The advancements in the field of Ge on Si integration have been driven by the development of processes that allow epitaxial growth of Ge on Si, despite the 4.2% lattice mismatch between the two materials. SiGe buffer layers and annealing processes are some of the ways in which dislocation densities can be reduced [24]. Despite this, there are still a few drawbacks of integrating Ge photodetectors into a CMOS process, such as thermionic emission, which contributes to a relatively high dark current density resulting in high noise level of the photodetectors [25].

Monolithic integration of photonics with silicon has been sought for some time, and most of the related works have been done based on CMOS technologies [26], [27]. However, CMOS technologies do not seem to be the best choice when it comes to the base electronics that can ideally meet the requirements of future communication systems in terms of throughput and RF power. Beyond 100 Gbps systems, data rates in excess of 50 GBd are required for 400 Gbps transceivers. High-speed transistors are therefore a prerequisite for high-performance ePIC technologies [28].

Advanced SiGe heterojunction bipolar transistors (HBTs) outperform CMOS transistors in terms of RF performances and hence, SiGe HBTs are often preferred over CMOS technologies in high-speed analog circuits. Consequently, for an optical receiver built on SiGe BiCMOS

platform, the analog part will exploit the high-speed capabilities of SiGe HBTs, while the digital part will make use of the high-density, low-power characteristics of MOSFET technologies.

In [28], a monolithically integrated optical receiver has been fabricated and successfully characterized on SiGe BiCMOS technologies (see Figure 1.6). The receiver includes a Ge integrated waveguide PD on which light is cast with a brag grating, a TIA, a Single-to-differential buffer (SDB) to convert the TIA outputs into fully differential signals, a post amplifier (PA) which enhances the gain bandwidth signal, and an output buffer providing 50 Ω matching impedance for measurements. The design and optimization of the optical receiver was done in the standard silicon integrated circuit design environment using an equivalent circuit model for the PD. Also, in 2017, higher data rates of 56 Gbps have been reported for monolithically integrated optical receiver [28], [29].

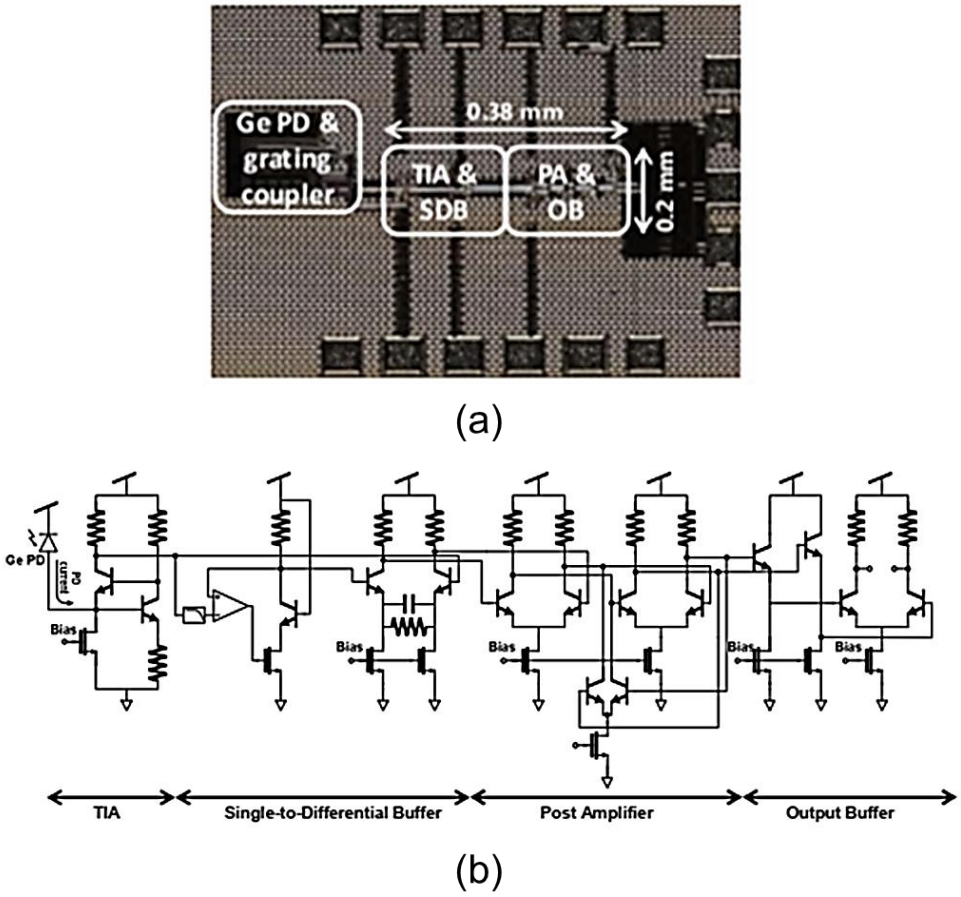

Figure 1.6. (a) Microphotograph of an optical receiver monolithically integrated with Ge PD (b) Schematic diagram of the optical receiver [28].

1.1.3 Conclusion and Perspective on OEICs

In this section, different approaches to photonic-electronic co-integration have been discussed. Although electronic and photonic devices based on III-V materials have superior performances compared to Silicon devices, the dominance of the latter in modern electronics

remains the driving force behind the development of high-performance Silicon photonics. However, with the exponential growth in data traffic that we are experiencing today, monolithic silicon electro-photonic integration does not seem to be able to keep up with this evolution and will most likely give way to monolithic InP platform integration.

1.2 Wireless communication

Today, existing conventional radio frequency (RF) wireless communication faces significant challenges in meeting growing bandwidth demands. Upper RF bands, including millimeter-wave and terahertz, offer greater bandwidth and must be exploited to support ultrafast wireless communications. In this section, we briefly discuss millimeter wave (mm-Waves) and terahertz (THz) generation and detection techniques. We also discuss the benefits of OEICs (convergence of electronics and photonics) in the mm-Waves and THz domains. Also, we address their potential to bridge the gap in data rate between fiber-optic and wireless networks. We conclude this section by presenting a few demonstrations of mm-Wave and THz links applied in wireless communication, based on Radio over fiber (RoF) techniques and photonic devices, in particular, the UTC-PDs.

1.2.1 Millimeter and Terahertz waves: sources and detectors

Sandwiched between microwave and infrared, mm-Wave (3-100 GHz) and Terahertz (0.1-10 THz) frequencies (see Figure 1.7) have been traditionally used in niche applications such as security imaging and spectroscopy, or high-resolution radar. Due to the large bandwidth available and the fact that large portions of these bands are still not regulated for use, they offer greater potential applications than the conventional microwave spectrum for the development of high-capacity wireless systems [30].

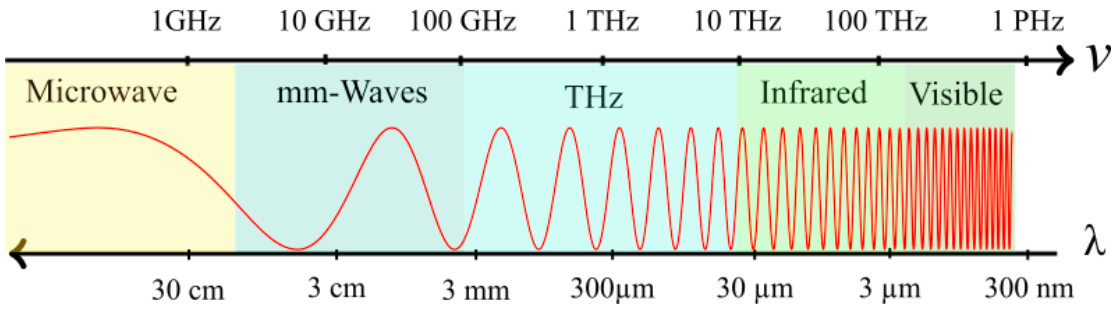

Figure 1.7. Millimeter and terahertz waves in the electromagnetic radiation spectrum.

Until the late 1980s, the lack of sources for the generation and detection of terahertz radiation created a frequency gap in the spectrum between 0.1 and 3 THz, known as the THz gap. Over the past few decades, the development of THz sources has progressed considerably. It started with the development of femtosecond-based technologies combined with photoconductive antennas used for both transmission and detection. The emergence of this technology in the 1980s thus greatly motivated researchers to invest in this frequency range,

even though these optical systems were still bulky and expensive [7]. Since then, significant efforts have been made to develop low-cost, efficient and eventually integrated systems for this frequency band. The fruits of this labor found applications in several fields, particularly in the domain of semiconductor and photonic devices. In the following, we discuss some of the photonic and electronic sources and detectors that work in the mm-Wave and THz range.

1.2.1.1 mm- and THz Waves generation

In electronics, the generation of mm-Wave and THz frequencies are done by techniques that rely on diodes, transistors or on frequency multiplication in low frequency oscillators.

Among the several examples of mm- and THz Wave generation by diode-based sources, one can cite Gunn diodes, resonant tunneling diodes (RTDs), IMPATT diodes, and tunnel injection transit time (TUNNETT) diodes [31]–[34]. The mm-Wave and THz generation relies on the negative differential resistance (NDR) of these diodes to generate high frequency oscillations. The difference between these diodes lies with the method used to produce the NDR, which results in variations of their performance parameters (oscillation frequency, output power, and phase noise) [35]. The IMPATT and Gunn diodes can generate high power at high frequencies (20 dBm at 100-200 GHz) [35], but they exhibit high phase noise levels. The TUNNETT diode is a variant of the IMPATT diode that can oscillate at higher frequencies with low phase noise, but with less output power. As for the RTD diode, it can generate the highest frequencies among these diode-based technologies (up to 1.92 THz) [32]. However, its output power is the lowest (below 1 µW). Table 1.1 summarizes some of the key figures of these diode-based sources.

Table 1.1. mm-Waves and THz diode-based sources.

Technology	frequency	Output power	Year	Reference
Gunn	78.9 GHz	25 mW	2015	[31]
	300 GHz	28 µW	2014	[36]
RTD	28 GHz	1mW	2013	[37]
	260 GHz	1 mW	2020	[38]
	1.92 THz	0.4 µW	2016	[32]
IMPATT	82 GHz	4.6 mW	2019	[39]

To achieve the NDR, transistor-based mm-Wave sources, such as CMOS transistors, Heterojunction Bipolar Transistors (HBT), Double Heterojunction Bipolar Transistors (DHBT), and High Electron Mobility Transistors (HEMT), use circuit-level topologies [35]. These transistor-based technologies can also offer higher power gain, making them more

attractive over diode-based sources. Due to their advantageous electron transport characteristics, HBTs and HEMTs based on III-V materials can oscillate beyond THz frequencies. The record for the highest f_t/f_{MAX} of 475 GHz/1.2 THz has been reported for InP/GaAsSb DHBTs [40]. Despite the relatively inferior electronic transport properties of Silicon, recent advances in CMOS transistors and SiGe BiCMOS HBTs have brought them back in competition with HBTs and HEMTs based on III-V materials. Maximum cut-off/ oscillation frequencies up to 505/720 GHz (f_t/f_{MAX}) have been achieved with these Si-based technologies [41].

The mm-Waves and THz generation through frequency multiplication, several stages of frequency multipliers are implemented to generate high frequency signals from a low frequency source. Frequency multiplication introduces high losses (theoretically: 7.4 dB, typically: 10 dB) [42], so an amplifier needs to be added to each frequency multiplication stage, which is often complex and expensive [35]. Additionally, each multiplication stage further degrades the noise characteristics. However, advances in CMOS technology have demonstrated the possibility of the generation of high power signals at hundreds of GHz [43].

The techniques discussed so far introduce unwanted phase noise, which may be intrinsic to the component or created and amplified post-amplification. This limits the data rate in communications systems especially when a higher order modulation format is used. There also exist techniques that produce low phase noise, but at the cost of low power generation. In these cases, the use of power combiners would become necessary.

There are also several photonic techniques for millimeter wave generation, including: optical heterodyne photomixing, mode-locked laser diodes (MLLDs) [44], nonlinear effects in waveguides and fibers such as four-wave mixing (FWM) [45], and the Brillouin fiber laser [46]. Each of these techniques has its unique advantages and disadvantages. MLLDs, for example, can generate high frequencies with low phase noise, but they are not tunable. The FWM technique can generate frequencies with low phase noise, but this technique requires high pump power and low conversion efficiency [42].

In what follows, we will focus on photomixing. Despite the fact that this technique produces a higher phase noise compared to other photonic techniques, it has several advantages such as simplicity of implementation, high tunability, full modulation depth and other characteristics [47].

Photomixing is an optoelectronic technique for generating terahertz waves, using two lasers and a photoconductor or a photodiode that converts the two laser beams into a Terahertz wave. The illumination of the photosensitive surface by the two lasers induces a modulation of the beat frequency between these two lasers, which corresponds to the modulation of the generation of electron-hole pairs in the photosensitive material (photo-current). The photo-mixer is then connected through a waveguide or a propagation line to an antenna to transmit the THz wave into the air (Figure 1.8). With tunable lasers, photo-mixing offers a tunable

terahertz source, since the beat frequency, ν_B, depends directly on the frequency of the two lasers ν_1 and ν_2. However, the bandwidth of the photo-mixers is limited by the materials which they are made of as well as their design [48].

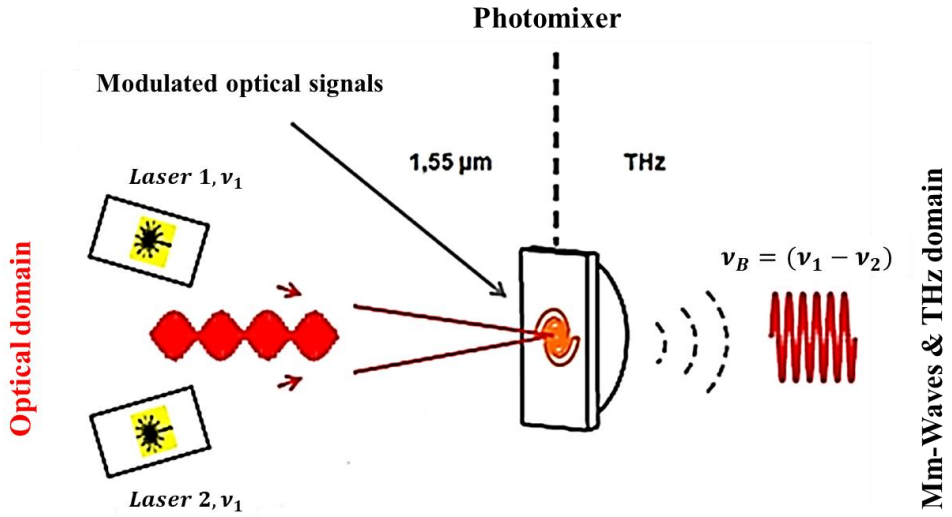

Figure 1.8. Schematic showing the photo-mixing principle [48].

From a mathematical point of view, let's consider two spatially superimposed laser beams, with the same polarization, that propagate along the z direction. Their frequencies are defined by ν_i with $i = \{1,2\}$. Their electric and magnetic fields can be written as follows:

$$\overrightarrow{E_i}(z,t) = E_i \cos(2\pi\nu_i t - k_i z + \varphi_i)\overrightarrow{e_x} \tag{1.1}$$

$$\overrightarrow{H_i}(z,t) = E_i \cos(2\pi\nu_i t - k_i z + \varphi_i)\overrightarrow{e_y} \tag{1.2}$$

To determine the energy associated with the photo-mixing of these two laser beams, we calculate the Poynting vector:

$$\vec{P}(z,t) = (\overrightarrow{E_1}(z,t) + \overrightarrow{E_2}(z,t)) \times (\overrightarrow{H_1}(z,t) + \overrightarrow{H_2}(z,t)) \tag{1.3}$$

The electric and magnetic fields are related to each other by [49]:

$$\sqrt{\varepsilon} \cdot |E| = \sqrt{\mu} \cdot |H| \tag{1.4}$$

Where ε and μ are the dielectric constant and magnetic permeability, respectively.

The magnitude of the Poynting vector is thus simplified as follows:

$$|\vec{P}(z,t)| = \sqrt{\frac{\varepsilon}{\mu}} |E_1(z,t) + E_2(z,t)|^2 \tag{1.5}$$

Assuming that the two lasers have the same magnitude ($E_1 = E_2 = E$) and the same phase ($\varphi_1 = \varphi_2$). The magnitude of Poynting vector at $z = 0$ (at photodetector surface) can be written as:

$$\left|\vec{P}(0,t)\right| = \sqrt{\frac{\varepsilon}{\mu}}(E^2 cos^2(2\pi\nu_1 t) + E^2 cos^2(2\pi\nu_2 t) + E^2 \cos(2\pi(\nu_1 + \nu_2)\, t + E^2 \cos(2\pi(\nu_1 - \nu_2)t)) \quad (1.6)$$

The beating frequency of the lasers can be recovered by a photodetector. The contributions ν_1, ν_2 and $\nu_1 + \nu_2$ are in the optical domain and are higher than the cut-off frequency of the photodetector and their values are therefore averaged. The magnitude of Poynting vector perceived by the photodetector thus becomes:

$$\left|\vec{P}(0,t)\right| = \frac{1}{2}\sqrt{\frac{\varepsilon}{\mu}}(2E^2 + E^2 \cos(2\pi(\nu_1 - \nu_2)t))) \quad (1.7)$$

This gives a static component as well as a beat component, $\nu_B = (\nu_1 - \nu_2)$, which can be solved in the RF domain.

There are three widely used photomixing devices: low temperature growth (LTG) GaAs photoconductors (LTG-GaAs), p-i-n PDs and the UTC-PDs. Among these, the photoconductor is the most basic photomixer, consisting of a semiconductor material sandwiched between two electrodes. When the semiconductor is illuminated by a laser beam whose energy is equal to or is higher than the band gap of the semiconductor, electron-hole pairs are generated. By applying an electric field to these charges, a closed circuit is formed which generates a current proportional to the power of the laser. The superposition of two laser beams very close in wavelength generates a current at the beat frequency of the two lasers. To ensure high performance of the photoconductors, it is important to have semiconductor materials with short carrier lifetimes and high carrier drift rates. As LT-GaAs photomixers are optimized for operation at a wavelength of 800 nm, they are less suitable for optical communications at 1550 nm wavelength. Efforts have been made to design photoconductors based on InGaAs [50]. However, they still offer lower performances compared to GaAs photoconductors or p-i-n and UTC-PD photodiodes (Figure 1.9) [51]. Moreover, the design process of InGaAs photoconductors is very challenging due to sometimes conflicting requirements, such as high absorption, high resistance, short carrier lifetime, high mobility and high breakdown field [50].

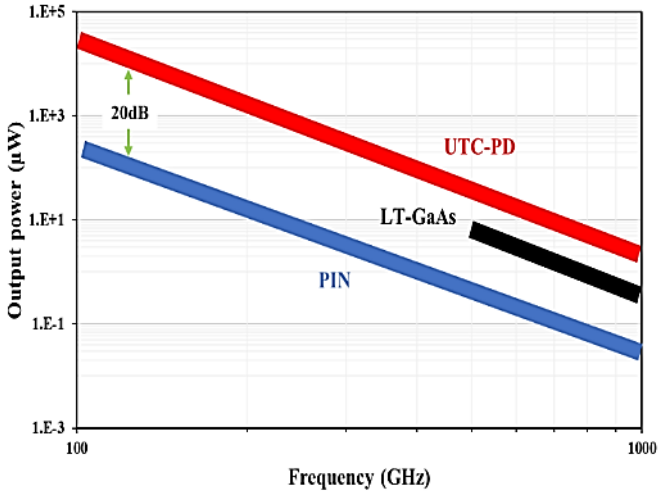

Figure 1.9. Comparison of photomixing devices in terms of output power [51].

Conventional p-i-n PDs have an intrinsic semiconductor layer that absorbs the targeted wavelength, sandwiched between p- and n-doped semiconductors. In p-i-n PDs, photo generation of electron-hole pairs occurs in the depletion region, where they drift in the presence of an electric field created by the semiconductor junction. The electron-hole drift dynamics and the intrinsic resistance and capacitance (RC) of the photodiode define the bandwidth of the photodiode. The thinner the depletion region, the shorter the transit time. However, this causes the capacitance to become larger, which limits the bandwidth and the responsivity of the photodiode. Furthermore, the trade-off between the width of the intrinsic region and the RC component is further limited by the hole velocity, which is lower than the electron velocity.

In contrast with the responsivity of p-i-n PDs which is limited predominantly by hole transit time through the intrinsic region, in UTC-PDs, the response is dominated by the electron drift velocity. In UTC-PDs, absorption and carrier collection are separate processes. Absorption occurs in the p-doped region, where holes are the majority carriers that recombine due to dielectric relaxation. Therefore, only electrons drift through the depletion region, resulting in a higher 3-dB bandwidth. Additionally, UTC-PDs feature better saturation characteristics compared to p-i-n PDs since there is no hole accumulation in the depletion region.

1.2.1.2 mm- and THz waves detection

Till date electronic-only circuits have proven to be the most efficient for the detection of mm- and THz waves. However, given the exponential growth of data traffic in wireless communication, OEICs appear to be the best candidate to support these demands.

There are two common methods used for electronic detection [52]: (i) direct detection, which can be achieved with either a diode detectors such as a Schottky Barrier Diode (SBD) or transistors such as HEMT (see Figure 1.10); (ii) Heterodyne detection which consists of mixing the received signal with a local oscillator (LO) to convert it into an intermediate frequency (IF) or baseband frequency. SBD and HEMT can be used in the direct detectors and heterodyne mixing receivers. To increase the sensitivity of the receivers, low noise factor (LNF) preamplifiers are used.

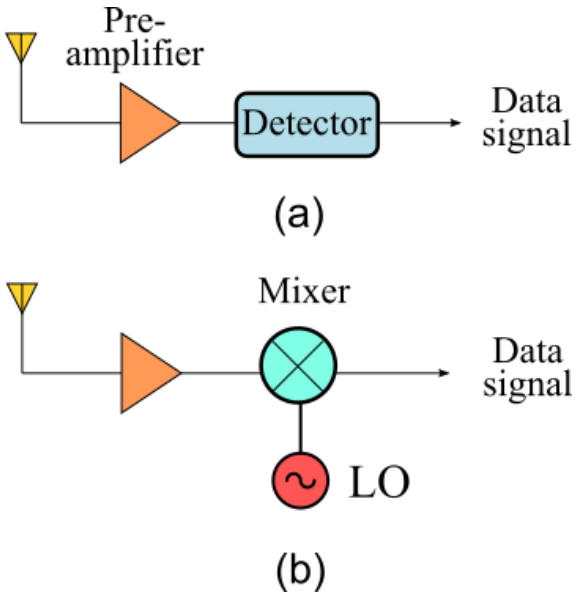

Figure 1.10. mm- and THz waves detection approaches (a) direct detection (b) heterodyne detection.

1.2.2 Deployment of mm-Wave and THz technologies in wireless communications

With the exponential growth in mobile traffic we are currently experiencing, the expected data rate for wireless communications in the market will reach 100 Gbps and higher in the coming years [53]. In the spectrum currently allocated for mobile services, the largest connected band is located around 60 GHz and ~70-95 GHz, where only a bandwidth of 7-9 GHz is available. This limits the total channel throughput even with QAMs of high spectral efficiency. Efficient communication requires larger bandwidths. Clearly, the use of an even higher carrier frequency in the THz range (0.1-10 THz) is mandatory when the minimum required bandwidth reaches several tens of GHz [7], [54], [55].

A vision of future wireless network architectures based on RoF is illustrated in Figure 1.11, where the central idea is that wireless backhauling infrastructures are provided by high-speed wireless point-to-point links that operate at THz frequencies and can be efficiently interfaced with fiber optic networks. Moreover, a large number of transparent terminals and a dense mesh of small radio cells are required to provide ubiquitous, broadband wireless access [56]–[58].

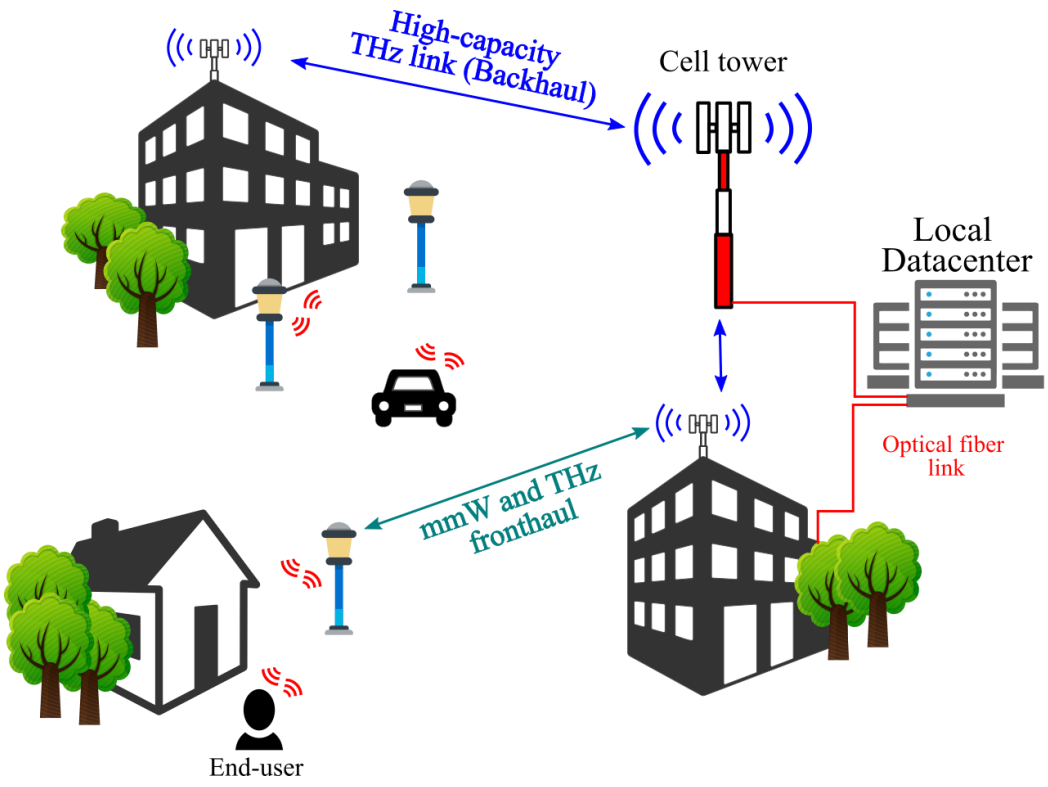

Figure 1.11. Vision of the future wireless network architecture based on mm-Waves and THz technologies.

For optimal flexibility and performance, signal transmitters and receivers in wireless communications must be capable of switching between windows depending on channel occupancy. As shown in Figure 1.12, at the level of the transmitter, Tx, the generation of a THz

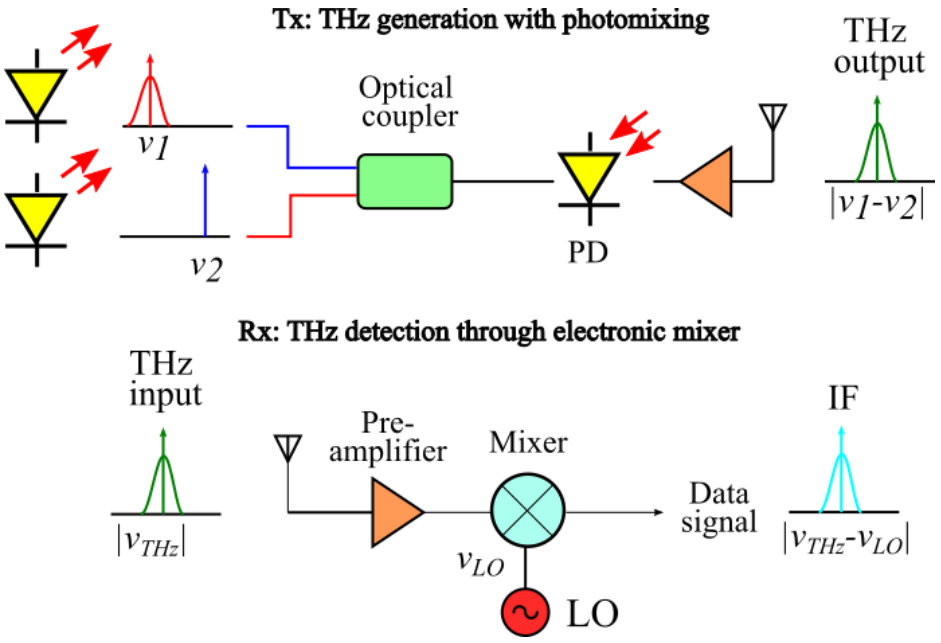

Figure 1.12. THz detection through electronic-based mixer.

carrier is based on heterodyning two lasers of frequencies ν_1 and ν_2 on a high-speed photodiode connected to a broadband antenna. The generated THz signal can be tuned by changing the frequency of the unmodulated laser. This THz signal, on the receiving end, Rx, can be extended by an electronic module. The module consists of an antenna to detect the radiation, a low noise preamplifier to boost the signal power and sensitivity of the receiver, and finally a millimeter wave detector or mixer based on Schottky barrier diodes (SBD).

Electronic receiver modules, however, cannot match the wide bandwidth of the transmitter module. To overcome this limitation, some optoelectronic receiver modules, Rx, have also been proposed (see Figure 1.13). These modules are based on a photoconductor (or photodiode), driven by an LO generated by superimposing two optical tones on a photoconductor [59], [60].

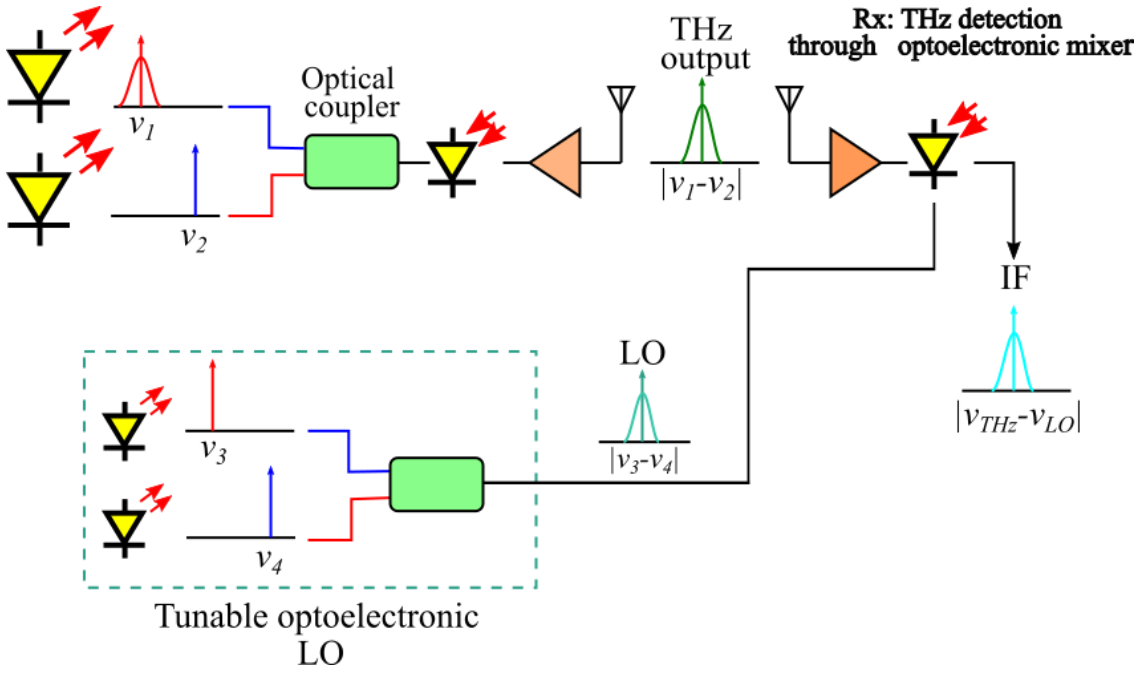

Figure 1.13. THz detection through optoelectronic-based mixer.

1.2.2.1.1 UTC-PD based mm-Waves and THz wireless communication

UTC-PDs have been widely studied for ultrafast optoelectronic applications, including THz signal generation and as local oscillators. High performances have been reported, reaching bandwidths of more than 600 GHz and power levels of the order of milliwatt around 300 GHz [61], [62]. These performances allowed the realization of the first indoor THz radio links with "optical" data rates [7]. The integration of UTC-PD in wireless communication transceivers offer high speed fiber links, achieved using RoF techniques.

Table 1.2 summarizes the state of the art for the wireless links in mm-Wave and THz frequency ranges, particularly using UTC-PD and RoF techniques. The table also includes information on demonstrations using p-i-n PDs and fully electronic transceiver modules, for comparison.

From the comparison we can conclude that: (i) The highest carrier frequency and the highest data rates that have been achieved in the THz frequency range for photonic technologies developed with UTC-PD as the source on the transmitter side; (ii) On the receiver side, electronic based detectors (direct detectors and mixers) have been used exclusively, indicating that photonic-based receivers are not yet competitive; (iii) To enhance the data rate, the combination of spatial multiplexing and polarization techniques have been explored.

Table 1.2. State of the art of wireless link demonstration with highest performance.

Technology Tx/Rx	Frequency (GHz)	Data rate (Gbps)	Distance (m)	Modulation format	Bit error	Year	Reference
Photonic UTC-PD/SDB	670	10	15	ASK	$<10^{-9}$ real time	2018	[63]
Photonic p-i-n/HEMT	300	128	0.5	16-QAM	2.2×10^{-2} offline	2019	[64]
130-nm SiGe BiCMOS	230	100	1	16-QAM	1×10^{-3}	2019	[65]
Photonic UTC-PD/SDB	350	2x300	2.8	64-QAM OFDM	2.7×10^{-2} offline	2020	[66]
Photonic UTC-PD/HEMT	300	100	15	16-QAM	4×10^{-3}	2020	[67]
Photonic p-i-n PD/HEMT	300	160	50	32-QAM	2.9×10^{-4}	2022	[68]
Photonic UTC-PD/SBD	400	131	10.7	16-QAM	2.7×10^{-2} offline	2022	[69]

1.2.3 OEICs for mm-Waves and THz transceiver

As we have shown in the previous section, photonic devices play a key role for future wireless communication systems in the mm-Wave and THz frequency domain, especially for the generation of high carrier frequency and bandwidth by heterodyne mixing using a photodiode. In all these demonstrations, signal reception was based on electronic circuits. The

implementation of optoelectronic receivers has now begun to generate an increasing interest because of their manyfold advantages. Beyond the wide bandwidth that optoelectronic receivers can offer, they have several other interesting features: (i) optoelectronic receivers can operate at very high frequencies and wide-band systems, especially when UTC-PDs are used as mixers, e.g., from 90 to 580 GHz with frequency-independent phase noise [70], (ii) (ii) optoelectronic receivers can be monolithically integrated, resulting in more compact, efficient, and less expensive systems; (iii) Unlike Schottky diode mixers, a photodiode mixer does not require an electronically generated LO, as it can be generated by the UTC-PD itself, by heterodyning two optical signals [71].

Till date, most experimental demonstrations of high-speed optoelectronic THz communications are still performed in the laboratory. In 2014, a fully integrated monolithic chip on InP substrate was demonstrated (see Figure 1.14) for the mm-Wave applications. This chip demonstrated the ability to act as both transmitter and receiver [72]. The chip included two tunable DFB lasers that allowed for heterodyne mixing. It also included SOA optical amplifiers, electro-optical modulators (whose modulation can be directly applied to the chip) and finally UTC-PDs. Demonstration of a communication link in the mm-Wave range using this chip has been reported in [47], where a UTC-PD was used at the transmitter to generate a 1 Gbps OOK data signal at a carrier frequency of 61.3 GHz. This was done by heterodyning two modulated optical tones from an optical frequency comb system. The generated electrical heterodyne signal was then transmitted using a parabolic antenna with a 25 dBi gain. The signal was transmitted wirelessly over a distance of 0.55 m and was received on a different antenna with identical characteristics, connected to an optically pumped UTC-PD mixer. This mixer converted the received RF signal to an intermediate frequency of 6.3 GHz, which was then amplified and acquired by a real-time oscilloscope for offline processing. The recovered data exhibited an open-eye pattern and a bit error rate of the order of 10^{-5} was measured.

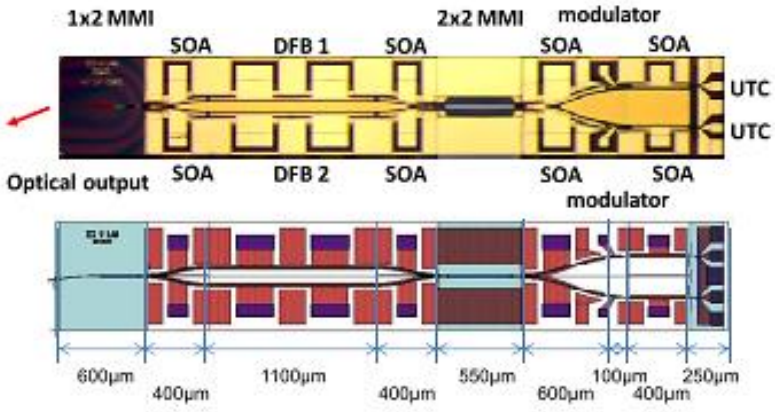

Figure 1.14. Microscopic view and layout of the PIC chips [72].

Figure 1.15 shows the first successful demonstration of a wireless THz communication link that exploits OECs at both the transmitter and receiver operating in the THz range [59]. Their approach relied on a high-speed photoconductor and a photonic local oscillator for optoelectronic down conversion of THz data signals to an IF band. Also, they demonstrated that tuning the frequency of the photonic LO allows a wide range of carrier frequencies to be covered between 0.03 and 0.34 THz. Furthermore, data rates of up to 10 Gbps on a single channel and up to 30 Gbps on multiple channels transmitted over a distance of 58 m were also demonstrated.

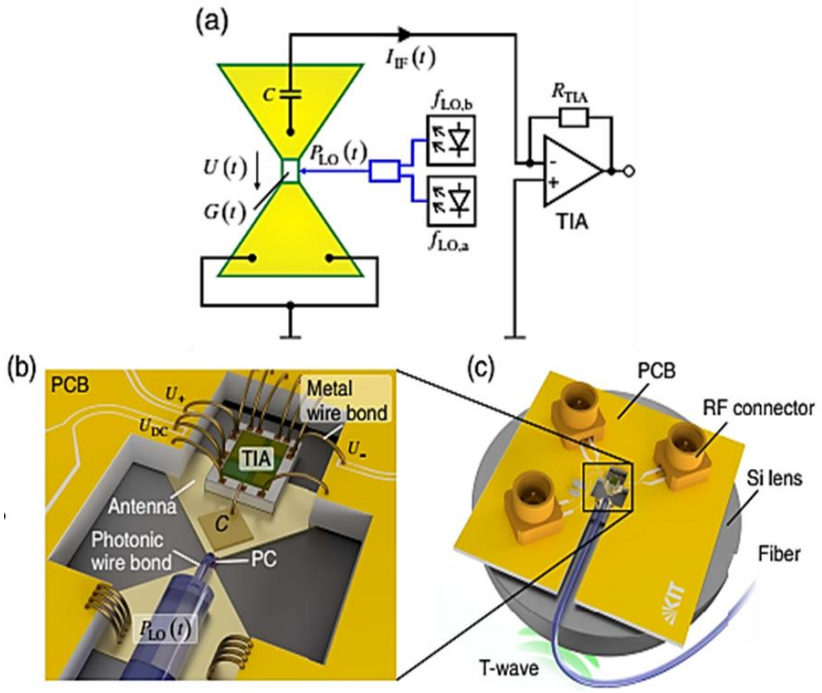

Figure 1.15. Schematic of the optoelectronic receiver: (a) concept and principle, (b) the optical coupling and the interconnections between the photoconductor, the TIA and the antenna, (c) the optoelectronic receiver assembled on a printed circuit board and bonded to a silicon lens to receive the THz signal [59].

1.2.4 Conclusion and Perspectives on monolithic OEICs for wireless communication

Despite the advantages that photonic technologies offer in terms of link efficiency and generating high data rates, the deployment of a complete wireless communication technology in mm-Waves and THz is still faced with multiple challenges. These systems still need more output power at the transmitter level, especially for applications such as backhaul, where a distance of 1 km needs to be reached [7]. To deal with the power limitation of photonic devices, future THz OEICs and systems could rely on combining power amplifiers with photomixers. However, maximum performance requires monolithic integration of both photonic and electronic devices to obtain minimal losses , which has not yet been achieved in the THz range [7].

1.3 Conclusion

Future communication systems will have to support the expected increase in data traffic. Monolithic OEICs appear to be a viable and efficient solution. Receivers based on monolithic OEICs with high bandwidths for optical communications are hence essential. UTC-PDs are a key component in OEICs. They have been widely studied for ultrafast optoelectronic applications, including THz signal generation, and high performances have been reported, demonstrating bandwidths of more than 600 GHz obtained with good power levels [63].

For wireless communications, the availability of efficient, low-power, and compact transmitters and receivers will be a key element for the implementation of high-performance systems. This can be realized by mm-Wave and THz wireless technology based on monolithic OEICs in which UTC-PD takes the center stage.

The recent trend of research in OEICs indicates that the electronics and photonics communities are looking for an efficient and most crucially a common way of modelling elementary components for their systems. As a first step towards the development of a unified modelling solution, we propose a scalable, compact and multi-physics model for the UTC-PDs. The model is written in Verilog-A and is compatible with the existing electronic circuit design methodology/tool/flow. The model is developed based on the charge carrier transport equations in the UTC-PDs and will be discussed in the next chapter.

Chapter 2: UTC-PD fundamentals and compact modelling

In this chapter, we first introduce the concept and the fundamental physics of the UTC-PDs. We then present a brief literature review of the technological progresses that have been made to improve the performances of the UTC-PDs in term of responsivity and bandwidth. As the UTC-PDs are mainly used in very high data rate communication systems, the development of a reliable, computationally efficient model, compatible with existing circuit design tools (Cadence, Siemens EDA, etc.) is crucial for the design and simulation of such communication systems. For that, we highlight the importance of small-signal and compact modelling approaches and we describe the main models developed based on early theoretical efforts on UTC-PD modelling. Although small signal models are easy to implement and fast to simulate, they still have several limitations that we will also address. Finally, within the scope of our study and in order to overcome small signal modelling limitations, we propose a compact model which offers more versatility higher accuracy since it physics based.

2.1 Overview of the UTC-PD

The Uni-Traveling Carrier Photodiode (UTC-PD) was invented by T. Ishibasi of Nippon Telegraph and Telephone (NTT) corporation, Kanagawa, Japan in 1997 [73]. As the name implies, the UTC photodiodes rely only on electron transport, which mainly distinguishes the performances of this type of photodiodes from other types, e.g., the conventional p-i-n photodiodes (p-i-n PD).

Figure 2.1 (a) and (b) show the energy band diagrams of the classic p-i-n PD and the UTC-PD, respectively [74]. In p-i-n PD, the absorption occurs in the depletion region (not intentionally doped n-i-d) where electron-hole pairs are photo-generated and then driven out by the electric field present in this region. As the velocity of the holes is lower than the one of the electrons the response of the device will be mainly limited by the hole velocity. This is illustrated in the impulse response in Figure 2.1 (c) observed using the electro-optical sampling (EOS) technique. The p-i-n PD waveform consists of two current components: the initial fast component is attributed to electron transport, and the slow tail is due to hole transport.

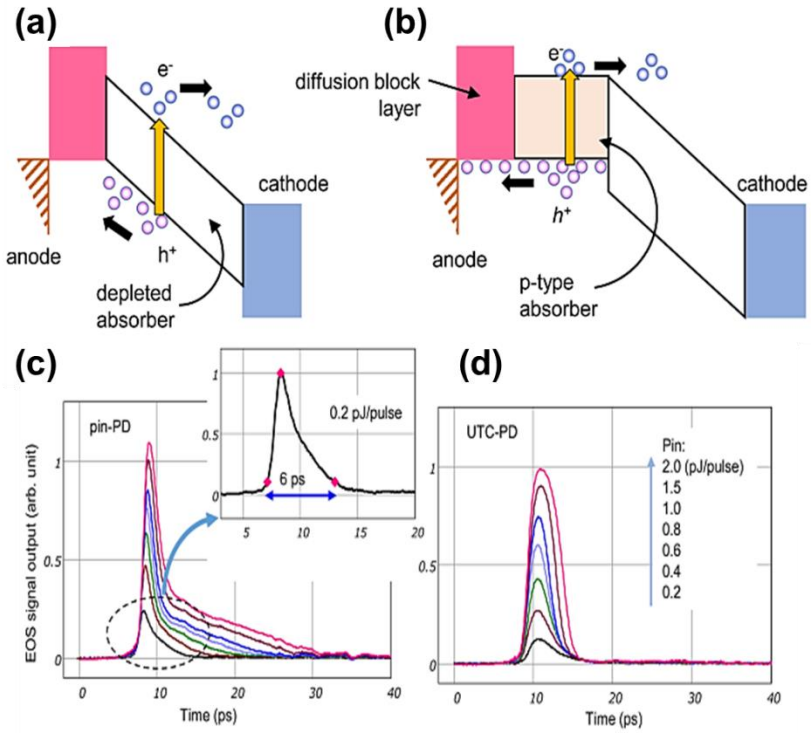

Figure 2.1. Band diagrams of (a) p-i-n PD (b) UTC-PD; Output signals observed by EOS measurement under various input optical power for (c) p-i-n PD (d) UTC-PD [74].

In the UTC-PD, the p-doped absorption region is separated from the collection region (or depletion region), which is slightly n-doped. For the photo-generated electron-hole pairs, the minority electrons systematically diffuse from the absorption layer to the collection layer due to the presence of a wider energy band gap material on the absorption layer side. Indeed, the discontinuity of the conduction band forms the barrier that prevents electrons from reaching the anode. Following diffusion, the electrons then drift into the collector layer driven by the electric field present in this region. At the same time, the majority of holes diffuse via the dielectric relaxation mechanism, which is essentially the tendency of a material to regain its neutrality almost instantaneously in the presence of a small perturbation. This reduces the dependence of the UTC-PD photoresponse to only electron transport. Figure 2.1 (d) shows the impulse response of the UTC-PD observed by same the electro-optical sampling (EOS) technique. The UTC-PD waveform is very different from that of the p-i-n diode, especially since the fall time of the waveform does not increase significantly. The quick fall time is attributed to the fast response of the electron-only transport.

2.2 UTC-PD Development

The first UTC-PD structures consisted of a simple mesa structure with a top illumination. The absorber constitutes a $2.5 \cdot 10^{18}$ cm^{-3} p-doped $In_{0.53}Ga_{0.47}As$ layer with a thickness of 220 nm. The collector was formed of an *n-i-d InP* layer with a thickness of 200 nm [73]. The *InGaAs* was chosen for its high absorption efficiency at 1.55 µm of wavelength, which is the wavelength typically used for optical fiber communication. The *InP* was chosen for its electron mobility

and its transparency at this wavelength. The reported bandwidth for this illuminated UTC-PD is 80 GHz [73].

This initial structure was improved by introducing a grading of the energy band at the heterostructure interface, formed by the absorption and the collection layers, in order to reduce the blocking of photo-generated electrons at this interface. Thus, in the initial structure, intermediate layers of *i-InGaAs/i-InGaAsP/i-InP/n-InP* were inserted between the *p-InGaAs* absorption layer and the *InP* collection layer. A bandwidth of 94 GHz was reported despite the fact that the absorption layer (220 nm) and the collection layer (300 nm) are thicker than the first proposed structure [75]. This result was attributed to the reduction in electron transit time [75]. The work on bandwidth enhancement was continued by the same team by reducing the thickness of the UTC-PD and especially the thickness of the absorber. Bandwidths of 220 GHz and 310 GHz for absorber thicknesses of 86 nm and 30 nm, respectively, have been reported. However, these performances were obtained at the expense of the responsivity which was considerably reduced from 0.2 A/W in [75] to 0.12 A/W and then to 0.07 A/W in [76], [77].

For more details on the numerous efforts to improve the design and energy band diagram of the UTC-PD, a comprehensive and chronological study of the development of UTC-PDs can be found in [78].

2.2.1 UTC-PD topology

A thin absorber increases the bandwidth but at the detriment of the responsivity value. A compromise is therefore sought to find the optimal performance. The goal is to improve the responsivity for low thicknesses without compromising the thickness of the absorber which will affect the bandwidth of the UTC-PD. Several efforts leading to the proposal of new UTC-PD designs have been reported in the literature [10].

The responsivity corresponds the ratio of the output photocurrent over the incident optical power (in A/W). It can be expressed as a function of the internal quantum efficiency, $\boldsymbol{\eta_{int}}$, as follows:

$$\boldsymbol{R = \frac{\eta_{int} q \lambda}{hc}} \qquad (\mathbf{2.1})$$

Where, q, h and c are the elementary charge, the Planck constant and the speed of light respectively.

The quantum efficiency for top-illuminated photodiodes (Figure 2.2) is determined by the absorption coefficient, α, and the absorbing layer thickness, d, as follow:

$$\boldsymbol{\eta_{int} = 1 - e^{-\alpha . d}} \qquad (\mathbf{2.2})$$

As mentioned above, a thick absorber increases responsivity but at the cost of reduced bandwidth. To overcome this, other structures have been proposed, including UTC-PDs with refracting facet [79] and integrated waveguide UTC-PDs [80].

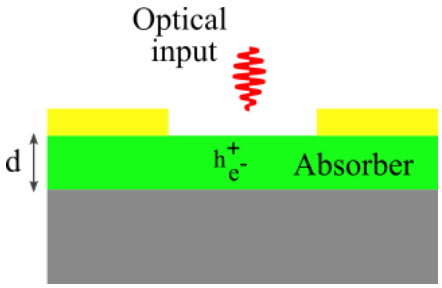

Figure 2.2. Structure of top- illuminated photodiode.

2.2.1.1 Refracting facet UTC photodiode

A UTC-PD structure with refractive facet has been developed by H. Fukano at NTT [79]. The optical coupling in the UTC-PD is a mix of both vertical and waveguide couplings. Here, the light arrives parallel to the absorber and is then refracted into the cleaved input facet as illustrated in Figure 2.3. As a result, the light transits at an angle through the absorber layer, which increases the effective thickness and thus improves the quantum efficiency of the photodiode. A responsivity of 1 A/W was achieved with the UTC-PD refractive facet for a bandwidth of 40 GHz.

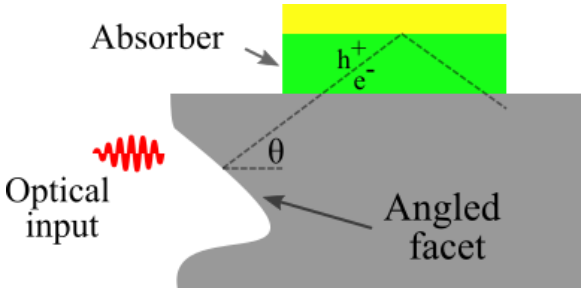

Figure 2.3. Structure of refracting facet photodiode.

2.2.1.2 Waveguide integrated UTC-PD

In order to improve responsivity and at the same time ensure a high bandwidth, other approaches have been explored, among which is the lateral illumination configuration (Figure 2.4 (a)). In this case, the light is coupled in parallel with the absorption layer. The quantum efficiency, η, for a single mode photodiode in this case is written as:

$$\eta_e = \eta_0\left(1 - e^{-\Gamma.\alpha.L}\right) \qquad (2.3)$$

Where Γ is the confinement factor, L is the length of the absorption layer and η_0 is the coupling efficiency between the optical fiber and the waveguide-integrated photodiode.

However, this type of optical coupling requires the use of an optical fiber with a very small mode field diameter. Since commercial optical fibers have a mode field diameter of about 5 µm, the coupling of these fibers with an absorbing layer of some hundred nanometers is not a simple task.

An evanescent illumination can better distribute the light along the absorbing layer, on one hand, while on the other hand improve the tolerances in positioning of the optical fibers. In waveguide integrated photodiode with evanescent coupling, the light is injected first into a waveguide and then transferred to the absorption layer (Figure 2.4 (b)). Two main types of evanescent coupling have been developed, as described next.

The first method uses a single-mode waveguide fabricated with a material of low refractive index, which allows to obtain an optical mode wide enough for effective coupling with the optical fiber. An optical matching layer with a higher optical index is inserted between the single mode waveguide and the absorption layer, allowing the coupling of light between these two parts.

The second type of evanescent coupling uses a multi-mode waveguide. This approach helps to achieve a higher efficiency for a smaller size of the photodiode compared to the case of the single-mode waveguide. However, the graded index structure of these multimode waveguides requires the use of three different quaternary materials, which complicates the device fabrication [80].

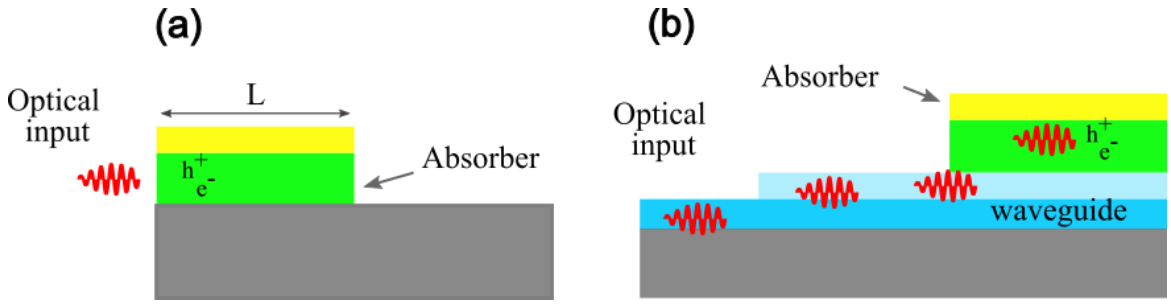

Figure 2.4. Schematic of (a) waveguide photodiode (b) waveguide evanescent coupling photodiode.

The IIIV-Lab proposed a diluted multi-mode *InGaAs/InP* waveguide using a single quaternary layer to simplify the epitaxy. This new design allowed to achieve responsivities of 0.76 A/W and 0.6 A/W for bandwidths above 50 GHz and 110 GHz, respectively [81], [82].

The given expressions for responsivity and quantum efficiency are further simplified, and are valid in a homogeneous absorption scenario in the absorber. This absorption scenario ensures a homogeneous optical generation rate. It is important to note that a homogeneous

generation rate results in maximum responsivity and thus RF power, in comparison to the case of inhomogeneous distribution.

As micro/nano-manufacturing technology progresses, improvements are made on top-illuminated UTC-PDs. Anti-reflective coatings and nanostructured metal contacts are currently used. However, the shrinking size of the devices required for higher bandwidths leads to the metal contacts covering a large portion of the illumination area. This results in a higher reflection and thus a reduction of the responsivity. Consequently, the design and configuration of the absorbing and anti-reflective layers, as well as the metal contacts, must be carefully analyzed. A simple approach to calculate the generation rate is thus not sufficient. A full 2D or 3D physical simulation is required to design and optimize the individual photodiodes, which is beyond the scope of our compact modelling approach. For example Figure 2.5 (a) shows the optical power distribution inside a top-illuminated Si/Ge UTC-PD grown on a the SOI substrate with an anti-reflective coating on the Ge absorption layer [83]. Due to the interference effect between the incident and reflected light from the different layers, the optical power inside the UTC-PD shows a periodic distribution. An analysis of the different configurations and thicknesses of the layers constituting the device is thus required to design more advantageous structures for higher absorption. This work should be conducted prior to the compact modelling of the photodiode.

For the integrated waveguide UTC-PDs, achieving optimal coupling between the waveguide and the absorber layer is a priority. Therefore, analyses are necessary to maximize the optical coupling. The homogeneous generation rate can be achieved by ensuring the most uniform optical absorption profile in the absorber, which again can only be achieved with full physical simulations in 2D or 3D. Figure 2.5 (b) shows an optical simulation study of realistic

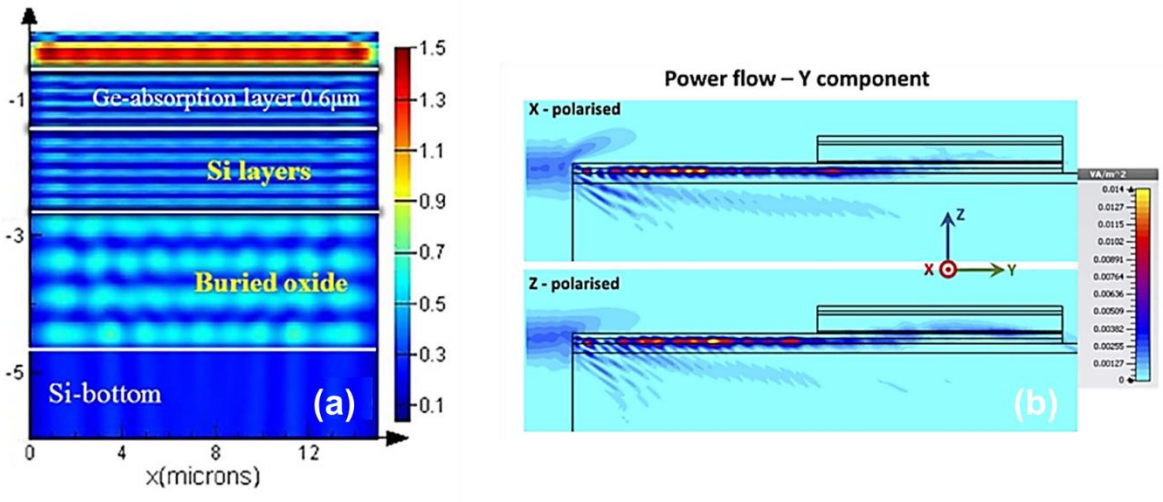

Figure 2.5. Optical power distribution inside (a) top-illuminated Si/Ge UTC-PD [83] (b) waveguide integrated InGaAs/InP UTC-PD [84].

scenarios in integrated waveguide UTC-PDs [84]. Here, the light source is a Gaussian beam, which is a good approximation of the light coupled from a lensed optical fiber, into the waveguide. In this type of simulation, it is possible to study: the effect of the misalignment

between the Gaussian beam and the waveguide, the type of optical propagation mode in the waveguide (single mode or multimode), the profile and the optical generation rate in the absorption layer of the UTC-PD.

The calculation of the absorption coefficient and the optical carrier generation rate can be studied considering either the particle or the wave representation of light. The wave representation of light approach, is widely used in the context of integrated photodiodes in order to identify the predominant absorption regions.

Considering that a plane wave of frequency, ω, is propagating through a semiconductor with a velocity, v, and moving in the x direction, the electric field can be defined by the following equation:

$$\boldsymbol{E = E_0 e^{j\cdot\omega\cdot\left(\frac{x}{v}-t\right)}} \qquad (\mathbf{2.4})$$

Here, E_0 signifies the incident field and the term $\omega \cdot (\frac{x}{v} - t)$ is the displacement at time t. The relation of the speed of light in the semiconductor is given by:

$$\boldsymbol{v = \frac{c}{N}} \qquad (\mathbf{2.5})$$

Where, N is the complex refractive index of the semiconductor, which also represents the dielectric constant $\sqrt{\varepsilon(\lambda)}$ as:

$$\boldsymbol{N = \sqrt{\varepsilon}(\lambda) = n(\lambda) - j \cdot K(\lambda)} \qquad (\mathbf{2.6})$$

Where, n is the refractive index and K the extinction coefficient and λ is the wavelength.

Replacing N by its expression in equation (2.5) and replacing the new expression of v in equation (2.4), we obtain:

$$\boldsymbol{E = E_0 e^{j\cdot\omega\cdot\left(n\frac{x}{c}-t\right)} e^{-\cdot\omega\cdot K(\lambda)\frac{x}{c}}} \qquad (\mathbf{2.7})$$

The first exponential denotes harmonic oscillation, while the second one describes the decay of the electric field along the x direction due to extinction. The absorption coefficient is defined by:

$$\boldsymbol{\alpha(\lambda) = \frac{2 \cdot \omega \cdot K(\lambda)}{c}} \qquad (\mathbf{2.8})$$

The optical carrier generation rate associated to the optical absorption in photodiodes, can be calculated by several techniques, such as the Beam Propagation Method (BPM), the Eigenmode Expansion Method (EEM) or the Finite Difference Time Domain (FDTD) method. The FDTD method is the most widely used and is an advanced method to: solve Maxwell's

equations, calculate the absorbed optical power and then the optical generation rate at each point in space. Starting from Poynting's theorem, we have [85]:

$$\frac{\partial U}{\partial t} + \nabla \cdot \vec{P} = \vec{J} \cdot \vec{E} \tag{2.9}$$

Where, $U = \frac{1}{2}(\varepsilon \cdot |E|^2 + \mu \cdot |H|^2)$ is the total energy density, $\vec{P} = \vec{E} x \vec{H}$ is the Poynting vector and $\vec{J}$ is the current density of free charges.

The expression (2.9) can be further simplified if there is no electric current, i.e., $\vec{J} = 0$:

$$\nabla \cdot \vec{P} = -\frac{\partial U}{\partial t} \tag{2.10}$$

Converting into the frequency domain by using:

$$\tilde{P} = S_0 e^{-j\omega t} \tag{2.11}$$

$$\tilde{U} = U_0 e^{-j\omega t} \tag{2.12}$$

Equation (2.10) becomes:

$$\nabla \cdot \tilde{P} = j\omega \tilde{U} \tag{2.13}$$

$$\nabla \cdot \tilde{P} = j \cdot \omega \cdot \left(\frac{1}{2}\left(\varepsilon \cdot |E|^2 + \mu \cdot |H|^2\right)\right) \tag{2.14}$$

The absorbed power per unit volume (Pabs) is calculated from the divergence of the Poynting vector as follows [86]:

$$P_{abs} = -\frac{1}{2} Re\left[\nabla \cdot \vec{P}\right] \tag{2.15}$$

$$P_{abs} = -\frac{1}{2} Re\left[\frac{1}{2} j\omega\left(\varepsilon \cdot |E|^2 + \mu \cdot |H|^2\right)\right] \tag{2.16}$$

The electric and magnetic fields are related to each other through [49]:

$$\varepsilon \cdot |E|^2 = \mu \cdot |H|^2 \tag{2.17}$$

Replacing equation (2.17) in equation (2.16), the absorbed optical power becomes:

$$P_{abs} = -\frac{1}{2} \omega \cdot |E|^2 Im[\varepsilon] \tag{2.18}$$

In 3D structures and for various wavelengths of incident optical beam, the expression in (2.18) can be generalized as follows:

$$\boldsymbol{P_{abs}(r,\lambda) = -\frac{1}{2}\omega \cdot |E(r,\lambda)|^2 Im[\varepsilon(r,\lambda)]} \quad (2.19)$$

Assuming that each absorbed photon generates an electron-hole pair, the number of photo-generated carriers per unit volume, $G(r,\lambda)$, can be calculated by dividing $P_{abs}(r,\lambda)$ by the photon energy, as shown in the equation (from [86]):

$$\boldsymbol{G(r,\lambda) = \frac{P_{abs}}{\hbar\omega} = -\frac{\pi}{h} \cdot |E(r,\lambda)|^2 Im[\varepsilon(r,\lambda)]} \quad (2.20)$$

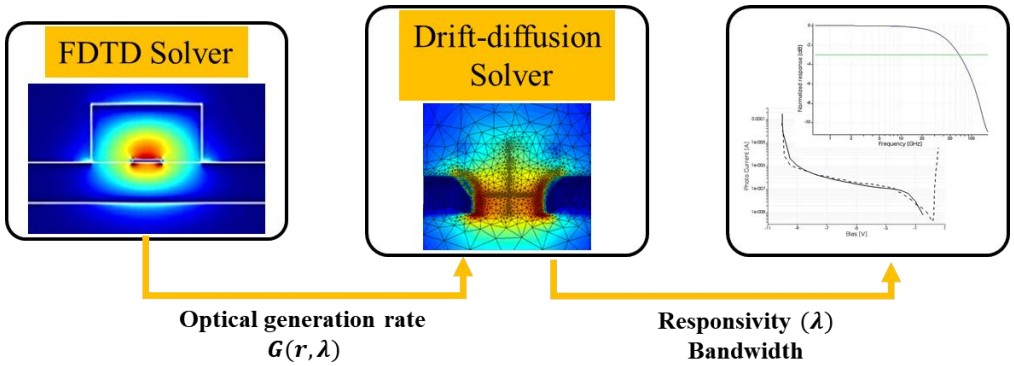

Figure 2.6. The general workflow for simulating a photodetector with FDTD and Drift-Diffusion solvers.

The generation rate $G(r,\lambda)$ can then be used as input to another solver that can solve the drift-diffusion equations, in order to calculate the responsivity and other figure of merits of the photodiode such as the bandwidth. The general workflow for simulating a photodetector with the FDTD and Drift-Diffusion solvers is summarized in Figure 2.6.

2.3 UTC-PD modelling

The ability to provide large bandwidth at a high power level makes a UTC-PD quite attractive for various applications, especially in the high data rate communication systems where the development of OEICs seems very promising. The architecture of OEI circuits and systems varies according to the application type and can quickly become quite complex. The need for a co-design and verification infrastructure for such systems, capable of supporting billions of devices, is therefore mandatory.

There exist software such as Lumerical and Sentaurus that can be used to perform coupled physical simulations of photonic devices. The workflow consists of constructing the device geometry, defining the materials and boundary conditions and finally performing the simulations. Typically, two different solvers are used to obtain the final results. A first solver, based on the FDTD method, computes the generation rate according to an incident optical signal. Then, a second solver calculates the responsivity and the bandwidth from the drift-diffusion equations, or the hydrodynamic equations, if a more complex model is considered. Even though these software offer detailed and quite precise results, the calculation time is too intensive and requires too much computing resources to simulate thousands of components.

In the RF domain, physical models of the devices are easier to simulate when they are implemented as electrical equivalent circuits. Using this approach, called small signal modelling, the intrinsic parameters of the UTC-PD can be translated into equivalent electrical circuit elements.

The complexity of device modelling for circuit/system requires models to be more versatile, both in terms of UTC-PD technology and under different operating conditions, compatible with various standard simulation platforms, and flexible enough to analyze UTC-PD performance along with other RF devices within the integrated circuits. The compact modelling approach has these advantages.

The compact models are, in fact, physical models translated into simpler and easy-to-solve analytical equations through reasonable assumptions and approximations. These models are commonly written using programming languages such as Verilog-A, that are compatible with SPICE circuit design tools and software (Cadence, Siemens EDA, etc.). In electronics, compact models have already reached a significant degree of maturity and computational efficiency over the last few decades. To enable the design of high-speed integrated communication technologies, the photonics community has also started looking for accurate and physics-based compact models for optoelectronic devices, in order to unify electrical, photonic and electromagnetic modelling using the same existing software design tools [87]. It is important to note that a scalable compact model offers a two-fold benefit. At the device level, a scalable compact model is a powerful tool for predicting performances across varying device geometries and operating conditions, it also provides a quick feedback on the impact of each technological and physical parameter. At the circuit/system level, compact models enable optimization of bias points and interconnections between photonic and electronic components, providing guidelines for OEIC design as well as prediction of its performances.

Figure 2.7 summarizes the three modelling approaches studied in this work and compares them in terms of desirable features, such as computational speed, scalability, and physical basis.

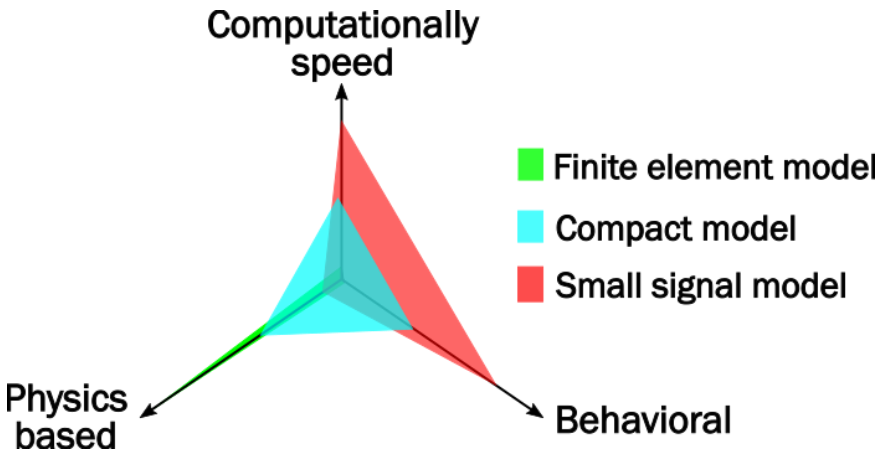

Figure 2.7. A comparison between different modelling approaches.

2.3.1 UTC-PD small signal modelling

UTC-PDs have great potential to be included in an integrated circuit with other photonic and RF devices. Therefore, the electrical equivalent circuit representation of UTC-PDs along with that of the other devices allows to predict the performance of circuits and systems developed based on those devices.

Several efforts for small signal modelling of UTC-PDs have been reported in the literature. These works have been based essentially on the representation of the electrical equivalent circuit describing the properties of the different material layers constituting the UTC-PD and on the description of the photo-response derived from the first analytical modelling work [73].

Since the first work on UTC-PD small signal modelling reported by H. Ito et al [88], numerous works have continued to propose electrical equivalent circuit models based on the UTC-PD design [89], [90]. Most of the proposed equivalent circuit models consist of a two-port network as depicted in Figure 2.8. The first port includes the electrical elements such as the series resistance, which represents the resistance of the UTC-PD metal contacts, and a junction capacitance in parallel with a resistance, which models the active region of the UTC-PD. The second port is formed by an R-C network that models the transit time of the photo-generated carriers. The two ports are coupled together through a voltage controlled current source (VCCS) where the current is calculated from the product of the responsivity and the input optical power. In addition, parasitic elements are added to model pads and access lines that are designed with a characteristic impedance of 50 Ω matched to the measurement instruments.

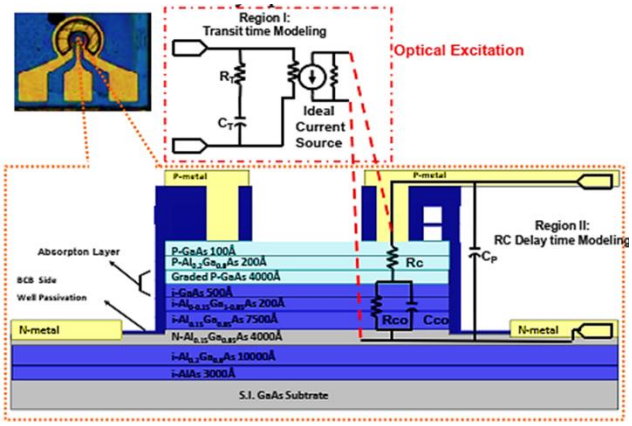

Figure 2.8. Top and cross sectional view of a UTC-PD showing its electrical equivalent circuit [88].

For these models, the electrical lumped elements equivalent to the UTC-PD model can be extracted from the one-port S-parameter measurements without illumination (S11 or S22), provided that the second port is kept disabled. As for the electrical elements that model the transit time of the photo-generated carriers and the responsivity, they can be extracted from the bandwidth (S21 or S12) and the photocurrent measurements, respectively.

In the absence of dedicated test-structures for device de-embedding, the electrical elements equivalent to pads and access lines are included in the overall model simulation, which makes the extraction of intrinsic parameters far less reliable. To overcome these shortcomings, de-embedding based on electromagnetic simulations of passive test structures can improve the extraction of intrinsic parameters [91], [92]. However, the imperfections in the fabrication process, on one hand, and the approximations and assumptions made during the simulation, on the other hand, can induce significant deviations in the results. The most realistic approach is therefore to fabricate and measure these de-embedding structures along with the photodiode.

Attempts to model the small signal equivalent electrical circuit including a more complex active region, were proposed by Natrella et al [93]. This was done because the simplified R-C model did not allow a correct interpretation of the measurement results. In the work of Natrella et al., the measurements show the appearances of poles and zeros at different frequencies. Two additional RC networks (Figure 2.9) have therefore been added to capture the behavior observed in the measurements. This modelling approach is justified by the fact that the presence of discontinuities in the conduction band leads to a charge accumulation. The first RC circuit represents the main active region (collector). The two other RC circuits represent the spacer layers, mainly inserted between the absorber and the collector layer, which are used to smooth the conduction band discontinuity at the *InGaAs/InP* heterojunction interface.

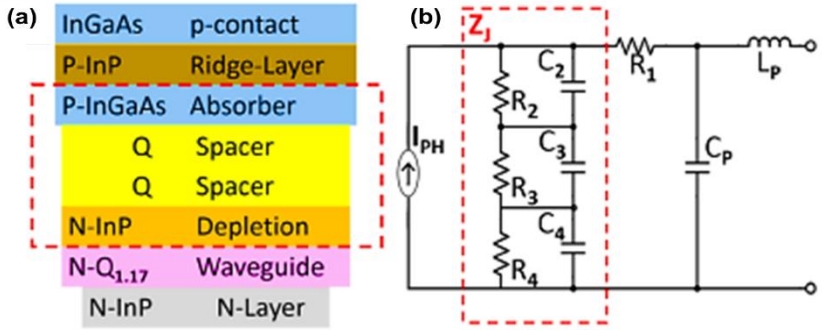

Figure 2.9. (a) UTC-PD layer structure (b) UTC-PD equivalent circuit, showing the relation with the UTC-PD structure [93].

2.3.1.1 Limitations of small signal modelling

The UTC-PD small signal models discussed before are simple to implement and easy/quick to simulate, but they have several limitations. The models are developed for a single operating bias point, typically for the optimal bias point. As a result, the models are not capable of handling bias changes. In addition, the material parameters are not correlated with the lumped elements of the electrical equivalent circuit. Moreover, the photo-generated carrier transit time calculation is not based on charge transport, but is rather modeled after the frequency-response of a first order low pass filter. Finally, the models are not scalable, i.e., for devices of different sizes, an optimization process is required to re-extract the values of the electrical equivalent circuit lumped elements from the model.

2.3.2 UTC-PD compact modelling

In 2020, Mukherjee et al. published the first UTC-PD compact model which was developed on the physical basis of UTC-PD charge transport [4]. The multi-physics model is versatile and is written in verilog-A, which makes it compatible with existing electronic circuit design tools. The analytical model equations capture the electronic transport and the frequency response of the photodiode without illumination as well as the photocurrent behavior as a function of different applied optical powers. To describe the temperature dependence, an additional thermal node consisting of an RC network to recalculate the device internal temperature has been added whose values have been determined by thermal simulations. This implementation describes the effect of self-heating at a given optical power and bias voltage. The model was validated on three UTC-PD geometries based on a technology developed by the University College London. These were *InGaAs/InP* waveguide integrated UTC-PDs in which the light is guided to the absorber by evanescent coupling.

In continuation of this previous work, this PhD thesis presents many improvements to the first compact model of the UTC-PD. Here we have introduced several new physical equations describing, in particular, the dark current, the intrinsic series resistance and the junction capacitance as well as their dependence on the applied bias. As a result, the new model now takes into account more material parameters such as doping, mobility and permittivity. Scaling laws have also been implemented by analyzing the UTC-PD geometry. Furthermore, we have developed the first accurate and physics-based Verilog-A SPICE compact model implementation for the complete analytic form of the photocurrent in UTC-PD.

2.3.2.1 Model formulation

Till now, several groups have made significant advances in UTC-PD design and modelling. However, until now, very few accurate and physics based compact or small signal models for UTC-PD devices have been reported.

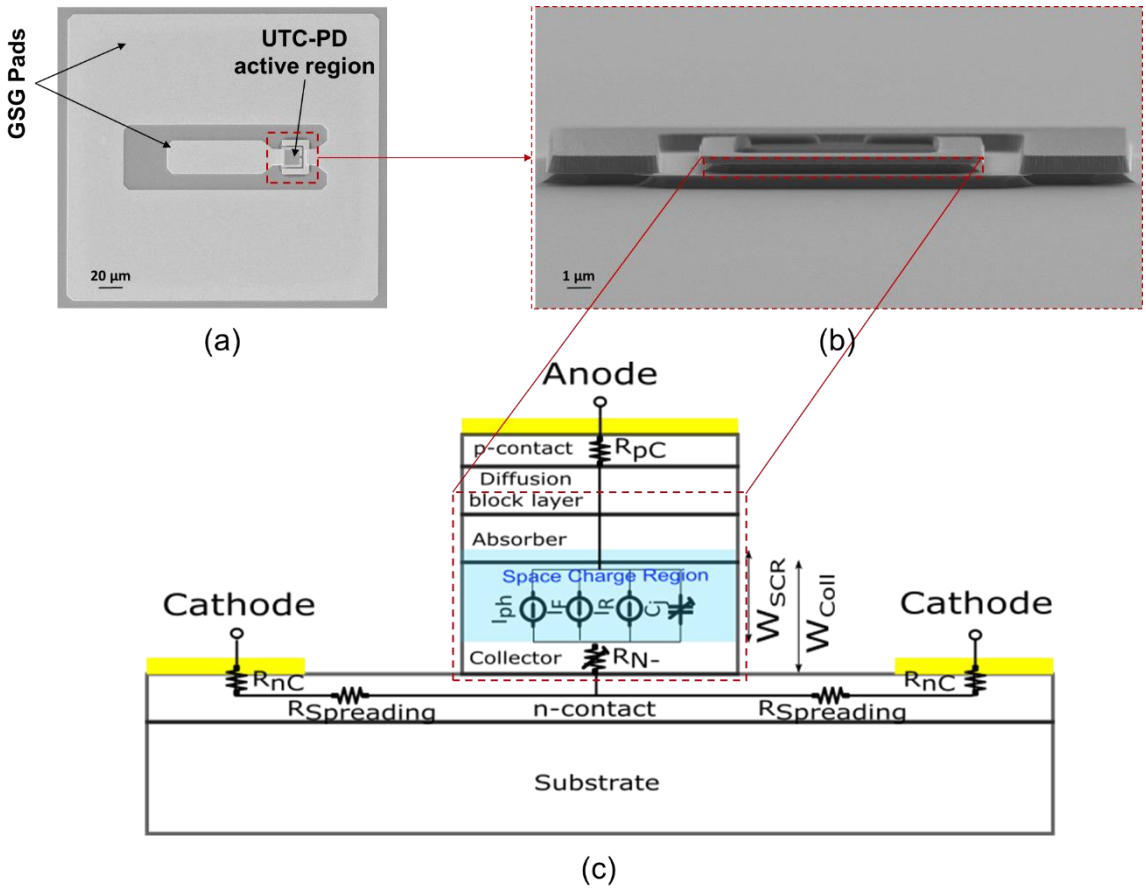

Figure 2.10. (a) Top-view of the SEM micrograph of a GaInAsSb/InP UTC-PD connected to the GSG RF pads (b) SEM micrograph of a GaInAsSb/InP UTC-PD (c) Schematic of the intrinsic mesa UTC-PD showing the location of the equivalent circuit elements.

Our UTC-PD compact model can be represented by an equivalent circuit with three terminals [94]. Among these terminals, two are for the electrical part and one for coupling the optical input signal. The model translates the analytical equations based on the physics of UTC-PDs into an equivalent electrical circuit representation. Figure 2.10 (a) shows the top view of the SEM micrograph of a GaInAsSb/InP UTC-PD connected to the Ground Signal Ground pads. Figure 2.10 (b) shows an SEM micrograph taken after the UTC-PD mesa formation. Figure 2.10 (c) illustrates the schematic of an intrinsic UTC-PD mesa structure, showing the schematic cross-section of the different epitaxial layers. On this schematic, the electrical equivalent circuit is superimposed depicting different electrical elements of the equivalent circuit representation. The active region consists principally of the epitaxial p-doped absorption layer and a lightly n-doped collection layer. The electrical representation of this region consists of a junction capacitance, C_j, which describes the absorber-collector junction. In parallel to this capacitance, three current sources model the forward current, the reverse current and the photocurrent, respectively. Note that, here the photocurrent implementation in Verilog-A is more complex than simple current source representations since it includes transfer functions. In series with the active region, there are resistances representing the resistive contribution of the non-depleted part of the collector, the spreading resistances and the resistances of the metal

contacts. The device can be biased via the doped P+ and N+ contacts at the top and the bottom, respectively. On both sides of the mesa, the access lines are connected to the GSG pads.

In the following section, we will detail the formulation of each electrical element of the UTC-PD compact model.

2.3.2.1.1 Junction capacitance

Modelling the junction capacitance is crucial for the compact modelling of UTC-PDs as it directly affects the dynamic response of the UTC-PD through the R-C delay.

After further investigation, the classical model of the bias-dependence of the junction capacitance (equation (2.21)) has evolved into a more mature form as described in the HiCuM/L2 model. We refer here mainly to the formulation for the base-collector junction since the UTC-PD is mainly operated under reverse bias.

$$\boldsymbol{C_j(V_d) = Area \cdot C_{j0}\left(1 - \frac{V_d}{V_j}\right)^{-M}} \qquad (\mathbf{2.21})$$

Where, C_{j0} is junction capacitance at zero bias per unit area, V_d is the applied bias, V_j is the built-in voltage of the junction and M is the grading coefficient which is associated to the grading doping profile (well-known example is $M = 1/2$ for step junction).

The classical theory is valid for p-n junction with a grading doping profile. In the case of a UTC-PD formed by a $P^+N^-N^+$ junction, the doping profile is not uniform in the whole structure. The n-doping, for example, increases from a low level in the collector to a high level in the n-contact. Similarly, the p-doping of the absorber may not be uniform. Consequently, the junction capacitance, which is related to the depleted space charge region, does not vary uniformly for all bias conditions. At low reverse bias, the junction capacitance follows the conventional model [95] until the doping profile changes and reaches its peak value, especially near the n-contact. As a result, depletion continues but with a weaker voltage dependence. Under reverse bias, the model of the junction capacitance, thus consists of two contributions as shown in the expression depicted by equation (2.22) [96], [97]. Here the first term, $C_{jm}(V_d)$, represents the contribution at medium reverse bias. The second part, $C_{jl}(V_d)$, represents the contribution that models the weaker dependence on the reverse bias around and beyond the condition of complete depletion of the collector.

$$\boldsymbol{C_{jT}(V_d) = Area \cdot \left[C_{j0m}\left(1 - \frac{V_d}{V_j}\right)^{-M_{mr}} + C_{j0l}\left(1 - \frac{V_d}{V_j}\right)^{-M_{lr}}\right]} \qquad (\mathbf{2.22})$$

Where M_{lr} and C_{j0l} can be calculated internally from the punch-through bias, V_{PT}, and M_{mr} using the following set of equations [96]:

$$\boldsymbol{V_{PT} = \frac{qN^-}{2\varepsilon_{Coll}} \cdot W_{Coll}^2} \qquad (\mathbf{2.23})$$

$$M_{lr} = \frac{M_{mr}}{4} \tag{2.24}$$

$$C_{j0l} = C_{j0m}\left(\frac{V_j}{V_{PT}}\right)^{(M_{mr}-M_{lr})} \tag{2.25}$$

Where, q is the electronic charge, N^{-}, ε_{Coll} and W_{Coll} are the collector doping level, permittivity and width respectively.

Following standard compact modelling practices, the capacitance contribution (equation 2.22) is actually implemented first by converting it to its equivalent charge, Q_{jT}, and then adding it to a current node by taking the time derivative of the charge, $\frac{dQ_{jT}}{dt}$.The equivalent charge is calculated as:

$$Q_{jT} = \int_0^{V_d} C_{jT}(V_d)dV_d \tag{2.26}$$

$$Q_{jT} = Area \cdot \left[\frac{C_{j0m}\cdot V_j}{1-M_{mr}}\cdot\left[1-\left(1-\frac{V_d}{V_j}\right)^{1-M_{mr}}\right]+\frac{C_{j0l}\cdot V_j}{1-M_{M_{lr}}}\cdot\left[1-\left(1-\frac{V_d}{V_j}\right)^{1-M_{lr}}\right]\right] \tag{2.27}$$

It should be noticed that in HiCuM/L2 formulation: (i) a correction term is added to the expression (2.22) (ii) the two contributing charges of the capacitance model are multiplied by smoothing functions (or weights) that result in a continuously differentiable function to ensure a smooth transition across the two adjacent bias regions.

To the best of our knowledge, there are currently no studies available in the literature on the dependence of the junction capacitance of UTC-PDs under bias voltage. Hence, we have validated equation (2.22) on a similar structure, the base-collector (BC) junction of an InGaAs/InP DHBT. Figure 2.11 shows the dependence of the BC junction capacitance on the reverse bias ($C_{BC} = f(V_{BC})$) for an InGaAs/InP DHBT comparing the classical and the proposed models [98]. From the figure, we note that at low reverse bias voltages, the two

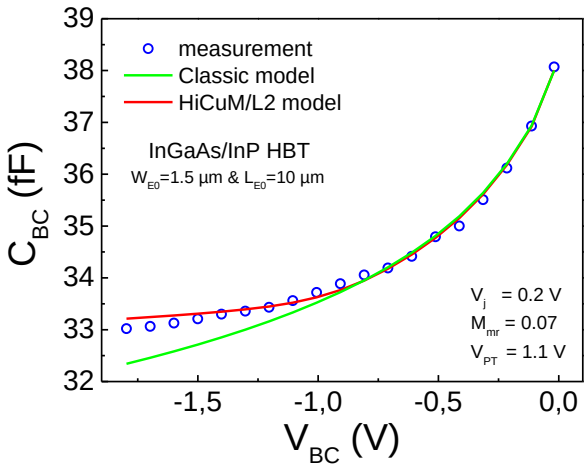

Figure 2.11. Base-Collector capacitance (C_{BC}) for InGaAs/InP DHBT as function of reverse bias (V_{BC}).

models give the same result. Above -1 V, the classical model does not follow the behavior of the device while the new implementation fits well due to the additional contribution taken into account.

2.3.2.1.2 Series resistances

The analysis of the total series resistance, R_s, of the UTC-PD is crucial, since it directly influences the dynamic response of UTC-PD, both on its bandwidth and on the output RF power. This can be understood by analyzing $I_L(\omega)$ which is the photocurrent, $I_{ph}(\omega)$, across the load resistance, R_L, as a function of the intrinsic electrical elements of UTC-PD as shown in the equation below:

$$\boldsymbol{I_L(\omega) = I_{ph}(\omega) \cdot \frac{1}{1 + j \cdot \omega \cdot C_j(V) \cdot (R_s + R_L)}} \quad (\mathbf{2.28})$$

Moreover, at high optical power, when the photocurrent becomes important, the applied voltage, V_{AK}, at the terminals of the UTC-PD appears across the series resistance. This voltage drop, proportional to the photocurrent, I_{ph}, becomes more significant as the series resistance becomes higher:

$$\boldsymbol{V_d = V_{AK} - I_{ph} \cdot R_s} \quad (\mathbf{2.29})$$

Therefore, a scalable analysis of the total series resistance, R_s, is the subject of the following section. The schematic in Figure 2.10 (c) illustrates the location of the individual series resistances.

One of the improvements made to the first model regarding the series resistance is the incorporation of a more detailed description of the series resistances by splitting the resistive contributions as a function of the applied bias and the device geometry. It is important to note that in the first version of the model, only one lumped series resistance, independent of the bias, was considered. This resistance took into account the contact resistance and the spreading resistance together.

As presented in Figure 2.10 (c), R_s is the sum of the resistances of the metal/semiconductor contact on the p-side, R_{pC}, the collector resistance due to the low doping of the collector, R_{N^-}, the n-side metal/semiconductor contact resistance, R_{nC}, and the spreading resistance of the n-contact semiconductor, $R_{Spreading}$. The total series resistance, R_s, of the UTC-PD can therefore be written as:

$$\boldsymbol{R_s = R_{pC} + R_{N^-} + \frac{1}{2}\left(R_{nC} + R_{Spreading}\right)} \quad (\mathbf{2.30})$$

In the following analyses, we will focus on the bias dependence and scalability laws for the total series resistance. For this purpose, we consider the case of a rectangular waveguide integrated UTC-PD. For circular geometry (circular mesa), the radius can be used in an equivalent analytical model development.

Assuming a uniform current density over the metal/semiconductor contact surface, the p-side contact resistance R_{pC} can be defined as follows:

$$\boldsymbol{R_{pC} = \frac{\rho_{pC}}{l_{mesa} \cdot w_{mesa}}} \quad (\mathbf{2.31})$$

Where ρ_{pC} is the specific contact resistance (in $\Omega.cm^2$), l_{mesa} and w_{mesa} are the length and the width of the contact, respectively.

The thickness and the doping level of the collector varies from one technology to another (usually N^- doped). When the collector is not fully depleted, an additional bias-dependent resistance, R_{N^-}, appears, which, when the collector is fully depleted, becomes negligible. The dependence of the R_{N^-} resistance on the applied voltage, V_d, can be expressed as follows [99]:

$$\mathbf{R_{N^-}(V_d) = \int_{w_{scr}(V_d)}^{w_{Coll}} \frac{1}{q \cdot \mu_{Coll} \cdot N^-} dx} \quad (\mathbf{2.32})$$

$$\mathbf{R_{N^-}(V_d) = \frac{w_{Coll} - w_{SCR}(V_d)}{q \cdot \mu_{Coll} \cdot N^- \cdot A}} \quad (\mathbf{2.33})$$

$$\mathbf{R_{N^-}(0) = \frac{w_{Coll} - w_{SCR0}}{q \cdot \mu_{Coll} \cdot N^- \cdot A}} \quad (\mathbf{2.34})$$

$$\boldsymbol{R_{N^-}(V_d) = R_{N^-}(0) \cdot \frac{w_{Coll} - w_{SCR}(V_d)}{w_{Coll} - w_{SCR0}}} \quad (\mathbf{2.35})$$

Where, $R_{N^-}(0)$ is the resistance of the undepleted collector at zero bias, w_{Coll} and μ_{Coll} are the width and the electron carrier mobility of the collector respectively, w_{SCR0} is the width of the space charge region (SCR) at zero bias. $w_{scr}(V_d)$ can be expressed with the following set of equations:

$$\boldsymbol{w_{scr}(V_d) = w_{SCR0}\left(1 - \frac{V_d}{V_j}\right)^{Mmr}} \quad (\mathbf{2.36})$$

Where V_j is the junction potential, and M_{mr} is the grading coefficient at medium reverse bias of the P-N^- junction, N^- is the doping concentration in the collector and A is the UTC-PD active area.

The resistances R_{nC} and $R_{Spreading}$ (equation 2.30) can be evaluated using the Linear Transfer Length Method (LTLM). For a three-dimensional semiconductor, the resistance can be expressed as a function of its geometry as follows:

$$\boldsymbol{R = \rho_{sc} \frac{l}{w \cdot t}} \quad (\mathbf{2.37})$$

Where ρ_{sc} is the resistivity, l is the length, w is the width and t is the thickness.

In the case of thin film semiconductors, a so-called sheet resistance is defined as follows:

$$\boldsymbol{R = R_{sheet} \cdot \frac{l}{w}} \qquad (\mathbf{2.38})$$

Where R_{sheet} is the sheet resistance in Ω/sq, which is normalized to a square geometry ($l = w$). Therefore, the R_{sheet} value that will be determined during extraction will need to be multiplied by the geometric factor ($l \,/\, w$) to find the exact value of the total resistance.

In a planar electrode, the distribution of the current density is not uniform across the metal/semiconductor contact surface (Figure 2.12 (a) and (b)), which is due to the lateral voltage drop. The current distribution can be calculated following the method described in [100], where the notion of transfer length, l_T, has been introduced (as illustrated in Figure 2.12 (b)) as function of the n-side contact resistivity, ρ_{nC}:

$$\boldsymbol{l_T = \sqrt{\frac{\rho_{nC}}{R_{sheet}}}} \qquad (\mathbf{2.39})$$

The transfer length represents the lateral distance over which the current density drops by a factor of $1 \,/\, e$ under the contact.

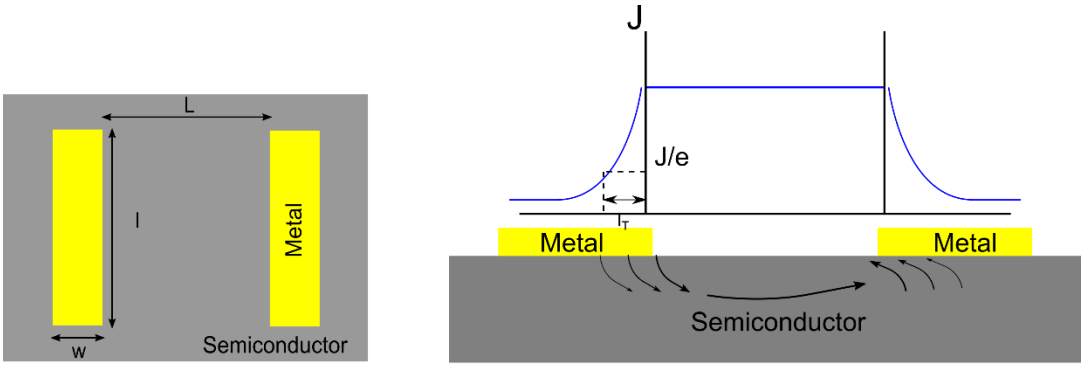

Figure 2.12. (a) Schematic of top view of two planar metal/semiconductor Ohmic contacts (b) Current density distribution between two planar metal/semiconductor Ohmic contacts.

The n-side contact resistance depends, therefore, on the transfer length and can be expressed as follows:

$$\boldsymbol{R_{nC} = \frac{\rho_{nC}}{l_T . l} coth\left(\frac{w}{l_T}\right)} \qquad (\mathbf{2.40})$$

For a metal contact of width greater than the transfer length, $w \gg l_T$, and by replacing l_T with its expression (equation 2.39), R_{nC} can be simplified to:

$$\boldsymbol{R_{nC} = \frac{\sqrt{\rho_{nC} R_{sheet}}}{l}} \qquad (\mathbf{2.41})$$

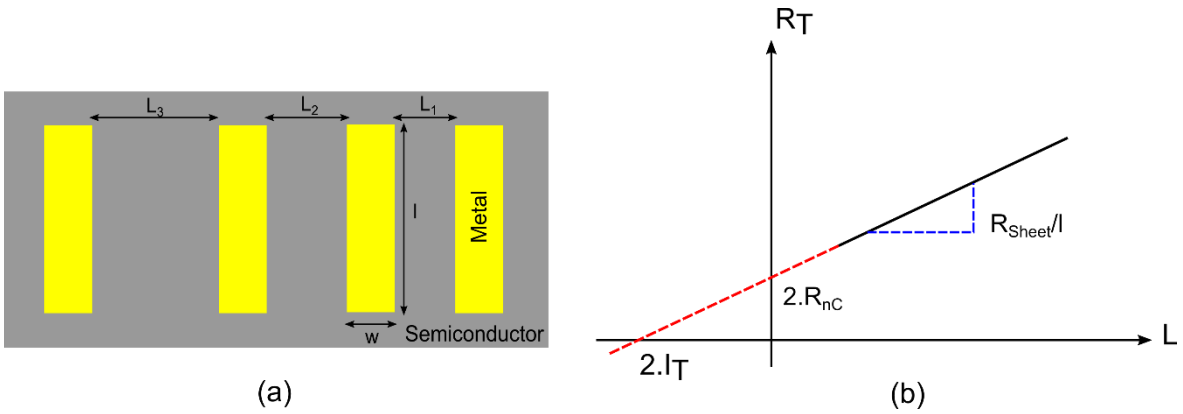

Figure 2.13. (a) Schematic of top view of the LTLM test structure (b) Plot of the total resistance between two planar metal/semiconductor Ohmic contacts as a function of the distance separating them.

Assuming that R_{sheet} is uniform along the semiconductor layer, the total resistance, R_T, between two contacts separated by a distance L can be written as follows:

$$\boldsymbol{R_T = 2R_{nC} + R_{Spreading} = 2.\frac{\sqrt{\rho_{nC}R_{sheet}}}{l} + \frac{R_{sheet}}{l}.L} \qquad (\mathbf{2.42})$$

Measurement of the total resistance as function of different distances, L_i, can be used to plot the curve $R_T = f(L_i)$. Linear regression on this curve allows one to extract the different parameters as illustrated in Figure 2.13 (a) and (b). The sheet resistance, R_{sheet}, can be determined from the slope of the curve $R_T = f(L_i)$. The specific n-contact resistance can be determined from the extrapolation of the curve at $L = 0$. The transfer length, l_T, can be extracted from the extrapolation of the curve at $R_T = 0$.

By replacing the resistances with their respective expressions and including the geometrical parameters of the UTC-PD in equation 2.30, the total resistance for a rectangular device geometry can be expressed as follows:

$$\boldsymbol{R_s = \frac{\rho_{pC}}{l_{mesa} \cdot w_{mesa}} + R_{N^-}(0) \cdot \frac{w_{Coll} - w_{SCR}(V_d)}{w_{Coll} - w_{SCR0}} + \frac{1}{2}\left(\frac{\sqrt{\rho_{nC}R_{sheet}}}{l_{mesa}} + \frac{L}{l_{mesa}} \cdot R_{Sheet}\right)} \qquad (\mathbf{2.43})$$

The resistance, R_s, determines the UTC-PD frequency response through equation (2.28). So minimizing its value can increase the bandwidth. Equation (2.43) indicates the parameters that we can control in order to minimize R_s. The geometrical parameters (l_{mesa} and w_{mesa}) cannot be adjusted freely, since they are optimized to maximize the absorption in the UTC-PD. So, the other parameters to investigate are the resistivity of the Ohmic contacts (ρ_{pC} and ρ_{nC}).

In equation (2.43), the first term depends linearly on the resistivity of the contact, $\boldsymbol{\rho_{pC}}$. The second term, for a fixed geometry and given material, depends mainly on the term $w_{Coll} - w_{SCR}(V_d)$. Finally, the third term features a square root dependence on the variations of the resistivity $\boldsymbol{\rho_{nC}}$.

To plot $\mathbf{R_s} = \boldsymbol{f}(\boldsymbol{\rho_{pC}}, \boldsymbol{\rho_{nC}})$, we took the structure and materials of the UTC-PD reported in [93], [101], as an example, whose length of the active region has been fixed at 15 µm with widths of 3 and 4 µm. The resistivity values found in the literature for *n-InP* and *p-InGaAs* Ohmic contacts are summarized in Table 2.1.

Table 2.1. Classical contacts resistivities on p-InGaAs and n-InP.

	Metallization	**Doping level (cm^{-3})**	**ρ_C ($\Omega.cm^2$)**	**R_{sheet} (Ω)**	**references**
p-InGaAs	Au/Pd/Ti/Pd	1×10^{19}	1.7×10^{-6}	-	[102]
	Al/W/Ti	2×10^{19}	3.3×10^{-6}	-	[103]
	Pd/AuGe	4×10^{19}	4×10^{-6}	-	[104]
	Au/Pd/Si/Gd	2×10^{19}	5.6×10^{-6}	-	[105]
n-InP	Au/Pt/Ti	1×10^{19}	8×10^{-6}	20.2	[106]

In the second term of equation (2.43), the collector thickness, w_{Coll}, and doping level, N^- were set to 300 nm [101] and $1 \times 10^{16}.cm^{-3}$ respectively. The mobility, μ_{Coll}, was set to 4500 $cm^2.V^{-1}.s^{-1}$ [107]. As the amount of depletion of the SCR was unknown, we considered that the SCR is depleted by half at equilibrium (at 0 Volt), and then we analyzed all possible values until the quantity $w_{Coll} - w_{SCR}(V_d)$ becomes zero, i.e., the SCR becomes completely depleted.

Also, it should be noted that for the evaluation of the third term in equation (2.43), $\boldsymbol{R_{sheet}}$ values are required. Since all $\boldsymbol{R_{sheet}}$ values were not found in the literature for every material's resistivity, we considered the only value reported, for the *n-InP* contact resistivity.

Figure 2.14 (a) and (b) show the values of the p-contact resistance, R_{pC}, and the values of collector resistance, $\boldsymbol{R_{N^-}(V_d)}$, for various UTC-PD widths respectively. In Figure 2.14 (c) and (d) we report theoretically calculated R_s for widths of 3 and 4 µm respectively. On the same plots we show in red R_s values the UTC-PDs reported in [93]. We notice that there is no unique solution for the parameters couple $f\left(\rho_{pC}, w_{Coll} - w_{SCR}(V_d)\right)$ for both geometries. Possible reasons for this deviation are the differences between the drawn contact and the real contact, as well as the possible technological dispersion.

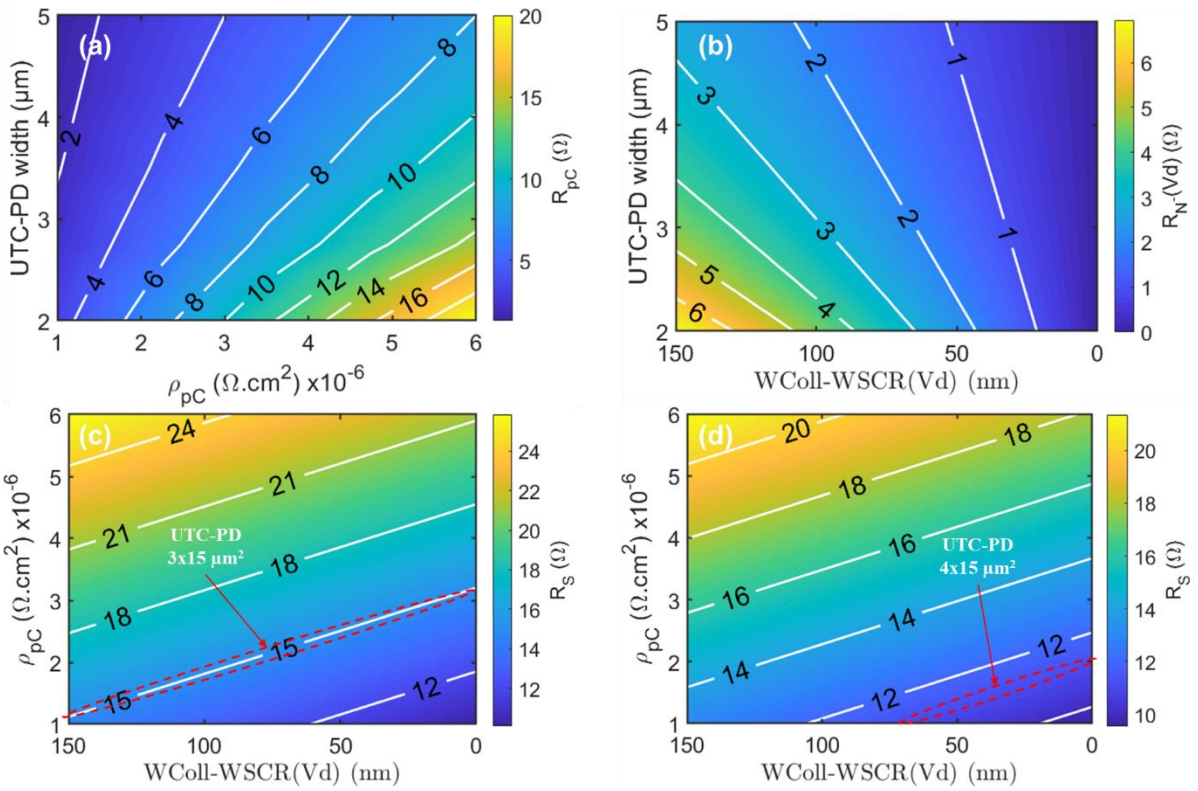

Figure 2.14. Theoretical calculation of the resistance from equation (2.43) for several values of resistivity and width of the UTC-PD (a) p-contact resistance R_{pC} (b) collector resistance $R_{N^-}(V_d)$. Global series resistance R_s for UTC-PD with an active area of (c) 3×15 µm² (d) 4×15 µm².

2.3.2.1.3 Dark current

The dark current in the previous work was developed based on a SPICE model for the P-N diode [95]. In this section, we will discuss the first proposed model and then present the improvements and arguments that were used to justify our choices.

a. Direct current

The forward current, I_D, of a photodiode can be described macroscopically by the classical intrinsic diode equation given by:

$$\boldsymbol{I_D = Area \cdot J_S(T) \cdot \left(e^{V_d / NV_t(T)} - 1\right)} \qquad (2.44)$$

Where N is the emission coefficient, $J_S(T)$ is the reverse saturation current density (reverse dark current), V_d is the forward bias applied across the photodiode and V_t is the thermal voltage. The temperature dependence of the $J_S(T)$ has been taken into account, as follows [95]:

$$\boldsymbol{J_S(T) = J_S\left(\frac{T}{T_0}\right)^{\frac{X_i}{N}} \cdot e^{\left[-\frac{E_g(T_0)}{V_t(T)}\left(1-\frac{T}{T_0}\right)\right]}} \quad (\mathbf{2.45})$$

Where, $E_g(T_0)$ is the temperature dependence of the energy band gap, T_0 is the nominal temperature, usually considered as the ambient temperature and X_i is a fitting parameter.

Indeed, this description of the diode DC current is valid for a single operating regime, such as low injection. For high forward bias voltage, the model is not adequate to fit the I-V characteristics. Therefore, overestimated values of the series resistance were employed. To overcome this difficulty, the forward current contribution, I_D, has been slightly modified by coupling the two operating regimes: low/medium and high injections . Thus, the forward current equation becomes the following [108]:

$$\boldsymbol{I_F = \frac{I_D}{1 + \sqrt{\frac{I_D}{I_K}}}} \quad (\mathbf{2.46})$$

Here I_D is the classic diode current under forward bias and I_K is the knee current parameter that signifies the transition between the medium and high injection regimes.

b. Reverse current

The dark current is the current in the photodiode when there is no incident light. In practice, it corresponds to the current generated when the photodiode is reverse biased in the absence of an optical input signal. Dark current is one of the contributing factors in the shot noise of a photodetector (equation (2.47)) [109], which can be one of the main sources of noise in the photodiode systems. Since the photo-current generated in the photodiode can be quite low under certain conditions, high dark current levels can mask the current produced by incident light at low optical powers, which can result in poor signal-to-noise ratio (SNR). Dark current is also a source of device power consumption when there is no signal to detect.

$$\boldsymbol{< i_s^2 >= 2 \cdot q.(I_{dark} + I_{ph})} \quad (\mathbf{2.47})$$

Where I_{dark} is the dark current and I_{ph} is the photocurrent.

In the previous work, the reverse bias current had four components, including the reverse saturation current I_{RS}, the reverse breakdown currents I_{RB} and I_{BV}, and the reverse leakage current I_{RL}, which used an expression similar to the interface state generation leakage current in p-i-n SOI diodes [110]. The individual expressions for the reverse current components are as follows [95]:

$$\boldsymbol{I_{RS} = -Area \cdot J_S(T), V_d \leq -5NV_t, I_{RB} = -I_{BV}, V_d = -BV} \quad (\mathbf{2.48})$$

$$\boldsymbol{I_{BV} = -Area \cdot J_S(T)\left(e^{-(BV+V_d)/V_t(T)} - 1\right), V_d < -BV} \quad (\mathbf{2.49})$$

$$\boldsymbol{I_{RL} = -Area \cdot J_R \cdot (T)^{1.5}\left(e^{-qE_g(T)/2k_BT}\right)V_d^2\sqrt{V_{bi} - V_d - V_t(T)}, V_d < -V_{ref}} \quad (\mathbf{2.50})$$

Here, BV is the reverse breakdown voltage, and E_g is the band gap of the absorption layer, V_{bi} is the junction built-in potential and V_{ref} is a threshold value of the reverse bias associated with the component I_{RL}.

In [110], the main contribution to the leakage current of a p-i-n diode under reverse bias is attributed to the thermal generation in the depleted space charge region (SCR). This leakage current expression was developed considering an applied potential on the back gate of the diode, which is not the case in majority of the UTC-PD structures. Therefore, we focused on a more general description of the dark current.

Due to the absence of dedicated test structures and the limited number of samples, i.e. one UTC-PD per geometry, determining the surface current contributions was not a straightforward task. Therefore, we considered that only the bulk current flows through the heterojunction stack of the epitaxial layers. The principal mechanisms at low reverse bias are diffusion and generation- recombination. While, contrastingly, at high reverse bias the tunneling processes are dominant.

In semiconductor materials, the crystalline quality of the junctions is very important for determining current conduction. Defects in the lattice structure and at the interfaces act as carrier generation/recombination states. These states act as active traps and contribute to the Shockley-Read-Hall current, I_{GR}, which is proportional to the intrinsic carrier concentration ($I_{GR}\ \alpha\ n_i$). The expression of I_{GR} is given by:

$$\boldsymbol{I_{GR} = \frac{qn_iW_{SCR}A}{\tau_{eff}}\left(e^{qV_d/2kT} - 1\right)} \quad (\mathbf{2.51})$$

Where τ_{eff} is the effective carrier life time and W_{SCR} is the space charge region width that can be estimated from a good approximation of the collector width, W_{Coll}.

Figure 2.15 shows I_{GR} values for different active areas of the device. Here the value of $\boldsymbol{\tau_{eff}}$ that has been used is 1 ns for the InP layer, as cited in reference [111]. $\boldsymbol{W_{Coll}}$ was then varied from 100 to 450 nm to cover the available collector widths of most of the UTC-PDs reported in the literature.

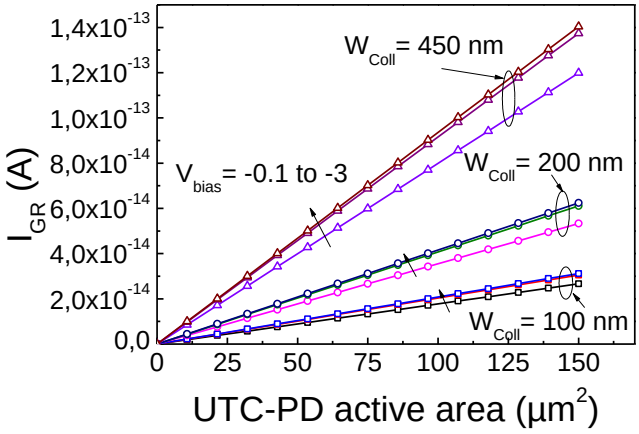

Figure 2.15. Generation-recombination current component as function of UTC-PD active area and reverse bias.

In addition to the generation- recombination current, there is also a diffusion current, I_{Diff}, originating from the thermally generated minority carriers that tend to diffuse to the SCR. I_{Diff} is proportional to the square of the intrinsic carrier concentration ($I_{Diff}\ \alpha\ n_i^2$) under low reverse bias.

In order to evaluate the contributions of the $\boldsymbol{I_{Diff}}$ currents in the UTC-PD, we take a simple $P^+N^-N^+$ structure formed by *p-InGaAs/n⁻-InP/n-InP* where the P^+N^- junction is dominant. In the case of UTC-PDs, the contribution of carriers generated on the N type side of the InP layer is neglected. This is because the intrinsic carriers concentration of the *InP* is negligible compared to that of *InGaAs* ($n_i(InP) \approx 10^{-4} \cdot n_i(InGaAs)$) [112]. Henceforth, we only consider the diffusion of minority electrons on the P side. The expression of I_{Diff} can therefore be reduced to:

$$\boldsymbol{I_{Diff} \approx qn_{i\_InGaAs}^2 \left(\sqrt{\frac{D_n}{\tau_n}}\frac{A}{N_A}\right)\left(e^{qV_d/kT} - 1\right)} \qquad (\mathbf{2.52})$$

Where, τ_n is the minority carrier life time of electrons, D_n is the minority carrier diffusion constant, A is the area of the SCR, N_A is the doping density.

For the calculation of I_{Diff}, physical parameters of the doped InGaAs layer from the literature were used (see Table 2.2).

Table 2.2. InGaAs material parameters used to calculate the diffusion current.

Physical parameter @ T = 300 K	***$In_{0.53}Ga_{0.47}As$***	**References**
$n_i\ (cm^{-3})$	5.4 x 10^{11}	[113]
$D_n(cm^2/s)$	67.6	[74]
$N_A\ (cm^{-3})$	1 x 10^{18}	
$\tau_n\ (ns)$	2	[114]

Figure 2.16 shows I_{Diff}values for different device active areas. These active areas have been chosen for UTC-PDs of high bandwidths, as reported in the literature.

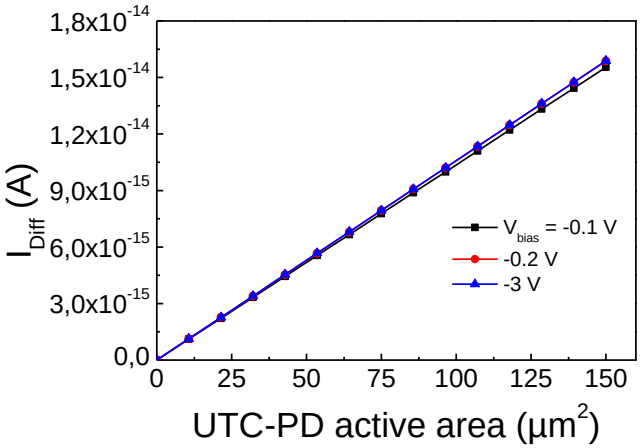

Figure 2.16. Diffusion current component as function of UTC-PD active area.

Figure 2.17 shows the ratio I_{GR}/I_{Diff} for three values of W_{Coll} and at saturation applied bias (-3 V). Clearly, the I_{GR} component is dominant. However, these quantities are difficult to extract from measurements since the sensitivity of our equipment is limited to pico-Ampere (~pA) currents. Moreover, both currents can be masked by surface currents, which makes an extraction even more complicated given the limited number of samples available (one sample per geometry). Therefore, the total contributions of the currents, I_{GR}, I_{Diff} and the surface, are all taken into account by the quantity I_{RS}.

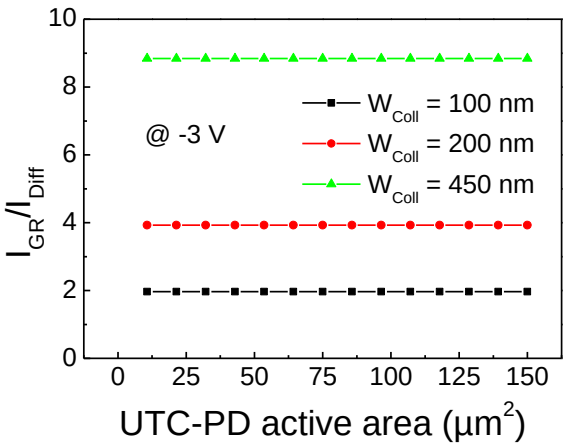

Figure 2.17. Diffusion and generation recombination currents ratio.

In small-gap semiconductor junctions, when the applied electric field is strong enough, the conduction and valence bands start to deform, and carriers can then tunnel through the barrier from the valence to the conduction band thus creating a current as illustrated in Figure 2.18.

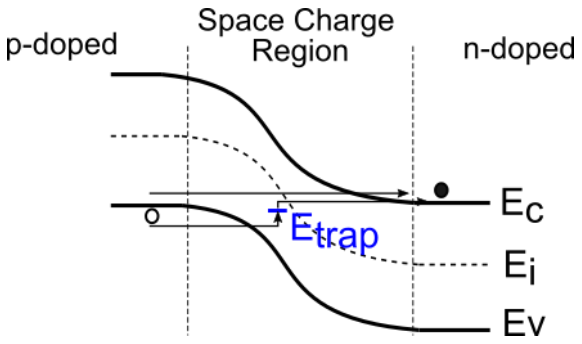

Figure 2.18. Band diagram showing tunnel currents mechanisms.

The band-to-band tunneling current, I_{BTB}, is calculated by considering a particle of given effective mass incident on a potential barrier. The complicated theoretical calculation is omitted to avoid the tedious extraction process of its numerous associated parameters, which include the effective mass of the charge carriers, the parameters related to the shape of the potential barrier, etc. Therefore, a simpler form of this tunneling current is used, which has been validated in many studies, especially at high reverse bias, and which can be expressed as follows [115]:

$$\boldsymbol{I_{BTB}(T) = Area \cdot A_{BTB} \cdot V_d \cdot E_{max}^2(T) \cdot e^{\left(-\frac{B_{BTB}}{E_{max}(T)}\right)}} \qquad (\mathbf{2.53})$$

Where A_{BTB} (in A/V^3) and B_{BTB} (in V/m) are parameters to be determined from model optimization, V_d is the UTC-PD applied bias in V and E_{max} is the maximum electric field (in V/m) at the collector input. E_{max} can be expressed as:

$$E_{max}(T) = \frac{C_{jT}(0)}{\varepsilon_{Coll} \cdot Area} \cdot \frac{\left(V_j(T) - V_d\right)^{1-M_{mr}} \cdot V_j(T)^{M_{mr}}}{(1 - M_{mr})} \quad (2.54)$$

Where C_{j0T} (in F) is the zero bias junction capacitance, ε_{Coll} is the collector's permittivity, V_j is the junction potential (in V) and M_{mr} is the grading coefficient of the junction at medium reverse bias.

At low reverse bias, the trap-assisted tunneling current is dominant. Typically, it is a Shockley-Read-Hall (SRH) generation current enhanced by tunneling effects. It can be expressed as follows [116]:

$$I_{TAT}(T) = Area \cdot A_{TAT} \cdot V_d \cdot E_{max}(T) \cdot e^{\left(-\frac{B_{TAT}}{E_{max}(T)}\right)} \quad (2.55)$$

Where A_{TAT} (in $A \cdot V^{-2} \cdot m^{-1}$) and B_{TAT} (V/m) are trap assisted tunneling current parameters. These parameters can be extracted from model optimization at low reverse bias.

2.3.2.1.4 Photocurrent

The photocurrent model that will be discussed next was originally developed by Ishibashi et al [73], [74]. It was developed with the drift-diffusion approach using the current continuity and Poisson's equation under short circuit condition. The model was developed for a simple UTC-PD structure with an absorption layer of thickness W_{Abs} and a collection layer of thickness W_{Coll} as illustrated in Figure 2.19.

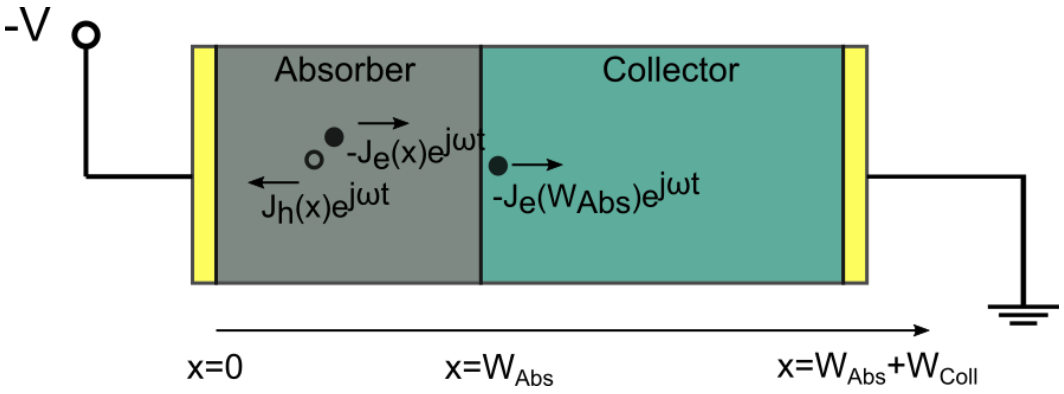

Figure 2.19. Schematic illustration depicting the analysis of the UTC-PD photocurrent.

In [74], Ishibashi et al. developed an improved formulation of the total photocurrent density, $J_{ph}(\omega)$, obtained by following current continuity across the absorber and the collector regions:

$$J_{ph}(\omega) = J_{Abs}(\omega) + j\frac{\omega\varepsilon_{Abs}}{W_{Abs}}V_{Abs}(\omega) + J_{adj}(\omega) \quad (2.56.a)$$

$$= J_{Coll}(\omega) + j\frac{\omega\varepsilon_{Coll}}{W_{Coll}}V_{Coll}(\omega) \quad (2.56.b)$$

Where $J_{Abs}(\omega)$ and $V_{Abs}(\omega)$ are the photocurrent and voltage drop in the absorber, respectively. $J_{Coll}(\omega)$ and $V_{Coll}(\omega)$ are the photocurrent and voltage drop in the collector layer, respectively. $J_{Abs}(\omega)$ and $J_{Coll}(\omega)$ are given as functions of their transfer functions as follows:

$$\boldsymbol{J_{Abs}(\omega) = -qG(\omega)\frac{1}{1+\omega\tau_{adj}}} \quad (\mathbf{2.57})$$

$$\boldsymbol{J_{Coll}(\omega) \approx -qG(\omega)\frac{1}{1+j\omega\tau_a}\frac{sin\left({}^{\omega\tau_c}/_{2}\right)}{{}^{\omega\tau_c}/_{2}}\cdot e^{-j\cdot\frac{\omega\cdot\tau_c}{2}}} \quad (\mathbf{2.58})$$

$$\mathbf{With\ \tau_a = \left(\frac{W_{Abs}^2}{3D_e} + \frac{W_{Abs}}{v_{th}}\right)\ and\ \tau_c = \frac{W_{Coll}}{v_C}}$$

Here, $G(\omega)$, is electron-hole pair generation rate uniformly distributed over the absorber of thickness W_{Abs}, v_{th} and v_c are thermionic and carrier saturation velocities in the absorber and collector, respectively, and D_e is the electron diffusion coefficient in the absorber.

As $J_{Abs}(\omega)$ and $J_{Coll}(\omega)$ differ in amplitude and phase, an additional current term $J_{adj}(\omega)$ was added to satisfy the current continuity.

For the terminal voltage of the photodiode to be zero in the case of a short circuit, it must maintain the balance:

$$\boldsymbol{j\frac{\omega\varepsilon_{Abs}}{W_{Abs}}V_{Abs}(\omega) = -j\frac{\omega\varepsilon_{Coll}}{W_{Coll}}V_{Coll}(\omega)} \quad (\mathbf{2.59})$$

The term $J_{adj}(\omega)$ is given by equation (2.60) and approximated by equation (2.61) [74]:

$$\boldsymbol{J_{adj}(\omega) = -2j\frac{\omega\varepsilon_{Abs}}{W_{Abs}}V_{Abs}(\omega)} \quad (\mathbf{2.60})$$

$$\boldsymbol{J_{adj}(\omega) \approx -j\omega C_{Abs}R_{Abs}J_{Abs}(\omega) = -j\omega\tau_{adj}J_{Abs}(\omega)} \quad (\mathbf{2.61})$$

Where C_{Abs} and R_{Abs} are absorber capacitance and resistance respectively. The product $C_{Abs}R_{Abs}$ is the adjusment time τ_{adj} and it is estimated to be serval tens of **femtoseconds** for a *p-InGaAs* absorber with low resistivity and small thickness (W_{Abs}= 100 nm). At low frequency (< 500 GHz) $\omega\tau_{adj} \ll 1$. Therefore, the collector displacement current $-j\frac{\omega\varepsilon_{Coll}}{W_{Coll}}V_{Coll}(\omega)$ (second term in equation (2.56.b)) can be ignored and $J_{ph}(\omega)$ becomes:

$$\boldsymbol{J_{ph}(\omega) \approx -qG(\omega)\frac{1}{1+j\omega\tau_a}\frac{sin\left({}^{\omega\tau_c}/_{2}\right)}{{}^{\omega\tau_c}/_{2}}\cdot e^{-j\cdot\frac{\omega\cdot\tau_c}{2}}} \quad (\mathbf{2.62})$$

Assuming that the sinusoidal generation rate G(ω) is constant throughout the absorption region, $\boldsymbol{W_{Abs}}$, one can rewrite the above as:

$$\mathbf{I_{ph}(\omega) \approx -I_{ph0} \cdot \frac{1}{1 + j \cdot \omega \cdot \tau_a} \cdot \frac{\sin\left(\omega\tau_c/2\right)}{\omega\tau_c/2} \cdot e^{-j\cdot\frac{\omega\cdot\tau_c}{2}}} \qquad (2.63.a)$$

This expression can be also found in [117].

In the following section, a comprehensive analysis of equivalent circuit implementations of the frequency-domain photocurrent model for UTC-PDs is developed based on the analytical equations discussed previously by incorporating charge carrier transit times, UTC-PD geometry and material parameters.

Figure 2.20 illustrates the complete electrical equivalent circuit representation of the first compact model developed for the UTC-PDs [4]. The compact SPICE modelling and

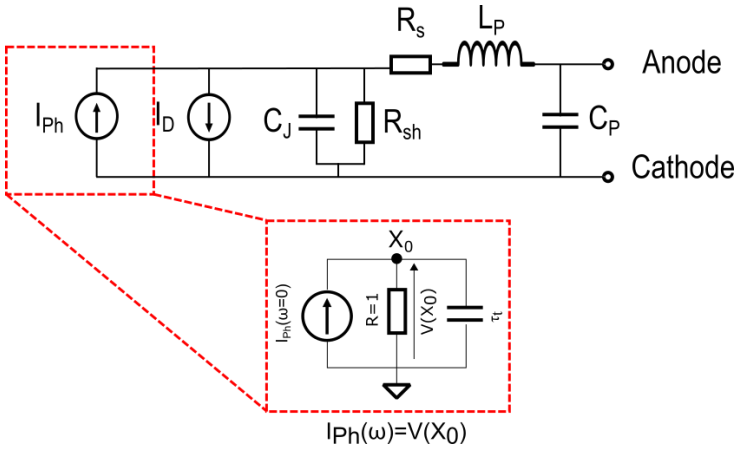

Figure 2.20. UTC-PD electrical equivalent circuit showing photocurrent implementation using low pass filter approximation.

implementation of the dynamic photocurrent behavior is not straightforward due to the complex frequency dependence of the sinusoidal and exponential functions present in the analytical current equation (2.63.a).

Direct frequency-domain implementations of ***sin*** and ***exponential*** functions in Verilog-A are not possible and therefore no SPICE Verilog-A model exists till date that takes into account the complete equation (2.63.a). As an approximation, the dynamic behavior in equation (2.63.a) can be represented using a single pole low-pass filter (LPF) R-C network to model the frequency roll-off. The additional electrical equivalent circuit uses a unit resistance (in Ω) and a capacitance value τ_t (in F) in parallel, fed by a current source I_{ph0}, which implements the transfer function $I_{ph}(w) = I_{ph0}/(1 + j\omega\tau_t)$ (Figure 2.20). However, this largely overestimates the analytical solution as frequency increases. Moreover, this approximation accounts for only one type of carrier in a unipolar region and thus lacks the physical basis of carrier transport in real devices like p-i-n PDs or UTC-PDs.

Considering absorber and collector thicknesses of 100 to 225 nm, respectively, a v_{th} of 2.5×10^7 cm/s as well as a v_C of 10^7 cm/s and a D_e of 5000 $cm^2.V^{-1}.s^{-1}$ for an InGaAs/InP UTC-PD, the magnitude and the phase of the normalized frequency response $I_{ph}(\omega)/I_{ph0}$ are plotted in Figure 2.21 for both the analytical equation and the single pole LPF approximation.

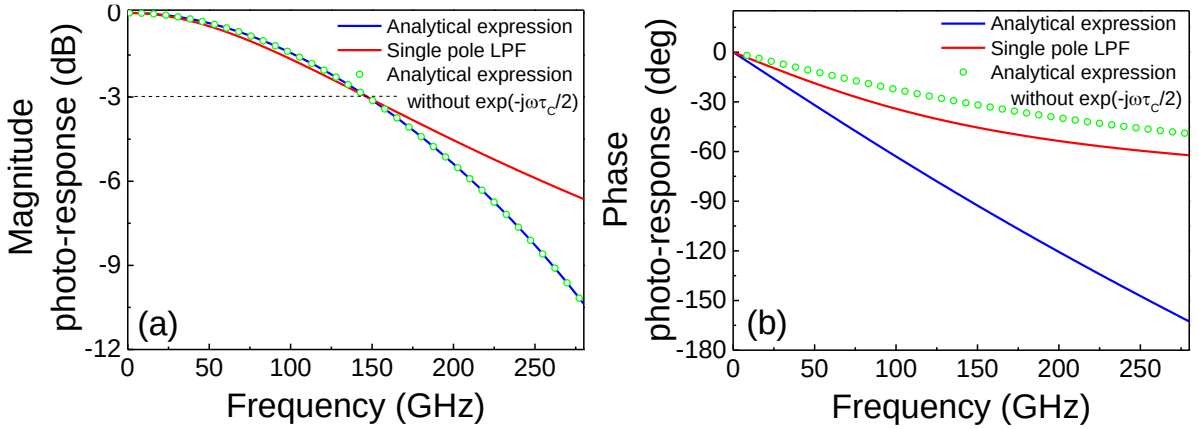

Figure 2.21. Normalized photoresponse of UTC-PD comparing the analytical and single pole LPF approximate solutions (a) magnitude in dB (b) phase in degree.

Clearly, the approximation starts to deviate from the analytical solution at frequencies around its 3-dB cut-off frequency. This implementation, thus, does not meet the criteria for design of high-speed optoelectronic circuits using SPICE. Interestingly, only the phase of the photocurrent is governed by the $e^{-j\frac{\omega\tau_C}{2}}$ term in expression (2.63.a) and without this term, the phase of the photocurrent in (2.63.a) reduces to that of the single pole LPF implementation (Figure 2.21 (b)) even though its magnitude remains the same as that of analytical expression (2.63.a). Even though 3-dB bandwidth and RF output power are both calculated from simply the magnitude of the photoresponse, the phase is important from the system perspective as it is dependent on the optical energy. Phase variations often come with excess phase noise and can thus impede demodulation [118]. Hence, it is important that the SPICE implementations also capture the phase of the photo-response accurately along with the magnitude of the photocurrent.

In this PhD work, we present the first SPICE implementation of an accurate and computationally efficient Verilog-A model for the complete analytical expression of photocurrent in UTC-PDs. Our proposed implementation methodology is not technology-specific and can be extended for other photonic devices such as high-bandwidth (>200 GHz) p-i-n PDs [119].

The main idea behind this work was to develop an analytical model that captures the dynamic photocurrent behavior of UTC-PDs by approximating equation (2.63.a) as closely and accurately as possible. This model should also be easily implementable in Verilog-A for the

existing SPICE simulation framework. To overcome the limitations of the single pole LPF approximation and to preserve the accuracy of equation (2.63.a) as much as possible, it is essential to simplify $sinc\left(\frac{\omega\cdot\tau_c}{2}\right)e^{-j\cdot\frac{\omega\cdot\tau_c}{2}}$ into a more computationally convenient form:

$$\boldsymbol{I_{ph}(\omega) = I_{ph}(\omega=0)\cdot\frac{1}{1+j\omega\tau_a}\cdot\frac{\left(e^{j\frac{\omega\tau_c}{2}}-e^{-j\frac{\omega\tau_c}{2}}\right)}{2\cdot j\frac{\omega\tau_c}{2}}\cdot e^{-j\frac{\omega\tau_c}{2}}} \qquad (\mathbf{2.63.b})$$

$$\boldsymbol{I_{ph}(\omega) = I_{ph0}\cdot\frac{1}{1+j\omega\tau_a}\cdot\frac{\left(1-e^{-j\cdot\omega\tau_c}\right)}{j\omega\tau_c}} \qquad (\mathbf{2.63.c})$$

As a first approach, the exponential can be substituted by its Taylor series representation. Considering a fourth-order expansion, and substituting the Laplace variable $s = j\omega$ in (2.63.c), the representation in the frequency domain can be written as follows:

$$\boldsymbol{I_{ph}(s) = I_{ph0}\frac{1}{1+s\tau_a}\cdot\left(1-\frac{s\tau_c}{2}+\frac{(s\tau_c)^2}{6}-\frac{(s\tau_c)^3}{24}\right)} \qquad (\mathbf{2.64.a})$$

In order to implement the equation (2.64.a) in Verilog-A, one must consider that the Laplace variable, s, actually represents the time derivative, $\boldsymbol{ddt}$. For the Verilog-A implementation, equation (2.64.a) must be rearranged and decomposed into single-pole network segments as follows:

$$\mathbf{I_{ph}(s) = V(X_0) - \frac{s\tau_c}{2}\cdot\left(V(X_0) - \frac{s\tau_c}{3}V(X_0) + \frac{s\tau_c}{4}\left(\frac{s\tau_c}{3}V(X_0)\right)\right)} \qquad (\mathbf{2.64.b})$$

$$\boldsymbol{With\ V(X_0) = I_{ph0}\frac{1}{1+s\tau_a}}$$

$$\boldsymbol{I_{ph}(s) = V(X_0) - \frac{s\tau_c}{2}\cdot\left(V(X_0) - V(X_1) + V(X_2)\right)} \qquad (\mathbf{2.64.c})$$

$$\mathbf{With,}\ \boldsymbol{V(X_1) = \frac{s\tau_c}{3}\cdot V(X_0)\ and\ V(X_2) = \frac{s\tau_c}{4}\cdot V(X_1)}$$

$$\boldsymbol{I_{ph}(s) = V(X_0) - V(X_4) = V(X_5)} \qquad (\mathbf{2.64.d})$$

$$\boldsymbol{With, V(X_3) = V(X_0) - V(X_1) + V(X_2)\ and\ V(X_4) = \frac{s\tau_c}{2}\cdot V(X_3)}$$

Equations (2.64.b)-(2.64.d) can be used to construct single-pole equivalent circuits for nodes X_0 through X_5 using Kirchoff's current law at each of these nodes in terms of lumped R, L, or C elements, as shown in Figure 2.22. Note that while equation (2.64.a) is still feasible for a Verilog-A implementation, it is quite computationally exhausting and requires 6 additional nodes in the equivalent electrical circuit of the photodiode, as shown in Figure 2.22.

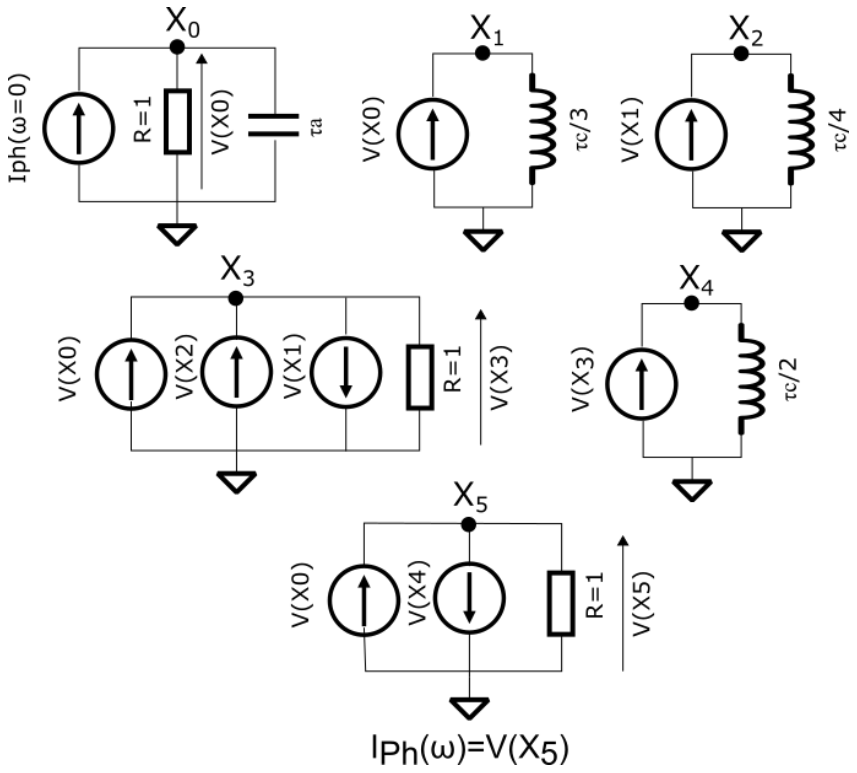

Figure 2.22. UTC-PD photocurrent electrical equivalent circuit for the Taylor approximation.

Considering absorber and collector thicknesses ranging from of 80 to 200 nm and collector thicknesses ranging from 100 to 450 nm, a v_{th} of 2.5×10^7 cm/s as well as a v_C of 10^7 cm/s and a μ_e of 5000 cm^2.V^{-1}.s^{-1} for an InGaAs/InP UTC-PD, the normalized magnitude photoresponse $\left(I_{ph}(\omega)/I_{ph0}\right)$, at – 3dB, for the analytical expression is calculated and plotted in Figure 2.23 (a). The dimensions were chosen based on the most commonly reported UTC-PD geometries

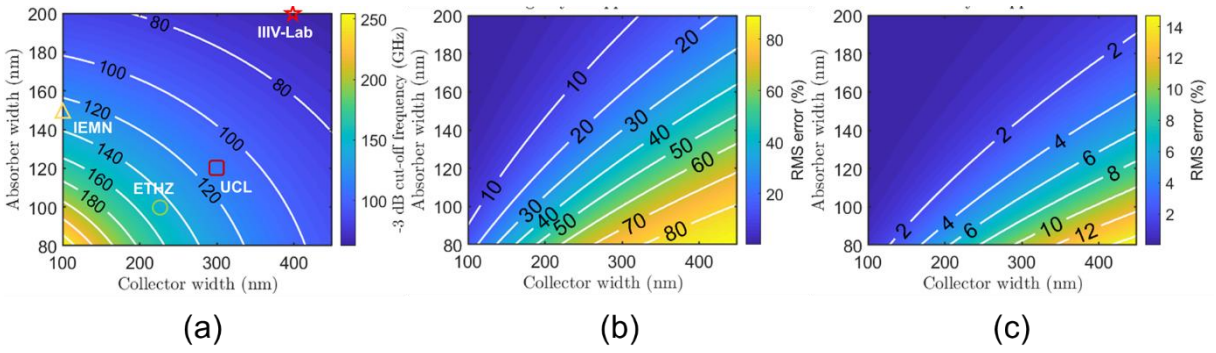

Figure 2.23. (a) Cut-off frequencies at – 3 dB of different UTC-PD technologies; RMS error comparing the analytical form of the photocurrent (eq. 62.c) with the Taylor approximation method (b) magnitude (c) phase.

in the literature [82], [101], [120], [121]. Figure 2.23 (b) and (c) shows the calculation of the RMS (Root Mean Square) for the magnitude and the phase error between the analytical expression and the Taylor series approximation. For the magnitude, the RMS ranges from 3% up to more than 80% depending on the geometry of the UTC-PD. For the smallest geometries and in the frequency range of a few hundreds of GHz, the transit time is small and therefore the term $\omega\tau_c$ remains close to zero making the approximation valid. Beyond that, the product $\omega\tau_c$ deviates from zero and the Taylor series approximation no longer remains valid. Regarding the phase, the Taylor approximation is quite tolerable (RMS<10%).

To investigate other approximations in order to reduce computational time and provide better accuracy, we explored the Padé approximation [122] to represent the exponential form in equation (2.63.c). We first started with the Padé (1, 1) approximation from Padé table. The exponential is approximated to:

$$\boldsymbol{e^{-j\omega\tau_c} \approx \frac{1-\frac{j\omega\tau_c}{2}}{1+\frac{j\omega\tau_c}{2}}} \qquad (\mathbf{2.65})$$

Using this approximation, the photocurrent equation (2.63.c) is reduced to:

$$\boldsymbol{I_{ph}(s) = I_{ph0}\frac{1}{1+s\tau_a}\cdot\left(\frac{1}{1+\frac{s\tau_c}{2}}\right)} \qquad (\mathbf{2.66})$$

The implementation of equation (2.66) requires only two nodes and is simpler than equation (2.64.a). Equation (2.66) can be translated into Verilog-A by representing each pole by its equivalent RC network. To do this, the corresponding Kirchoff current equation can be written for each node in terms of node currents and voltages. The capacitive elements are represented by the time derivatives, $\boldsymbol{ddt}$, of the node voltages to replace the Laplace variables (see Figure 2.24 (a)). Both equations can now be implemented in Verilog-A and solved simultaneously for $V(X1)$, which essentially provides the solution for $I_{ph}\ (s)$.

$$\boldsymbol{I_{ph}(0) - V(X_0) - ddt\left(\tau_a \cdot V(X_0)\right) = 0} \qquad (\mathbf{2.67.a})$$

$$\boldsymbol{V(X_0) - V(X_1) - ddt\left(\frac{\tau_c}{2}\cdot V(X_1)\right) = 0} \qquad (\mathbf{2.67.b})$$

However, as shown in Figure 2.24 (b) and (c), the accuracy of equation (2.66) is not sufficient over the entire frequency range, mainly regarding the magnitude. Therefore, we explored other approximations from the Padé table.

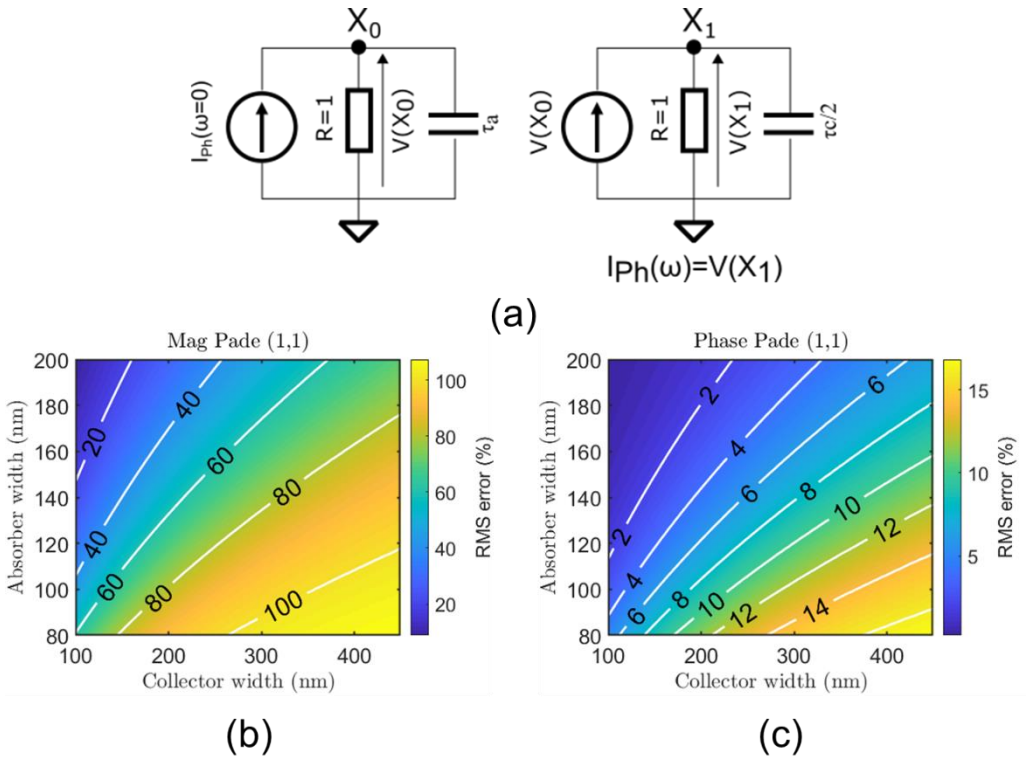

Figure 2.24. (a) UTC-PD photocurrent electrical equivalent circuit of the Padé (1,1) approximation; RMS error in (b) magnitude and (c) phase compared the analytical solution to Padé (1,1).

Similar to the analysis presented for Padé (1, 1), we approximated (2.63.c) using the Padé (2, 1) and Padé (3, 1) expansions to obtain the following approximations of the analytical solution in the Laplace domain, respectively:

$$\boldsymbol{I_{ph}(s) = I_{ph0}\frac{1}{1+s\tau_a}\cdot\left(\frac{1-\frac{s\tau_c}{6}}{1+\frac{s\tau_c}{3}}\right)} \qquad \boldsymbol{(2.68)}$$

$$\boldsymbol{I_{ph}(s) = I_{ph0}\frac{1}{1+s\tau_a}\cdot\left(\frac{1-\frac{s\tau_c}{4}+\frac{(s\tau_c)^2}{24}}{1+\frac{s\tau_c}{4}}\right)} \qquad \boldsymbol{(2.69)}$$

Based on the same methodology presented in the previous paragraph, the translation of equations (2.68) into Verilog-A requires 3 nodes (see Figure 2.25). The node current equations in the Verilog-A implementation can be expressed as follows:

$$\boldsymbol{I_{ph}(0) - V(X_0) - ddt\left(\tau_a \cdot V(X_0)\right) = 0} \qquad (\mathbf{2.70.}\boldsymbol{a})$$

$$\boldsymbol{V(X_0) - \frac{V(X_1)}{s\tau_c/6} = 0} \qquad (\mathbf{2.70.}\boldsymbol{b})$$

$$\boldsymbol{V(X_1) - ddt\left(\frac{\tau_c}{6} \cdot V(X_0)\right) = 0} \qquad (\mathbf{2.70.}\boldsymbol{c})$$

$$\boldsymbol{V(X_0) - V(X_1) - ddt\left(\frac{\tau_c}{3} \cdot V(X_2)\right) - V(X_2) = 0} \qquad (\mathbf{2.70.}\boldsymbol{d})$$

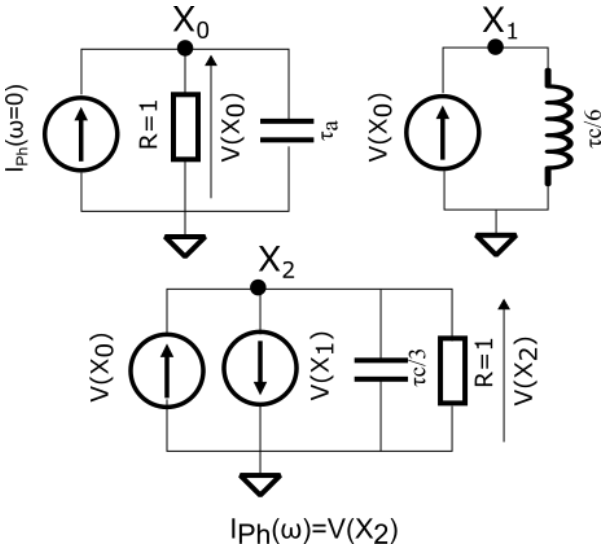

Figure 2.25. Electrical equivalent circuit of the Padé (2,1) approximation.

Similarly for the Padé (3, 1) expansions, the implementation of equation (2.69) in Verilog-A requires 5 nodes (see Figure 2.26). The node current equations for the Verilog-A implementation can be expressed as follows:

$$\boldsymbol{I_{ph}(0) - V(X_0) - ddt(\tau_a \cdot V(X_0)) = 0} \qquad (\mathbf{2.71.}\boldsymbol{a})$$

$$\boldsymbol{V(X_0) - \frac{V(X_1)}{s\tau_c/24} = 0} \qquad (\mathbf{2.71.}\boldsymbol{b})$$

$$\boldsymbol{V(X_2) - \frac{V(X_3)}{s\tau_c} = 0} \qquad (\mathbf{2.71.}\boldsymbol{c})$$

$$\boldsymbol{\frac{V(X_0)}{4} - V(X_1) - V(X_2) = 0} \qquad (\mathbf{2.71.}\boldsymbol{d})$$

$$\boldsymbol{V(X_0) - V(X_3) - ddt(\frac{\tau_c}{4} \cdot V(X_4)) - V(X_4) = 0} \qquad (\mathbf{2.71.}\boldsymbol{e})$$

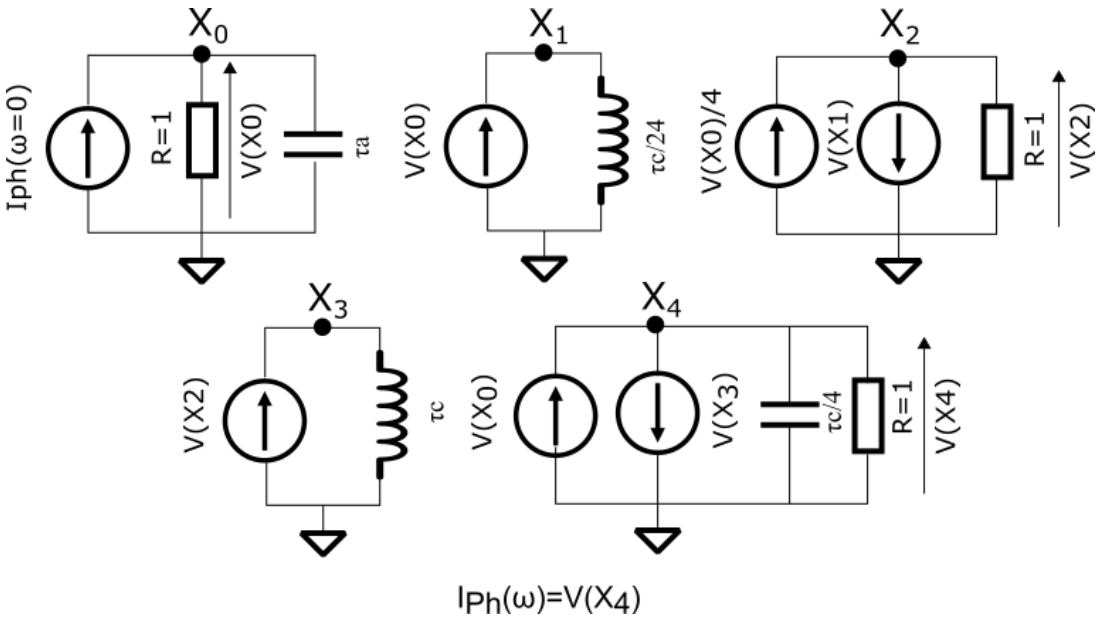

Figure 2.26. Electrical equivalent circuit of the Padé (3,1) approximation.

By calculating the RMS error between the fully analytical model and the approximations of equations (2.68) and (2.69), we note that as observed from Figure 2.27, the RMS error on the magnitude remains small only for a very limited range of device geometries and may be greater than 20% for some device geometries for both cases. Thus, the accuracies of these approximations are still not sufficient to obtain reliable simulation results. Note that, considering a trade-off between computational load and model accuracy, Padé (2, 1) should be preferred to Padé (3, 1).

In order to reduce the number of nodes and the RMS error, we propose a new implementation leveraging the Taylor series for the exponential term in equation (2.63.c). This new implementation not only ensures a very high accuracy of the model over a wide range of frequencies (up to 300 GHz) but also optimizes the computational load by limiting the polynomial expansion to its third order, thus limiting the number of required additional nodes to 3 in its Verilog-A implementation . First, equation (2.63.c) in the Laplace domain is rewritten as follows:

$$\boldsymbol{I_{pha}(s) = I_{ph}(s) \cdot \frac{s\tau_c}{(1 - e^{-s\tau_c})}} \qquad \boldsymbol{(2.72)}$$

$$\boldsymbol{With\ I_{pha}(s) = I_{ph0}\frac{1}{1 + s\tau_a}}$$

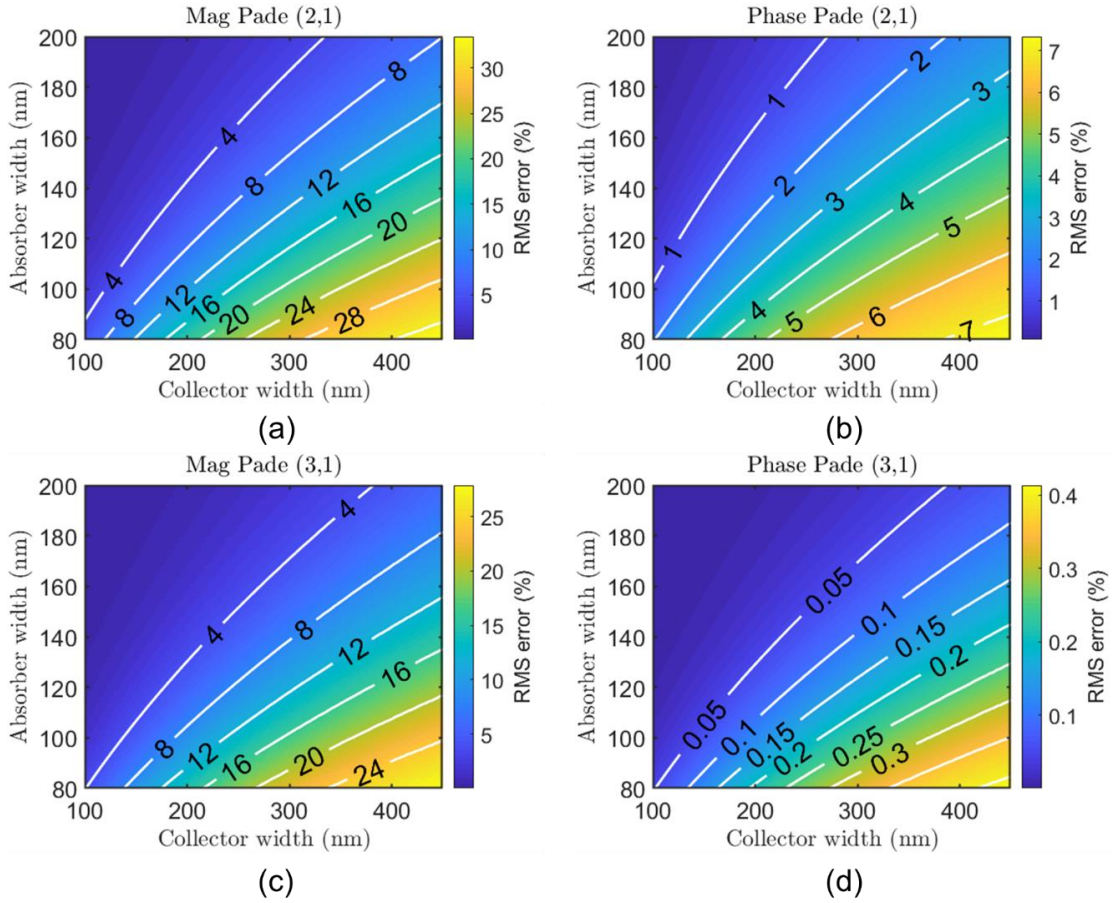

Figure 2.27. RMS error in magnitude and phase compared the analytical solution to (a) and (b) Padé (2,1); (c) and (d) Padé (3,1).

By considering that $s\tau_c/(1-e^{-s\tau_c})$ has a polynomial expansion of the form $[C_0 + C_1(s\tau_c) + C_2(s\tau_c)^2 + \cdots]$ and substituting the Taylor series for $e^{-s\tau_c}$, we can solve for the values of the coefficients C_0, C_1 and C_2:

$$\frac{s\tau_c \cdot e^{s\tau_c}}{(e^{s\tau_c}-1)} = C_0 + C_1(s\tau_c) + C_2(s\tau_c)^2 + \cdots \qquad (2.73.a)$$

$$s\tau_c \cdot \left(1 + s\tau_c + \frac{(s\tau_c)^2}{2} + \frac{(s\tau_c)^3}{6} + \cdots\right) = \left(C_0 + C_1(s\tau_c) + C_2(s\tau_c)^2 + \cdots\right) \cdot \left(s\tau_c + \frac{(s\tau_c)^2}{2} + \frac{(s\tau_c)^3}{6} + \cdots\right) \qquad (2.73.b)$$

Solving on both sides the coefficients of the polynomial, we obtain $C_0 = 1$, $C_1 = 1/2$ and $C_2 = 1/12$. By limiting the expansion to its 3rd order and rewriting (2.72) using these values, we obtain:

$$I_{pha}(s) = I_{ph}(s)\left[1 + \frac{s\tau_c}{2} + \frac{(s\tau_c)^2}{12}\right] \qquad (2.74.a)$$

$$I_{ph}(s) = \frac{I_{pha}(s)}{\left[1 + \frac{s\tau_c}{2} + \frac{(s\tau_c)^2}{12}\right]} \qquad (2.74.b)$$

Following the previous methodology, equation (2.74.b) can be represented in terms of the current equations for the three nodes (see Figure 2.28 (a)). Using Kirchoff's current law, one can thus write the model equations for a Verilog-A implementation:

$$I_{ph0} - V(X_0) - ddt(\tau_a . V(X_0)) = 0 \qquad (2.75.a)$$

$$V(X_0) - V(X_2) - ddt\left(\frac{\tau_c}{2} . V(X_1)\right) = 0 \qquad (2.75.b)$$

$$V(X_1) - V(X_2) - ddt\left(\frac{\tau_c}{6} . V(X_2)\right) = 0 \qquad (2.75.c)$$

Solving the equations in (2.75.a)-(2.75.c) simultaneously for $V(X2)$, we obtain $I_{ph}(\omega)$. As Figure 2.28 (b) and (c) show, we note the lowest RMS error on the magnitude (1-7%) and less than 1.4% RMS error on the phase for our proposed implementation compared to the other explored approximations. To the best of our knowledge, our proposed implementation is the first demonstration of such accurate SPICE implementation of the photocurrent in UTC-PDs offering the best trade-off between computational effort and model accuracy.

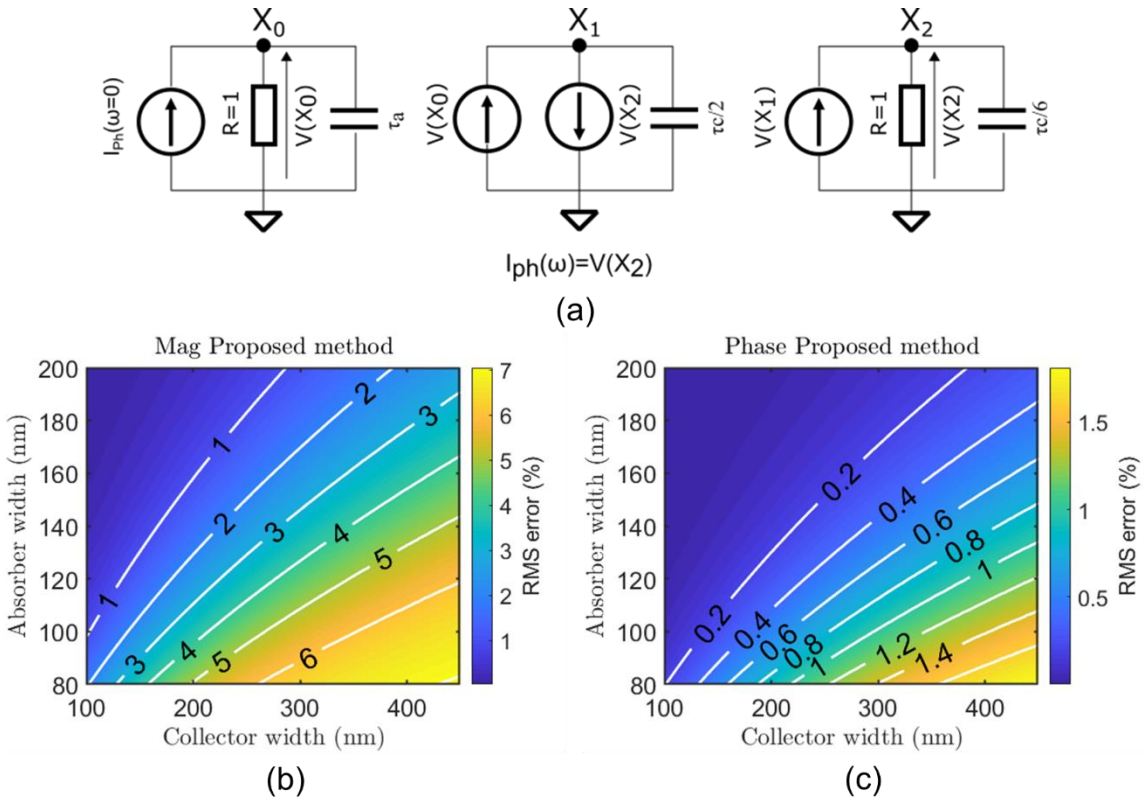

Figure 2.28. (a) Electrical equivalent circuit of the proposed implementation; RMS error compared the analytical solution to our proposed approximation (a) magnitude (b) phase.

2.3.2.1.4.1 Photo-generated carrier velocity

In order to limit the number of parameters to be extracted when optimizing the bandwidth parameters, we use the electric field, $E_{max}(v_d)$, at the collector input to calculate the transit time of the electrons in the collector, τ_C, from their drift velocity, which can be expressed by the following empirical expression [123]:

$$\boldsymbol{v(E) = v_{sat}\left(1 + \frac{\frac{E_{max}(v_d)}{E_{scale}} - 1}{1 + A\left(\frac{E_{max}(v_d)}{E_{scale}}\right)^t}\right)} \quad (2.76)$$

Where v_{sat} is the saturation velocity, $E_{scale} = {}^{v_{sat}}/_{\mu}$, A and t are parameters to be determined from the material used. The parameters of equation (2.76) can be determined from a fit on the data for each material used.

2.4 Conclusion

The UTC-PD technology showcases very promising performances for communication systems in the coming years. With the first structure proposed in 1997, efforts have since continued to propose and explore other structures and materials, in order to improve the performance of the UTC-PDs in terms of their bandwidth and RF output power.

In this chapter, analyses on the notable modelling efforts for developing small signal models of UTC-PDs for RF circuit design have been reported. The limitations of these models have been highlighted and it has been shown that these models are not physics based and therefore cannot be fully exploited for versatility, scalability and for all operating points.

In order to address this topic, it seems thus essential to develop a compact and physics-based model that describes the operation of the UTC-PD under any operating condition: frequency, applied voltage and optical input power.

Based on the first compact UTC-PD modelling efforts initiated at IMS, this PhD works have introduced new physical equations describing, in particular, the dark current, intrinsic series resistance and junction capacitance, and their dependence on the applied bias. As a result, the new model now takes into account more material parameters such as doping, mobility and permittivity. Scaling laws have also been implemented by analyzing the UTC-PD geometries from different technologies studied in this work.

As it will be demonstrated in chapter 4, this model now shows very good agreement with the experimental results for a wide range of operating conditions (DC, RF and optical illumination) across a wide range of geometries from several advanced UTC-PD technologies studied in this work, thus demonstrating its versatility for future optoelectronic circuit design.

Chapter 3: Measurements setup

This chapter is devoted to the description of the eletro-optical measurement setup that has been developed in the context of this work. An overview of the main equipment used will be provided. Possible improvements in the measurement accuracy and corresponding modifications in the setup will also be discussed. Finally, a summary of the characterization and parameters extraction protocols will be presented.

3.1 The electro-optical measurement setup

As the sizes of the integrated UTC-PDs are extremely small, performing measurements on the samples requires working with a probe station. Therefore, one of the probe stations available at the IMS has been set up to perform on-wafer optoelectronic measurements. This probe station

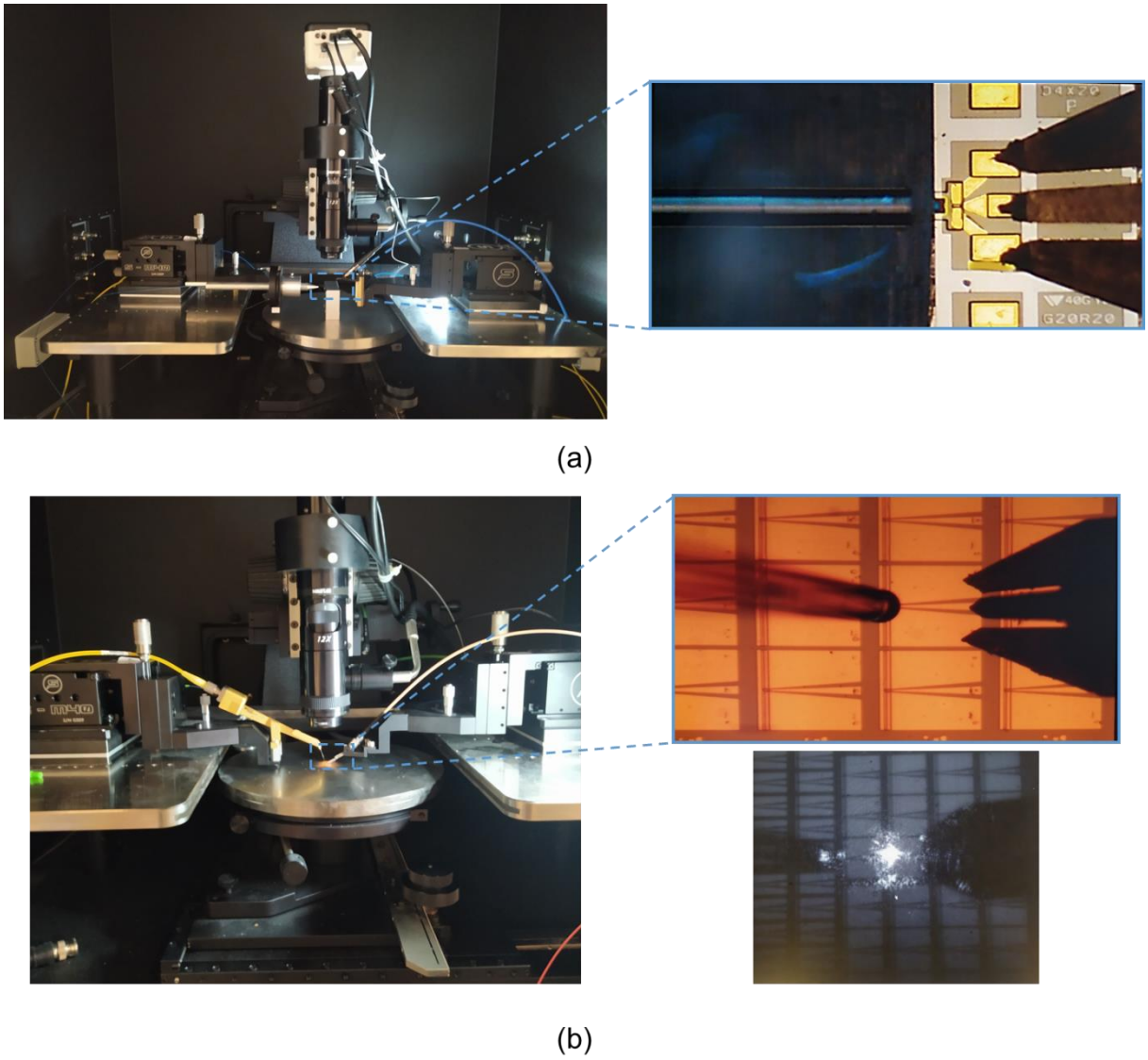

Figure 3.1. A partial view of the probe station (a) Trench light injection configuration with a zoom on the DUT (b) top illumination configuration with a zoom on the DUT, in visible and infrared lights.

is equipped with precision micromanipulators that are used to position and hold the microprobes, a wafer chuck on which the samples are held on firmly by vacuum along with other mechanical adapters that were designed and manufactured at the IMS laboratory to fix optical probes. A microscope with a long working distance was added to the probe station for more flexibility and precision during probe placement. The entire station is elevated on air cushions to ensure mechanical stability during measurements. Figure 3.1 illustrates a part of the station where the optical fiber-probe assembly and RF probe tips are mounted. Figure 3.1 (a) and (b) show the measurement configurations for top illumination and edge illumination, respectively.

In addition to the probe station, DC and RF measurement equipment for both illuminated and non-illumination measurement configurations were used. Figure 3.2 shows a schematic representation of the targeted measurements setup and the main equipment used. Except for the Vector Network Analyzer (VNA) and the source meter (SMU), most of the other equipment was purchased during this PhD work, based on bibliographic research and exchanges within the team to identify the appropriate equipment that better suited our need. In the following sections we will further detail the different measurement equipment used and their respective roles in our characterization.

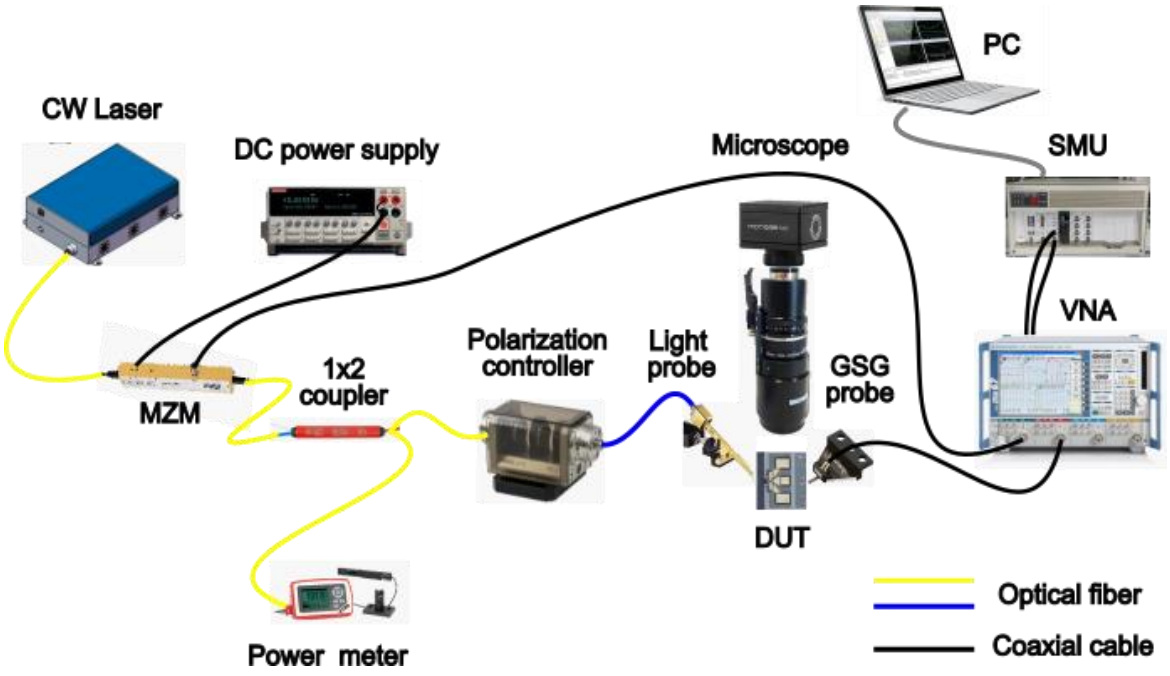

Figure 3.2. Schematic representation of the developed measurement setup.

3.1.1 Electrical equipment

3.1.1.1 Vector Network Analyser

A network analyzer is an instrument that measures network parameters ranging from electronic devices (transistors, diodes, filters, etc.) to more complex circuit modules (amplifiers). Network analyzers most often measure S-parameters because the reflection and transmission in electrical networks are easily measured at high RF frequencies. These S-

parameters can be subsequently converted to Y, Z and H-parameters for impedance analyses and parameter extraction.

In vector network analyzers, RF signals are conventionally represented by $\boldsymbol{a}$ for the incident wave and $\boldsymbol{b}$ for the reflected (or transmitted) wave. The terms $\boldsymbol{a}$ and $\boldsymbol{b}$ are power waves whose absolute squared values (i.e., $|a|^2$ and $|b|^2$) represent the true incident and reflected powers that we apply and measure, respectively. They are defined as follows:

$$\boldsymbol{a} = \frac{\boldsymbol{V} + \boldsymbol{Z_0} \cdot \boldsymbol{I}}{\boldsymbol{2\sqrt{Re(Z_0)}}} = \frac{\boldsymbol{V^+}}{\boldsymbol{\sqrt{Re(Z_0)}}} \tag{3.1}$$

$$\boldsymbol{b} = \frac{\boldsymbol{V} - \boldsymbol{Z_0} \cdot \boldsymbol{I}}{\boldsymbol{2\sqrt{Re(Z_0)}}} = \frac{\boldsymbol{V^-}}{\boldsymbol{\sqrt{Re(Z_0)}}} \tag{3.2}$$

where Z_0 is the characteristic impedance of a transmission line, V^+ and V^- are the incident and reflected voltage wave amplitudes, respectively. We can thus infer that the power waves carry the same information as the voltages for a lossless line (Z_0 is positive and real).

In general, for a network with *n* ports, one can write:

$$\begin{pmatrix} \boldsymbol{b_1} \\ \vdots \\ \boldsymbol{b_n} \end{pmatrix} = \begin{pmatrix} \boldsymbol{S_{11}} & \cdots & \boldsymbol{S_{1n}} \\ \vdots & \ddots & \vdots \\ \boldsymbol{S_{n1}} & \cdots & \boldsymbol{S_{nn}} \end{pmatrix} \cdot \begin{pmatrix} \boldsymbol{a_1} \\ \vdots \\ \boldsymbol{a_n} \end{pmatrix} \tag{3.3}$$

Where a_i and b_i are the incident and reflected waves respectively, for each port i, which is terminated by a characteristic impedance Z_{0i}. For a 2-port network (Figure 3.3), the above equation can be reduced to the following:

$$\boldsymbol{b_1} = \boldsymbol{S_{11}} \cdot \boldsymbol{a_1} + \boldsymbol{S_{12}} \cdot \boldsymbol{a_2} \tag{3.4}$$

$$\boldsymbol{b_2} = \boldsymbol{S_{21}} \cdot \boldsymbol{a_1} + \boldsymbol{S_{22}} \cdot \boldsymbol{a_2} \tag{3.5}$$

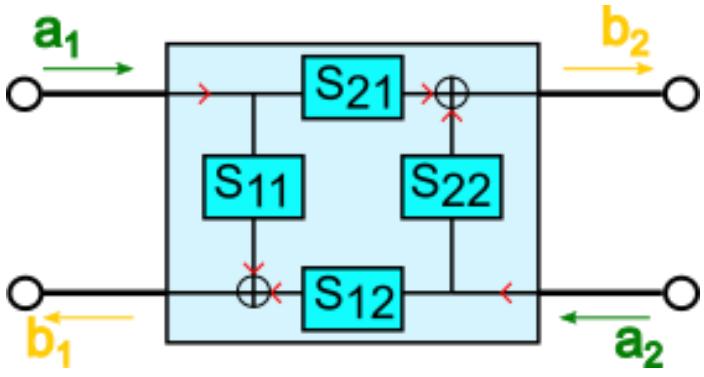

Figure 3.3. Schematic representation of a two port network showing signals and S-parameters.

Hence, the scattering parameters, S_{ij}, are defined as follows:

$$S_{11} = \frac{b_1}{a_1}|_{a_2=0} \quad S_{21} = \frac{b_2}{a_1}|_{a_2=0}$$
$$S_{12} = \frac{b_1}{a_2}|_{a_1=0} \quad S_{22} = \frac{b_2}{a_2}|_{a_1=0} \tag{3.6}$$

In the case of the UTC-PDs, the measurements were performed on one-port setups for the electrical characteristics without illumination and using a two port setup to couple optical input signal into the device for mainly photodiode bandwidth measurements.

For the one-port RF measurements without illumination, the setup comprises a PNA E8361A network analyzer (Agilent), covering the frequency range from 10 MHz to 67 GHz. This analyzer is equipped with a N5260A millimeter head which further extends the measurement frequency range from 67 to 110 GHz (Figure 3.4) [124].

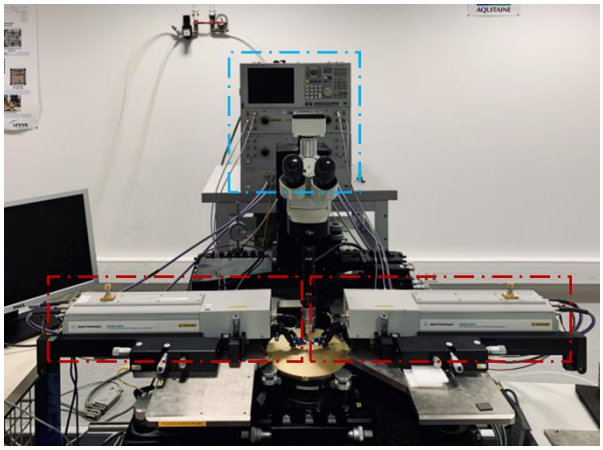

Figure 3.4. The IMS probe station used for 110 GHz on-wafer measurements: highlighted in blue is the PNA E8361A, highlighted in red is the mm-head controllers, i.e. the 67-110 GHz frequency extenders.

For RF measurements under illumination, a Rohde & Schwarz ZVA covering the range from 10 MHz to 67 GHz was used.

3.1.1.2 Radio frequency probes

Currently, radio frequency (RF) probes play a major role in the accurate characterization and, therefore, development of integrated RF technologies, especially for on-wafer measurement and parameter extraction of RF devices and circuits. With RF probes and dedicated test-structures, characterizations can be performed directly on the fabricated wafer containing individual components as well as final circuits and even systems [125]. This has helped reduce the research time and costs associated with the development and testing of new technologies.

In general, RF probes consist of a body with a transition to an RF connector on one side allowing connection to the measuring instrument via a coaxial cable or waveguide. The other side of the body is connected to a micro coaxial cable that finally leads up to a planar waveguide (e.g. CPW), which forms the tip head (Figure 3.5). The CPW is tilted to ensure planar contacts simultaneously. The probe tips can be made of different materials such as tungsten, copper-beryllium or gold-nickel alloys. Some WG-based probes also incorporate a bias tee, which is used in active device measurements to provide DC bias to the device.

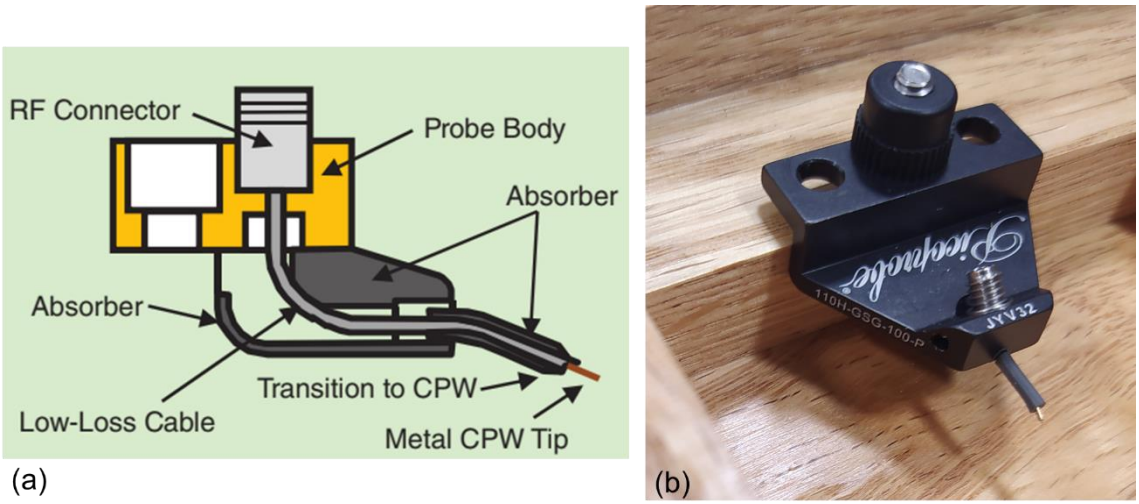

Figure 3.5. (a) A schematic of an RF probe based on a microcoaxial cable [125] (b) image of the Picoprobe® probes used in our study.

In the frequency range, in which we performed the on-wafer RF measurements (0.5-110 GHz), two different probes from the same manufacture were used. Indeed, the use of two different probes is due to the fact that two of the three studied UTC-PD technologies have pads with two different pitches of 100 µm and 150 µm. These probes are from GGB Industries Inc. Picoprobes®. Figure 3.5 shows an image of these probes; Table 3.1 summarizes the main technical features of these probes.

Table 3.1. Main feature of the used Picoprobe® probes.

Features	**Picoprobe GSG**
Frequency range (GHz)	DC to 110
Pitch (µm)	100 and 150
Probe input	Coax 1.0 mm
Tip material	BeCu
Insertion loss (typ.) (dB)	1.5
Return loss (typ.) (dB)	15

3.1.1.3 Dedicated substrate for off-wafer calibration

It is important to note that all contributions of the measurement setup from the VNA ports to the Device Under Test (DUT), such as cables, connectors, adapters and extenders, are to be considered as extensions of the VNA ports. The systematic errors associated with all these contributions can be eliminated, along with those produced internally by the VNA, through a calibration process. A typical calibration process for the S-parameter measurement setup consists of determining the systematic errors through a series of measurements on dedicated calibration structures (Figure 3.6), called standards. The errors thus determined are then subtracted, or 'de-embedded', from the raw S-parameter measurement data from a DUT. For on-wafer measurements, the calibration steps can be performed on an Impedance Standards Substrate (ISS) on alumina (a material of high dielectric quality) and the correction of errors can be made by several methods. In our work, the commercial calibration substrate CS-5 from GGB Industries was used, which is suitable for measurements in the 110 GHz range and the SOLT (for Short Open Load Thru) and the LRRM (Load Reflect Match) error correction methods were used [126].

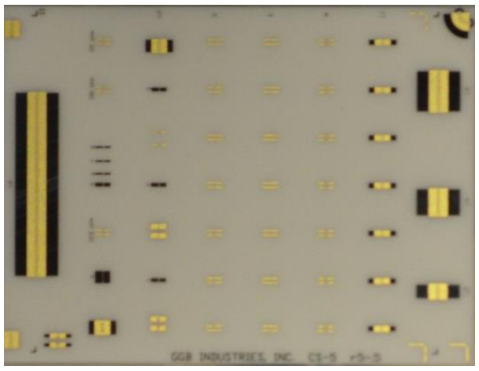

Figure 3.6. CS-5 calibration substrate.

3.1.2 Optical equipment

As already mentioned, the starting point in the installation of the new electro-optical measurement setup was a probe station dedicated to electrical characterizations. Next, we had to acquire additional, especially optical equipment, in order to perform optoelectronic measurements.

3.1.2.1 CW laser

During this thesis work, two laser sources were used. A first laser was used for the static photocurrent characterizations and a second laser, integrated in an optical module, was used for the measurements of bandwidths of the UTC-PDs, which will be described in more details later in this chapter. The first laser is a single frequency continuous wave laser with a wavelength of 1551 nm, providing a linewidth of less than 2 MHz and a high output power that can be amplified up to 127 mW by an amplifier optimized for low noise operation.

3.1.2.2 Polarization controller

As in fiber optic communication networks, lasers used for characterization in the laboratory setups emit mainly TE polarized light. However, commonly used fibers do not maintain the polarization state of the light constant during propagation. Consequently, the polarization state of the light arriving at the photodiodes remains unknown.

Controlling the light polarization was considered a viable option when defining the first configuration of the measurement setup. Initial requirements were set such that it would be possible to control any polarization state, compactness, mechanical stability and minimal optical coupling losses. For this purpose, we decided to use polarization controllers from Thorlabs® designed for fiber optic setups (Figure 3.7) [127]. Indeed, these polarization controllers are capable of transforming an arbitrary input polarization state into a pre-defined output polarization state. These controllers use two fiber ports mounted on either side of a single-axis fiber bench with wall plates. Any input polarization state can be deterministically transformed into a known output polarization state using a quarter-wave, a half-wave, and a quarter-wave plate mounted (in this order) between the two fiber ports. Each plate can be rotated 360° both precisely and continuously.

Figure 3.7. Photograph of the polarization controller.

Other advantageous features of the polarization controller are the wavelength operating range of 1100 to 1620 nm. It supports both types of fiber connectors, FC/PC and FC/APC, which are most commonly used in laboratory optical experiments. The controller also has good mechanical and thermal stability.

3.1.2.3 Optical fibers and light wave probe

3.1.2.3.1 Single mode optical fiber and coupler

Single mode optical fibers were used to connect the laser to other optical components (laser, polarization controller and optical power meter). These optical fibers are FC/APC terminated at both ends, making them ideal for systems sensitive to back reflections (Figure 3.8 (a)). The fiber tips are polished to be tapered at an 8° angle, providing a typical return loss of 60 dB. A one-input, two-output (1×2) coupler optical fiber with a 50:50 coupling ratio (Figure 3.8 (b)) was also used to link the optical components. The input of the coupler is connected to

the laser source and the two outputs are connected to the polarization controller and a power meter to read the power delivered by the laser.

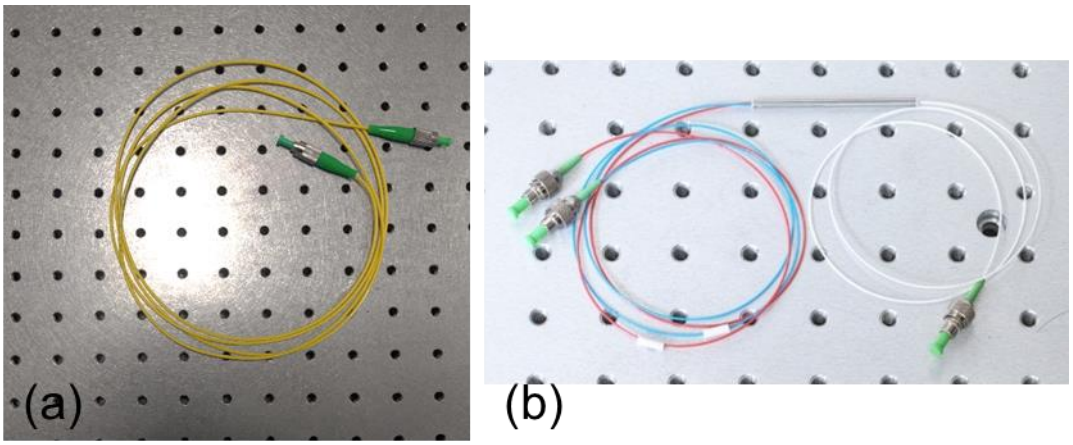

Figure 3.8. Optical fibers used for optical equipment's interconnections: (a) single mode (b) 50:50 optical fiber coupler.

3.1.2.3.2 Polarization maintaining (PM) lensed fiber

A polarization-maintaining (PM) lensed optical fiber from IDIL® was used [128] in our setup. It helps both to maintain the polarization imposed by the polarizer output and to minimize the size of the laser spot during the illumination of the photodiodes. Figure 3.9 shows the core of the fiber on which a micro-lens is fixed. To use the fiber, it must be placed on a micro positioner that can move in all 3 directions. The micro positioner, which has been used in this study, has a resolution of 2 µm in each direction. The lensed fiber has been used for characterization of integrated waveguide UTC-PDs operating under edge illumination.

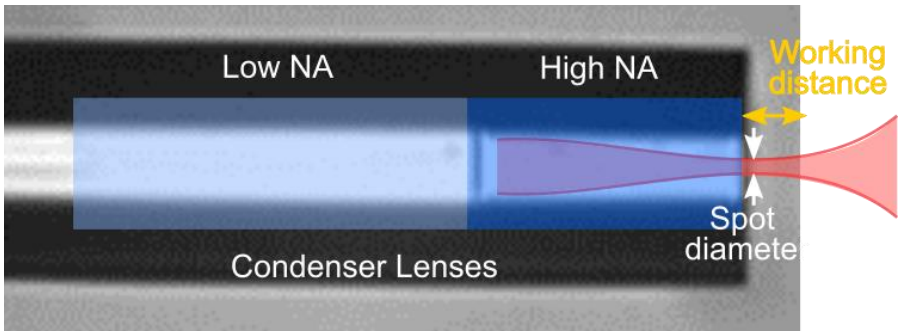

Figure 3.9. IDIL PM Lensed fiber.

The main technical specifications/characteristics of the lensed fibers provided by the vendor are summarized in the Table 3.2.

Table 3.2. Main feature of the used PM lensed fiber.

Features	IDIL PM lensed fiber
Wavelength (µm)	1550 nm
Mode field diameter (µm)	< 5.0
Working distance (µm)	Slightly divergent up to 100
Power handling (W)	1.0
Polarization Dependent Loss (dB)	< 0.01 dB
Fiber connector	FC/APC

3.1.2.3.3 Light wave probe

In order to build a versatile measurement setup with respect to the illumination strategy of the UTC-PDs, a Light Wave Probe (LWP) was acquired (Figure 3.10). In fact, the LWP can be used for on-wafer optical measurements of various photonics devices. In the LWP, fibers are replaceable by the user, allowing the probe to be optimized for a variety of light injection and light collection applications, including characterization of top-illuminated photodiodes, vertical cavity lasers (VCSELs), hybrid emitters and receivers, and LEDs [129]. The LWP offers an illumination angle that varies from 2° to 18°, which essentially allows the user to optimize the illumination angle for either mesa-structured photodiodes with top illumination or integrated waveguide photodiodes, for which the light is fed through a grating coupler. Since the optical fiber has to be selected according to application requirements, we opted for a single-mode optical fiber that can provide an illumination diameter as small as 5 µm.

Figure 3.10. Light wave probe.

3.1.2.4 Electro optic modulator

There are several methods for measuring the bandwidth of photodiodes. One of the most common methods, based on RF over fiber techniques, is to directly inject RF modulated light into a photodiode and then measure the output RF signal. In our work, we used another widely

used method that uses an external modulator via an electro-optical (EO) modulator. This method is relatively simple to implement and allows one to generate a coherent signal. In addition, the EO modulators require a low control bias and allows measurements over a wide bandwidth with a low signal distortion [130]. The EO modulator is usually made of indium phosphide (InP), lithium niobate (LiNbO3) or gallium arsenide (GaAs) materials.

To perform our bandwidth measurements, we acquired an intensity EO modulator from iXblue. This modulator is a LiNbO3 waveguide intensity modulator with Mach-Zehnder interferometers (Figure 3.11 (a)). The intensity MZMs generally consist of a two-arm interferometer integrated on a LiNbO3 substrate. The two arms are connected by couplers on both sides (Figure 3.11 (b)). The first coupler is used to split the incoming light in a balanced way (for the ideal modulator) into the two arms. The second coupler merges the two separated laser beams, resulting in an interference.

Indeed, the interference can be created and controlled by the phase change in both arms via the modulation of the optical index. The phase change is no more than a stretching or a contraction of the optical path which induces an intensity modulation at the output of the device (Figure 3.11 (b)). This modulation of the optical index can be induced by the application of an electric field in the electro-optical material (LiNbO3). This electric field is in fact the superposition of the supply voltage, V_{bias}, and the modulation voltage, $V_{mod}(t)$, which can be applied between the electrodes of the modulator. MZM modulators generally have two pairs of electrodes: the modulation electrodes (often called RF electrodes) and the DC electrodes (also called polarization electrodes).

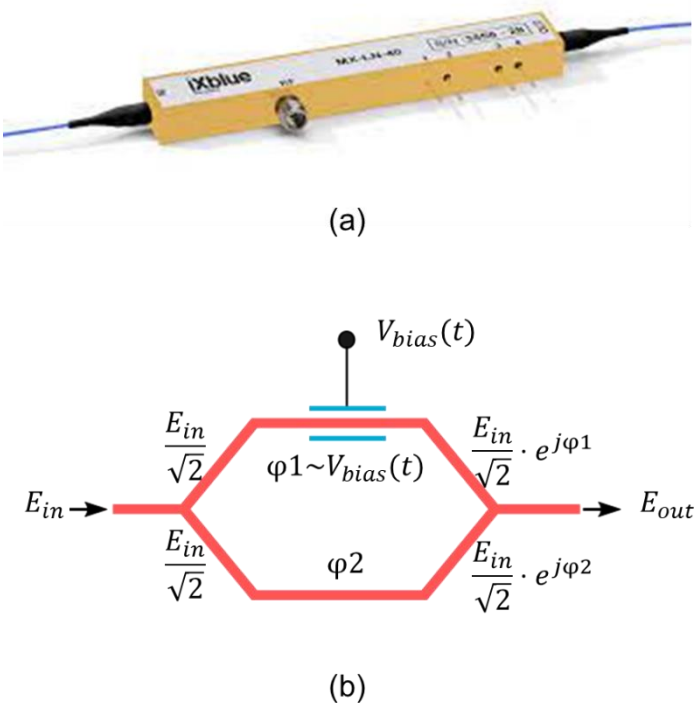

Figure 3.11. (a) iXblue intensity MZM (b) Simplified configuration of MZM.

For an ideal intensity MZM, the transfer function of the output power driven by time dependent voltage $V(t) = V_{bias} + V_{mod}(t)$ is given by the following expression:

$$\boldsymbol{P_{out} = |E_{out}|^2 = \frac{1}{2} \cdot |E_{in}|^2 \cdot (1 + cos(\varphi 2 - \varphi 1))} \quad (3.7)$$

As the phase, φ, on the first arm is proportional to the applied voltage, the expression (3.7) becomes:

$$\boldsymbol{P_{out} = \frac{1}{2} \cdot P_{in} \cdot \left(1 + cos\left(\pi \cdot \frac{V_{bias} + V_{mod}(t)}{V_{\pi}}\right)\right)} \quad (3.8)$$

Where P_{in} is the input optical power, V_{π} is the voltage needed to induce a π phase shift on the optical signal, also called the half-wave voltage. For a non-ideal MZM, a phase term,∅, can be added in case of asymmetric arms, resulting in unbalanced optical paths. Also, the insertion loss can be taken into account through a term, α.

The operating bias of the modulator is the bias on the transfer curve (Figure 3.12) around which the modulation signal is applied. It must be chosen according to the intended application. In our case, we worked with quadrature polarization to avoid any distortion of the output RF signal.

It is worth noting that the modulator transfer function drifts with time. The reasons for this behavior can be explained by a complex combination of pyroelectric, photorefractive and photoconductive phenomena activated in the electro-optical materials of the MZM [130]. In fact, this drift leads to a modification of the modulated optical signal if the bias voltage is not adjusted back to the desired state. Figure 3.12 shows a drift of the modulated optical signal which is seriously affected both in amplitude and frequency if the bias voltage is not corrected. For long term operation and especially in all systems that have to operate under changing temperature conditions, an automatic bias control system is needed to always ensure the correct DC voltage and lock the selected operating point.

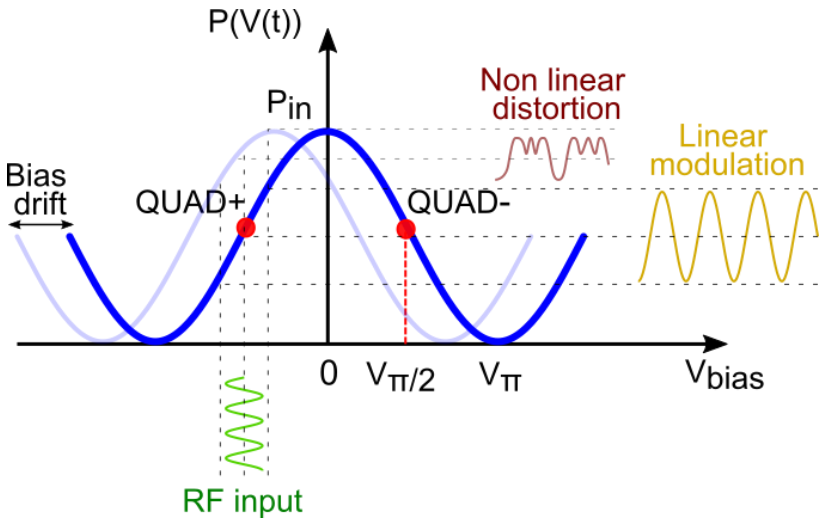

Figure 3.12. Typical transfer function of an MZM.

iXBlue offers a solution called ModBox-VNA with two versions suitable for operation in the 40 GHz and 70 GHz ranges. In this solution, there is MZM modulator, a modulator bias controller and an optional DFB laser operating at 1550 nm that can deliver a maximum power of 4 dBm. In the ModBox-VNA, all of these required hardware is assembled and encased in an enclosure integrated with a touchscreen control interface (Figure 3.13). For the UTC-PD bandwidth measurements that will be presented later, we used the 70 GHz version of the ModBox-VNA.

Figure 3.13. iXBlue ModBox-VNA.

3.1.2.5 Visualization system

To clearly visualize the DUT to be measured while maintaining a good working distance, a visualization system adapted to this type of measurements was set up. It is essentially composed of a Moticam 580 camera and a set of lenses proposed by Thorlabs. These zoom lenses are comprised of three modules (Figure 3.14). The first module consists of a modular extension tube which can provide a 7-fold magnification. It offers a fine focus travel of 3 mm for a wide range of working distances (up to 37 mm), as well as a coaxial illumination port, compatible with fiber bundles. The second module consists of a 2× magnification lens. Finally, the third module consists of an additional extension tube with 2× magnification that can be attached to a camera mounted using an adapter. Together, these components offer a net magnification of 0.07 to 28-fold.

Figure 3.14. The different components of the adopted visualization system.

3.2 Potential improvement of the measurement setup

In its current state of operation, the measurement setup can still be further improved. There are mainly two aspects to improve.

The first is to substitute the micro-positioner, where the fiber lens is placed, with a more precise version. Note that the micro positioner used has a resolution of 2 µm in each direction. This limited us from illuminating the photodiodes efficiently. These micro positioner can be replaced by commercially available micro positioners that can move in all 3 directions with a resolution of roughly less than one micrometer. Moreover, each axis can be moved precisely with a resolution of a few tens of nanometers owing to a piezoelectric system in these micro-positioners.

The second aspect to improve is to adapt the setup to the cut-off frequency of the photodiodes. As the frequency responses of photonic technologies push more and more towards higher frequencies, updating the limits of measurement systems must be ensured. In this work, we have made bandwidth measurements up to 67 GHz with the ModBox-VNA module [131]. The optical heterodyne technique is a more suitable method for these types of measurements involving a higher bandwidth of photodiodes. The main advantage of this method is that the modulation frequency can reach several THz [132]. The principle of optical heterodyne mixing is shown in Figure 3.15.

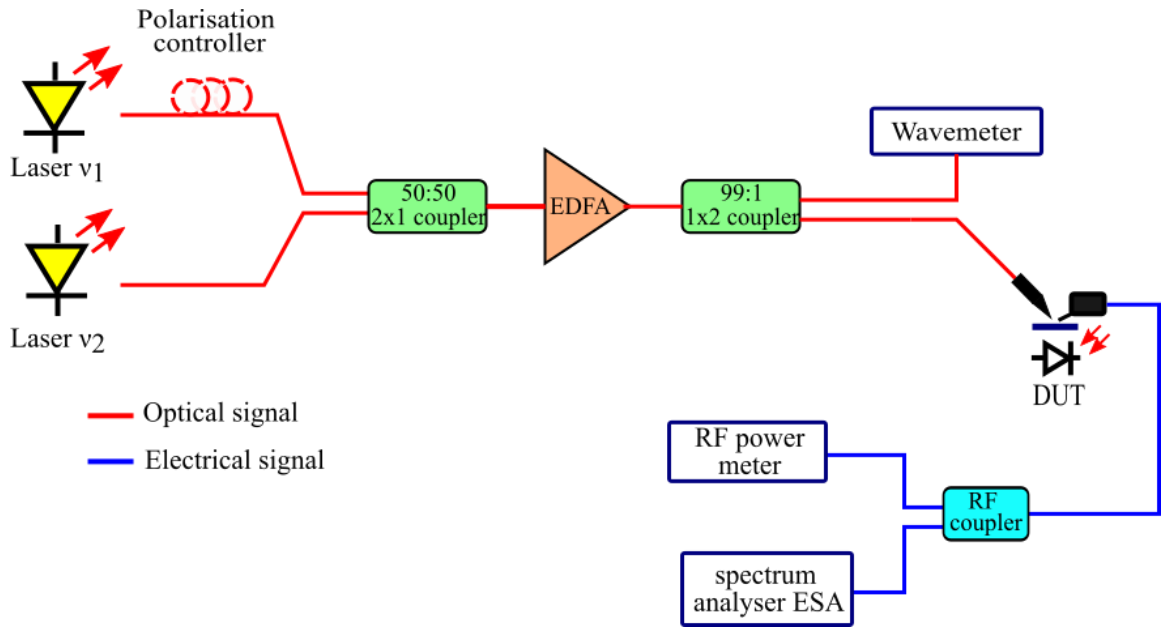

Figure 3.15. Optical heterodyne principle.

In this method, beating of two narrow linewidth, single frequency lasers, ν_1 and ν_2, are coupled in a 2x1 optical fiber coupler. To obtain the maximum beating power, a polarization controller (PC) placed at the output of one of the two lasers is used to ensure that the two laser waves are in the same polarization state, thus ensuring maximum beating power. At the output of the coupler, which ensures the spatial superposition of the two waves, the envelope frequency of the resulting modulated optical wave (and therefore the RF beating frequency) is equal to the difference of the frequencies of the two optical lasers ($\nu_{RF} = |\nu_1 - \nu_2|$). The optical beating signal is then photo-detected by the DUT and analyzed by an electrical spectrum analyzer or power meter.

3.3 Measurement protocol

The procedure used to perform the measurements, the de-embedding and the extraction of the model parameters is illustrated in Figure 3.16. More detail about each step is discussed in the subsequent sections.

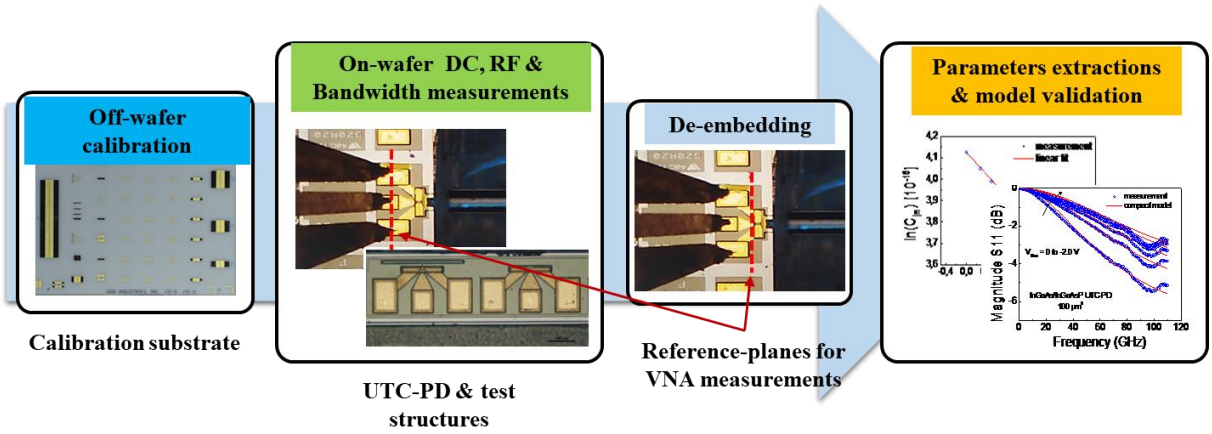

Figure 3.16. Flowchart explaining the characterization procedure and the model validation.

In our workflow, we first perform an off-wafer calibration on a standard impedance substrate. This involves calibration of the whole measurement setup, including the VNA, RF cables, and RF probes in a single step. This calibration eliminates errors in the measured S-parameters that originate from the VNA and the RF connectors due to losses and reflections. As already mentioned before, this calibration is performed on a commercial calibration substrate provided by the GSG probe vendor.

After performing the necessary calibrations, on-wafer measurements can now be performed on UTC-PDs and test structures. It should be noted that the role of the test structures is to reproduce the pads and access lines connected to the active region of the UTC-PDs. The measurements performed include DC and RF measurements with and without illumination.

Once we have the measurements data on the UTC-PDs and the test structures, a de-embedding operation can be performed. This operation removes the contribution of the pads and access lines from the raw measurement data, and thus moves the reference plane of the

measurements at the edge of the intrinsic devices, which can finally be used to access and analyze the intrinsic device.

In the end, using various de-embedded measurements and depending on how the compact model has been formulated, a step-by-step extraction and model validation process (which will be detailed in the next chapter) can be performed.

3.4 Conclusion

During this work, we initiated the electro-optical characterization of an optoelectronic component for first time at IMS laboratory, we started by developing a measurement bench to perform on-wafer optoelectronic characterizations.

We used a probe station dedicated to electrical characterizations and adapted as well as equipped it to be able to perform these optoelectronic measurements.

For this, we equipped the station with a visualization system with a larger working distance to be able to probe the components easily. Furthermore, we have also equipped the station with an optical module mainly consisting of a laser, a polarization controller, an optical probe, lensed optical fibers and an MZM modulator.

Moreover, improvements of the measurement setup have also been envisioned, with regard to the bandwidth measurement, in particular, conforming to the increase in UTC-PD bandwidth.

Finally, an overview on the workflow, starting from measurements up to the extraction of model parameters, was presented. We will discuss further details of each step of the workflow in the next chapter.

Chapter 4: Results

The validation of a device compact model implies a good agreement between the predicted simulation of the already calibrated model and the actual performances of the device. This chapter provides comprehensive results obtained with regards to the validation of our developed UTC-PD compact model. In order to ensure accurate extraction of intrinsic device parameters, the first step is to investigate the conventional de-embedding techniques, dedicated to one-port devices, from the literature. Then, we discuss the implementation of these techniques in our case study. We also compare the efficiency of these techniques with the techniques that we have developed that are better adapted to our case study. Once the de-embedding was performed correctly, the results are then used to extract the compact model parameters. Finally, the chapter concludes with the presentation of extensive model validation particularly for the main figures of merit, the dark current and the bandwidth, of the studied UTC-PDs.

4.1 De-embedding

4.1.1 Brief review of conventional one-port de-embedding methods

During RF characterization and followed by an off-wafer calibration, the reference plane of the measurement moves to the level of the RF pads. To access the intrinsic parameters of the device, the second step consists in performing on-wafer measurements on dedicated test structures, followed by a matrix subtraction step called de-embedding. This operation also helps to identify the equivalent electrical network for the pads and the access lines. Thus, following the de-embedding step i.e. the subtraction of external parasitic network, we have moved the reference plane of the measurement to the edge of the UTC-PD active region (Figure 4.1).

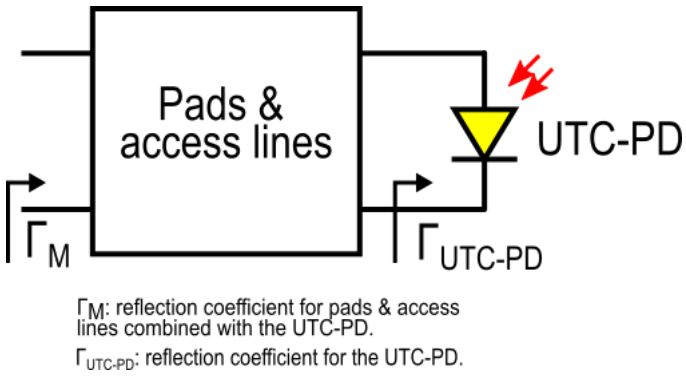

Figure 4.1. Extrinsic equivalent circuit representation for the UTC-PD compact model.

Compared to two-port devices, extensive studies on the de-embedding of one-port active devices, such as UTC- PDs, are quite scarce and lack in-depth investigations. Moreover, some of the conventional methods reported in the literature are compatible with all types of test structures and are not valid over a very wide frequency range. We will first review the most widely used de-embedding techniques cited in the literature.

4.1.1.1 Open-Short and Short-Open de-embedding

In this section, we focus on the most standard de-embedding methods. We can identify two de-embedding methods which are based on Open and Short test structures [133]. Note that the Open and Short structures are structures identical (dimensions and materials) to the pads and access lines connected to the DUT. These structures are used to determine the series and parallel impedances associated with the presence of pads and access lines.

The Open-Short de-embedding method consists in removing the capacitive, resistive, and inductive elements electrically equivalent to the pads and access lines connected to the UTC-PD (Figure 4.2 (a) and (b)). The extraction of the intrinsic impedance of the DUT, $\boldsymbol{Z_{UTC-PD_{OS}}}$, can be summarized by the expression:

$$\boldsymbol{Z_{UTC-PD_{OS}} = (Y_M - Y_{OC})^{-1} - (Y_{SC} - Y_{OC})^{-1}} \quad (\mathbf{4.1})$$

Here, Y_M is the total measured admittance, Y_{OC} and Y_{SC} are the admittances of the open and short structures, respectively. The Open test structure is represented by a capacitance, C_p, that can be extracted from the imaginary part of the reflection coefficient, Γ_{OC}, and converted into admittance Y_{OC}. The Short test structure is represented by a resistance, R_p, in series with an inductance, L_p. These values can be extracted from the real and imaginary part of Γ_{SC}, respectively, and then converted to Z_{SC}.

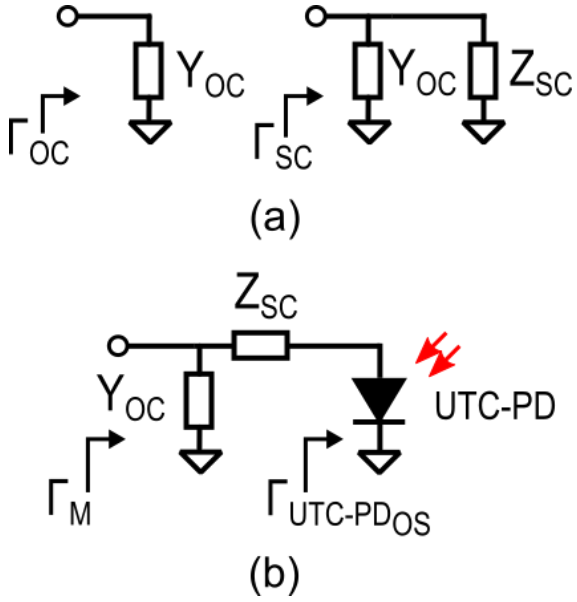

Figure 4.2. (a) Open-Short parasitic model (b) extrinsic equivalent circuit representation for the UTC-PD compact model.

The Short-Open de-embedding method is similar to the Open-Short method, except that the inductive and resistive parts are removed prior to the removal of the capacitive component (Figure 4.3 (a) and (b)). Thus, only the order of the elements change in the electrical equivalent circuit. The whole procedure can be expressed as follows:

$$\boldsymbol{Y_{UTC-PD_{SO}} = (Z_M - Z_{SC})^{-1} - (Z_{OC} - Z_{SC})^{-1}} \quad (\mathbf{4.2})$$

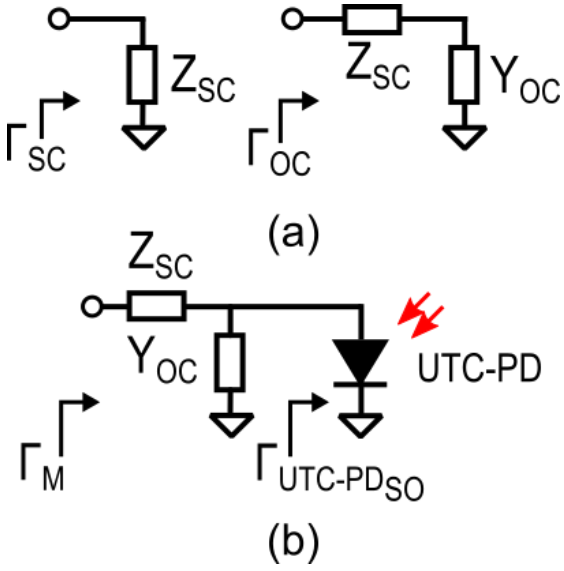

Figure 4.3. (a) Short-Open parasitic model (b) extrinsic equivalent circuit representation for the UTC-PD compact model.

4.1.1.2 S-parameter based de-embedding

Another method, known as S-parameter based de-embedding method [134], relies on determining the four S-parameter matrix for the pads and the access lines (Figure 4.4) associated with a waveguide. This method requires both an Open and a Short test structure. For this method, the property of passivity of the access lines is taken into account in order to reduce the matrix elements ($S_{12} = S_{21}$). Also, an assumption on the symmetry of the access lines is taken into account ($S_{11} = S_{22}$). Hence, the four matrix elements can be reduced to two. Equation (4.3) gives the total measured reflection coefficient of the UTC-PD from the theory of S-parameters [134]:

$$\boldsymbol{\Gamma_M = S_{11} + \frac{S_{12}S_{21}\Gamma_{UTC-PD_{Sp}}}{1 - S_{22}\Gamma_{UTC-PD_{Sp}}}} \qquad (\mathbf{4.3})$$

Thereby, the intrinsic reflection coefficient of the UTC-PD can be written as:

$$\boldsymbol{\Gamma_{UTC-PD_{Sp}} = \frac{S_{11} - \Gamma_M}{S_{11}S_{22} - S_{22}\Gamma_M - S_{12}S_{21}}} \qquad (\mathbf{4.4})$$

For the Open test structure, the reflection coefficient of these test structures, Γ_{OC}, can be replaced in (4.3) by $\Gamma_{OC} = 1$:

$$\boldsymbol{\Gamma_{OC} = S_{11} + \frac{S_{12}S_{21}}{1 - S_{22}}} \qquad (\mathbf{4.5})$$

For the Short test structure, the reflection coefficient of these test structures, Γ_{SC}, can be replaced in (4.3) by $\Gamma_{SC} = -1$:

$$\Gamma_{SC} = S_{11} - \frac{S_{12}S_{21}}{1 + S_{22}} \quad (4.6)$$

Based on the passive and symmetric waveguide approximations discussed above, the intrinsic reflection coefficient of the UTC-PD can thus be simplified as follows:

$$\Gamma_{UTC-PD_{Sp}} = \frac{\Gamma_{OC} + \Gamma_{SC} - 2\Gamma_M - \Gamma_M(\Gamma_{OC} - \Gamma_{SC})}{2\Gamma_{OC}\Gamma_{SC} + \Gamma_{SC} - \Gamma_{OC} - \Gamma_M(\Gamma_{OC} + \Gamma_{SC})} \quad (4.7)$$

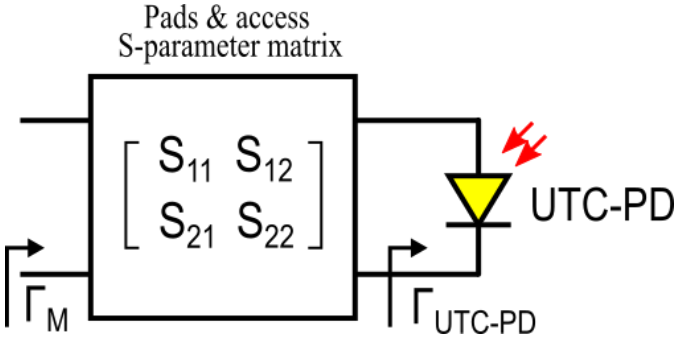

Figure 4.4. Schematic illustration of the S-parameter based de-embedding method.

4.1.2 UTC-PD high frequency characterization and de-embedding results

To assessing the model's scalability and versatility, both type I and II [135] UTC-PDs were characterized. More specifically, two varieties of type I UTC-PDs have been studied: (i) an InGaAs/InGaAsP UTC-PD with rectangular waveguide, through which the light is guided evanescently into the active region [136]; (ii) an InGaAs/InP UTC-PD with a simple top-illuminated structure. The type II device consists of a GaInAsSb/InP UTC-PD also with a simple top-illuminated structure [120]. Several geometries of the UTC-PDs were investigated in the current study, with their active areas listed in Table 4.1. Dedicated test structures associated with the UTC-PDs were available for the extraction of their intrinsic parameters.

Table 4.1. Geometries of the UTC-PDs under study.

UTC-PD technology		**Drawn active area (μm^2)**
UTC-PD type I	InGaAs/InGaAsP	100, 125 and 150
	InGaAs/InP	13
UTC-PD type II	GaInAsSb/InP	64, 79 and 100

For compact modelling validation, de-embedding is a crucial step since at high frequencies (required for communication using high data rates), the impact of parasitic interconnections becomes even more significant. Hence, accessing the intrinsic physical parameters of the UTC-PD requires careful modelling of the RF pads and access lines. To this purpose, dedicated test structures reproducing the pads and access lines are used, such as Open, Short and Thru test structures.

In the next section, we will implement the de-embedding techniques reported in the literature. We will highlight their limitations and suggest alternatives adapted to our case study.

4.1.2.1 GaInAsSb/InP UTC-PD de-embedding

In order to apply de-embedding method on the GaInAsSb/InP UTC-PDs, one-port S-parameter measurements were performed at ETH Zurich, up to 67 GHz, on Open and Short test structures (see Figure 4.5) as well as on the three geometries of the UTC-PD under a bias ranging from 0 to -2.5 V. The S-parameter measurements were preceded by an off-wafer LRRM (line/reflection/match) calibration [137] in order to move the measurement reference plane up to the RF probe tips.

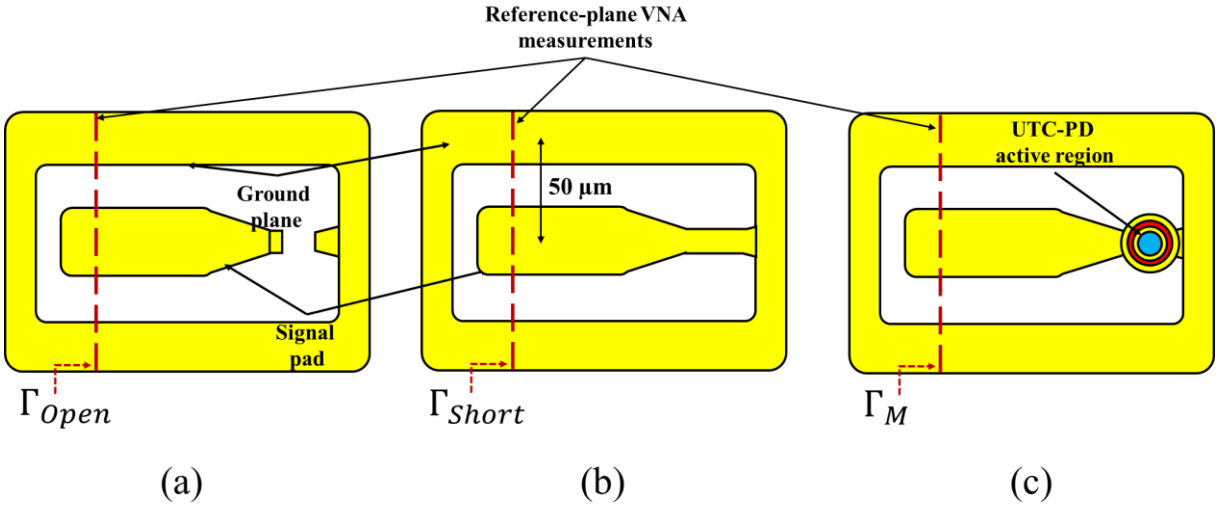

Figure 4.5. Schematic of the (a) Open (b) Short test structures (c) UTC-PD connected to pads and access lines.

Figure 4.6 (a) and (b) show the Smith plots of the reflection coefficient for the Open and the Short test structures as well as for the UTC-PD. The representation on the Smith chart allows us to understand the characteristics of the DUT impedance for various frequency and bias voltages. These reflection coefficients are composed of real and imaginary parts that represent respectively the resistive and capacitive or inductive contributions.

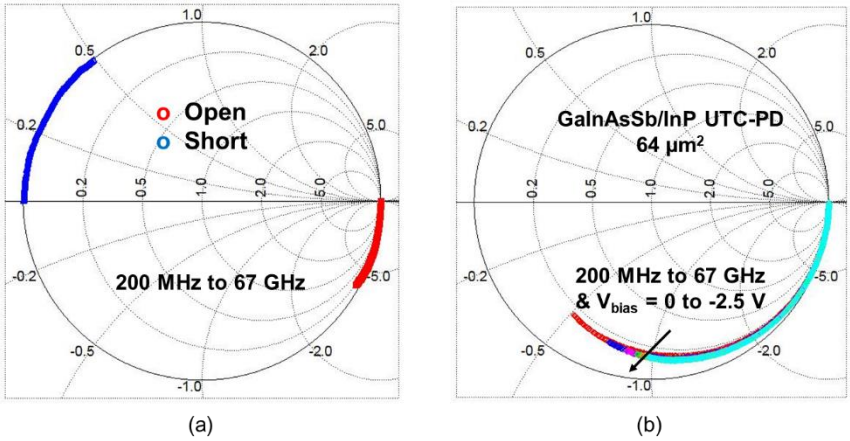

Figure 4.6. Smith chart representation of the measured electrical reflection coefficients of: (a) the Open and the Short test structures (b) the GaInAsSb/InP UTC-PD with an active area of 64 µm2 for several biases (0,-2.5)V.

Initially, we applied the conventional de-embedding methods discussed earlier: Open-Short, Short-Open and S-parameter based. The use of these techniques seemed justified since the electrical elements equivalent to the test structures did not show significant frequency dependence as observed in Figure 4.7.

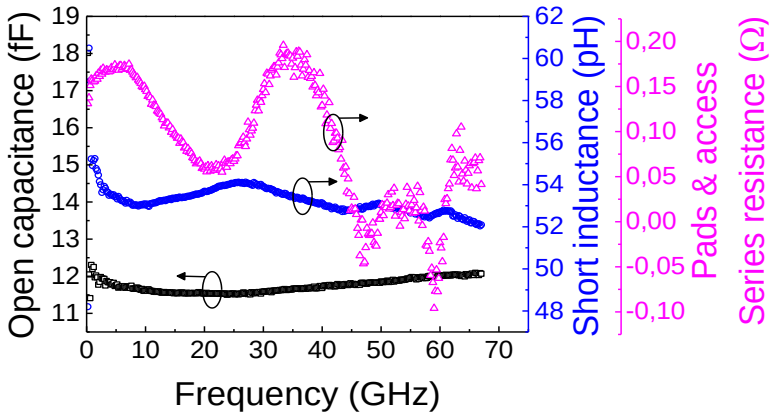

Figure 4.7. Extraction of parasitic capacitance, inductance and resistance equivalents to the Open and Short test structures.

Figure 4.8 shows the extracted junction capacitance values of a GaInAsSb/InP UTC-PD with an active area of 64 µm^2 (square shape) at zero bias. These junction capacitance values were extracted from the imaginary part of the Z11-parameter (previously named $\Gamma_{UTC\text{-}PD}$) obtained after de-embedding as follow:

$$C_{jT}(V_d = 0) = -\frac{1}{Im(Z_{11}(V_d = 0)) \cdot \omega} \tag{4.8}$$

The results in Figure 4.8 show very similar values of the junction capacitance, extracted using all three de-embedding methods, for frequencies up to 10 GHz. Above that, the extracted values diverge as the frequency increases, indicating uncertainties of the de-embedding methods. Thus, the previously discussed conventional de-embedding methods can only be used to extract the junction capacitance in limited frequency ranges. Hence, they do not provide reliable results for the validation of the compact model nor for any other small signal models over the entire frequency range.

Based on the limitations of the conventional methods, modelling the pads and the access lines using only a single RLC network (Open-Short, Short-Open and S-parameter case) is inadequate to capture the actual frequency dependence of the UTC-PDs. To overcome their limitations, other methods have been proposed relying on the same test structures. The main idea behind these methods is to dissociate the electrical networks equivalent to the pads and the access lines into an interconnection of subnetworks as shown in Figure 4.9.

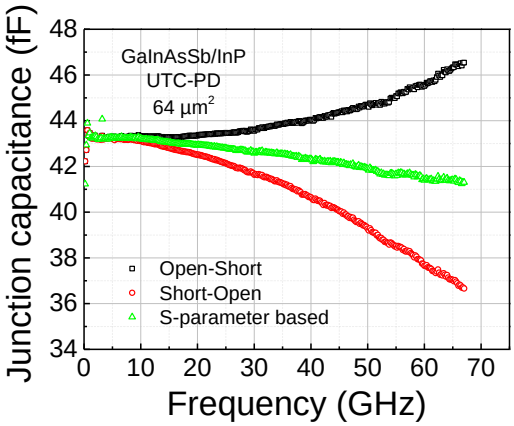

Figure 4.8. GaInAsSb/InP UTC-PD junction capacitance extraction.

To obtain a rather frequency-independent behaior of the intrinsic UTC-PD junction capacitance, we chose a balanced distribution of the sub-networks constituting the final

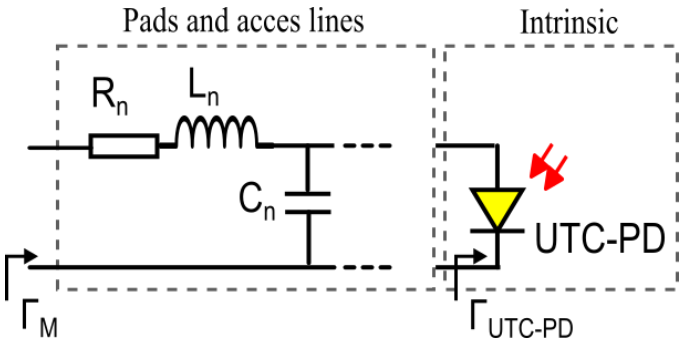

Figure 4.9. Equivalent circuit of the UTC-PD connected in cascade with the subnetwork for the pad and access lines.

electrical circuit representing the pads and the access lines. Hence, the pads and the access lines have been generically modeled by a cascaded $R_nL_nC_n$ network consisting of N sections. In our present study, three sets of cascaded $R_nL_nC_n$ elements were identified from the experimental results. This was achieved by ensuring that the resulting intrinsic junction capacitance of the UTC-PDs did not exhibit a frequency dependence. The R value was extracted from the real part of Z_{Short} while the L and C values were determined by optimizing the equivalent circuit model on the imaginary part of the measured Y_{Open}, as shown in the Figure 4.10, leading to the three cascaded $R_nL_nC_n$ elements. As presented in Figure 4.10, the sum of the capacitances, $\sum_{i=1}^{N} C/N$, converged to Y_{Open}/ω at low frequencies and the sum of the inductances, $\sum_{i=1}^{N} L/N$, was determined through an optimization at high frequency. The extracted parameter values are listed in Table 4.2.

Once the equivalent network of the extrinsic passive elements is accurately modeled, two-port S-parameter simulation data of the cascaded network can be used for de-embedding and obtain the intrinsic parameters of the UTC-PD through equation (4.7). Figure 4.11 shows the UTC-PD junction capacitance extracted from S-parameters de-embedded using the cascaded network. The results clearly reflect a significant improvement following the corrections for over de-embedding, as discussed earlier.

Table 4.2. Extracted R, L and C lumped elements from GaInAsSb/InP UTC-PD Open and Short Thru test structures.

R	**L**	**C**
0.1 Ω	47.6 pH	11.5 fF

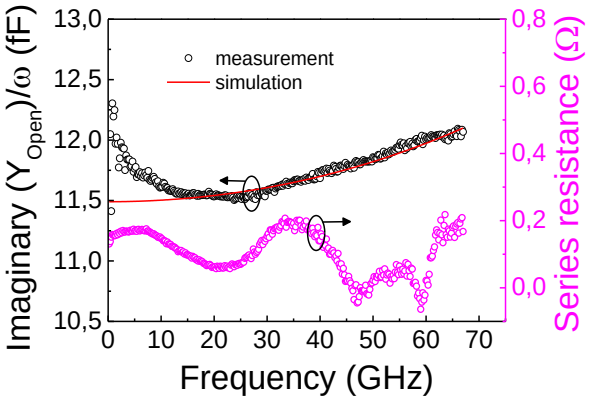

Figure 4.10. Extracted parasitic elements associated with the Pads and access lines.

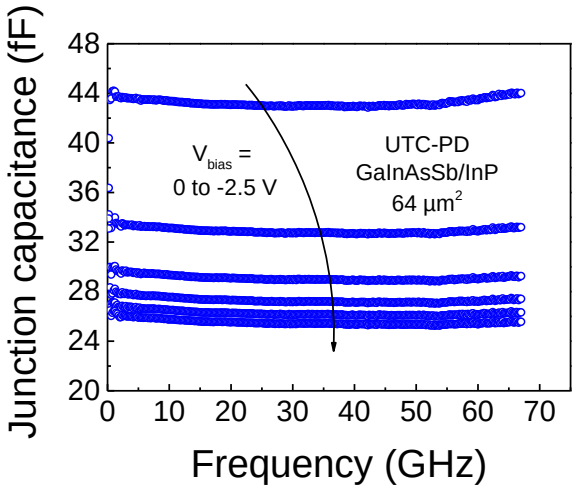

Figure 4.11. Extracted GaInAsSb/InP UTC-PD junction capacitances under various reverse bias.

4.1.2.2 InGaAs/InGaAsP UTC-PD de-embedding

The de-embedding methods used for this technology generally rely on on-wafer *S*-parameter measurements of different dedicated test structures, which are then subtracted from the global S-parameter measurements of the devices under test. The number of test structures and the complexity of the de-embedding method depend mainly on the geometry of the device as well as the frequency at which it operates. In this section, we show the limitations of conventional de-embedding methods at high frequencies (110 GHz) when using the Open and the Short test structures. We then propose a new de-embedding method that we have developed and that can be adapted to different designs of test structures and the frequency range used.

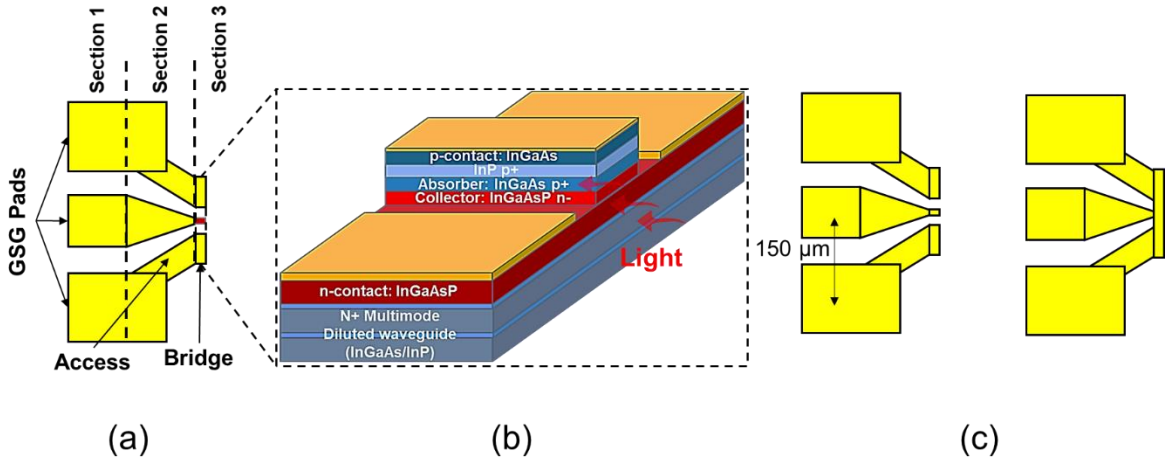

Figure 4.12. (a) Schematic of the UTC-PD structure connected to the GSG pads and the access lines (b) cross section of the UTC-PD active region (c) complete Open and Short test structures.

The InGaAs/InGaAsP UTC-PDs under test have been fabricated by III-V Lab [82]. The UTC-PD structure is formed by a mesa device connected to a waveguide by evanescent coupling. The device can be biased via the P+ and N+ doped contacts, above and below it,

respectively. On both sides of the mesa, the access lines are formed, which are connected up to the GSG pads (Figure 4.12 (a) and (b)).

The layout of the pads and the access lines of the UTC-PD is presented in Figure 4.12 (c). The signal pad has a size of 75×80 μm^2 with a probe pitch of 150 μm between the signal and ground pads. The pads are connected to access regions through 50 Ω CPW transmission lines which then end on to a mesa bridge.

To remove the contributions of pads and access lines in order to obtain the intrinsic characteristics of the UTC-PDs, complete (including the mesa bridge accesses) Open and complete Short test structures have been designed and fabricated at III-V Lab and characterized

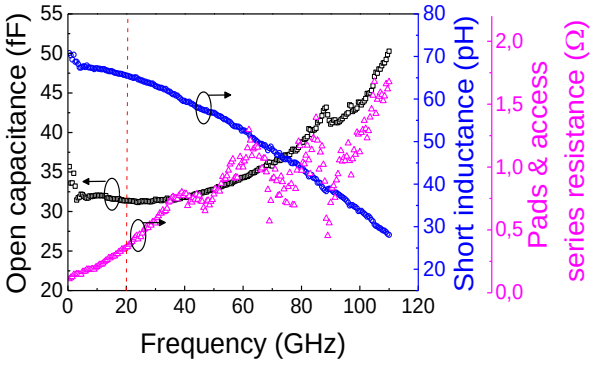

Figure 4.13. Extraction of capacitive, inductive and resistive parasitic equivalents to the pads and access lines.

at IMS laboratory. An off-wafer SOLT calibration on CS-5 substrate was used to bring the measurement reference planes at the probe tips. The on-wafer S-parameter measurements were then carried out up to 110 GHz using an Agilent E8361 PNA, with frequency extenders for the 67–110 GHz frequency range, using Picoprobe tips.

The complete Open and complete Short test structures are ideally modelled by a capacitance, resistance and an inductance. The results in Figure 4.13 indicate that this approximation is only valid up to 40 GHz, beyond which there is a frequency dependence of these electrical equivalent elements. The observed behavior can more likely be explained by an equivalent distributed electrical network.

In order to develop the latter model, complementary test structures were designed and fabricated. These include: (i) a Pad-Short and a Pad-Open (Figure 4.14 (a)) structure for the extraction of inductive and capacitive parasitic due to the pads, (ii) mesa-free Short and Open (Figure 4.14 (b)) structures for the extraction of the inductive, resistive and capacitive parasitic caused by the access lines. Finally, the complete Open and Short test structures are used for the extraction of inductive and capacitive parasitic caused by the mesa. A more detailed description of this new method has been presented in the next section.

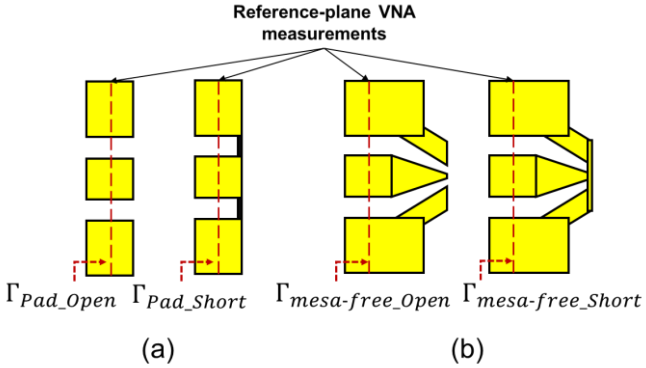

Figure 4.14. Complementary test structures: (a) Pad-Open and Pad-Short (b) mesa-free Open and mesa-free Short.

The accuracy of the new de-embedding method proposed in this work relies on the complete description of the global S-parameter matrix. All four matrix elements have been taken into account and no simplifications have been made, i.e. without the assumption of symmetry of the access that may introduce errors. In order to determine the matrix elements, construction of electrical equivalent circuits for the pads and the access lines is necessary. Next, a two-port simulation can be performed to determine its four matrix elements.

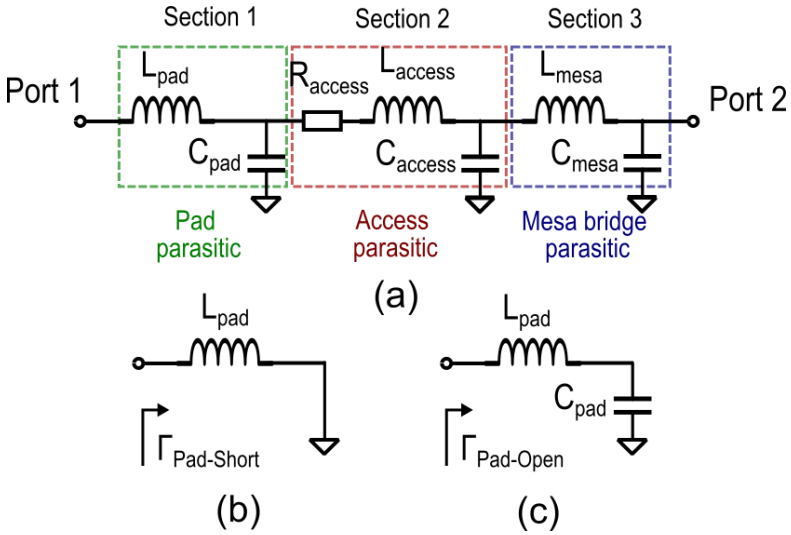

Figure 4.15. (a) Global electrical equivalent circuit of the pads and the access of the UTC-PD; (b) electrical equivalent circuit of the Pad-Short (c) electrical equivalent circuit of the Pad-Open.

The global equivalent circuit of the pads and the access lines is constructed using three cascaded sections, as shown in Figure 4.15 (a). The first section represents the electrical equivalent circuit of the pads. The equivalent parasitic elements of the pads can be determined from the Pad-Short and the Pad-Open test structures and their equivalent circuits (Figure 4.15 (b) and (c)). The inductive element is modelled by an inductance, L_{Pad}, which can be extracted from the Pad-Short reflection coefficient, $\Gamma_{Pad-Short}$, converted to an equivalent impedance, $Z_{Pad-Short}$. However, in addition to the pad inductances, L_{Pad} also includes an inductance for the return path to the ground (connection between the pads). So a correction should be made in the extracted value of the pad inductance through $Y_{Pad-Open}$ as:

$$Y_{Pad-Open} = j\frac{C_{pad} \cdot \omega}{1 - L_{pad} \cdot C_{pad} \cdot \omega^2} \tag{4.9}$$

At low frequency, the imaginary part of $Y_{Pad-Open}/\omega$ tends to the pad capacitance, C_{Pad}. At high frequency, an optimization on the value of L_{Pad} corrects the initial value determined from the Pad-Short test structure. The importance of this step can be understood more clearly when we write the first order expansion of $Im(Y_{Pad-Open})/\omega$:

$$\frac{Im(Y_{Pad-Open})}{\omega} \approx \left(L_{pad} \cdot {C_{pad}}^2\right) \cdot \omega^2 + C_{pad} \tag{4.10}$$

Here, the coefficient $\left(L_{pad} \cdot {C_{pad}}^2\right)$ is the driving factor in equation (4.9). Since at this point C_{Pad} has already been determined, the next parameter to be optimized is L_{Pad}. The results obtained are shown in Figure 4.16 (a) and (b). A value of 15 fF was extracted for C_{Pad} and a value of 18 pH was determined for L_{Pad} after correction.

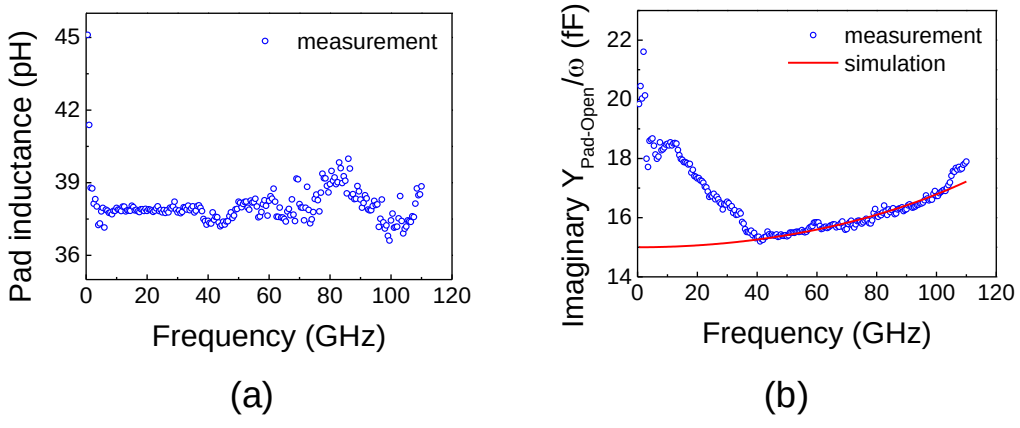

Figure 4.16. Frequency dependence of the Pad-Short inductance (b) imaginary part of the Pad-Open admittance.

The second section of the global equivalent circuit represents the mesa-free access regions. The corresponding parasitic elements can be determined from the mesa-free Short and Open test structures using their respective equivalent circuits (Figure 4.17 (a) and (b)). The parasitic lumped elements, R_{access}, L_{access} and C_{access} can be determined from the reflection coefficients, $\Gamma_{mesa-free-Short}$ and $\Gamma_{mesa-free-Short}$, de-embedded from pad parasitic elements.

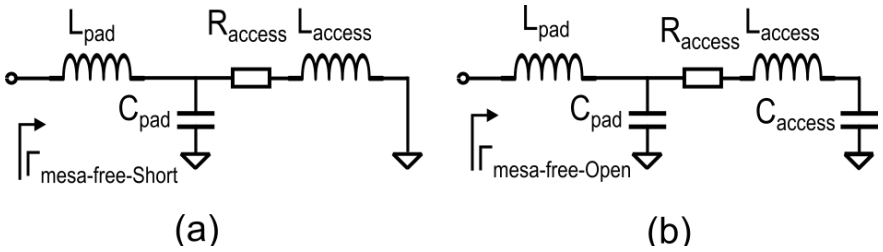

Figure 4.17. Electrical equivalent circuit of the mesa-free access test structures (a) Short (b) Open.

The same method was performed on the mesa-free access Open and Short test structures. The inductance remains overestimated (Figure 4.18 (a)), hence an optimization step was used for correcting the extracted value of the inductance. The sum of the capacitances equivalent to the pads and the mesa-free access, $C_{Pad} + C_{access}$, can be determined at low frequency from the imaginary part of $Y_{mesa-free-Open}/\omega$ (Figure 4.18 (b)). Then the inductance is corrected by optimizing the equivalent circuit model in the high frequency region. A value of 11 fF was extracted for C_{access} and a value of 28 pH was determined for $L_{access-corrected}$. The value of the resistance was determined from the real part of $Z_{mesa-free-Open}$, with an average value of 0.8 Ω (Figure 4.18 (a)).

The third section of the global circuit represents the mesa bridge access lines. The parasitic elements can be determined from the complete Short and complete Open test structures and their equivalent circuits (Figure 4.19 (a) and (b)). A similar process was followed as before to obtain the results shown in Figure 4.20. C_{mesa} and L_{mesa} were extracted to yield values of 5 fF and 5 pH, respectively.

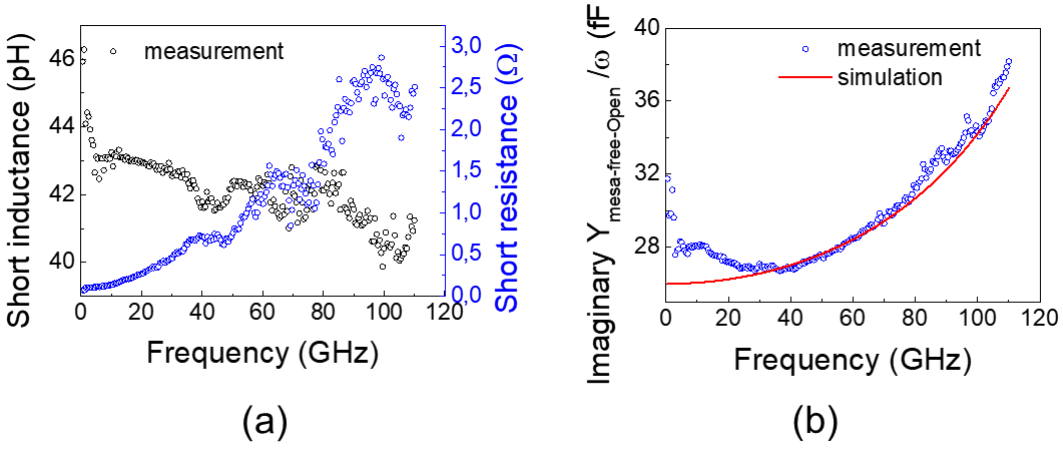

Figure 4.18. (a) Frequency dependence of mesa-free Short inductance and resistance (b) imaginary part of mesa-free Open admittance.

The parasitic elements, extracted for each segment of the whole electrical equivalent network representing the pads and the access line model, are summarized in Table 4.3.

Table 4.3. Extracted values of the lumped electrical elements, equivalent to the pads and access lines for the InGaAs/InGaAsP UTC-PDs.

L_{Pad}	C_{Pad}	R_{access}	L_{access}	C_{access}	L_{mesa}	C_{mesa}
18.0 pH	15.0 fF	0.8 Ω	28.0 pH	11.0 fF	5.0 pH	5.0 fF

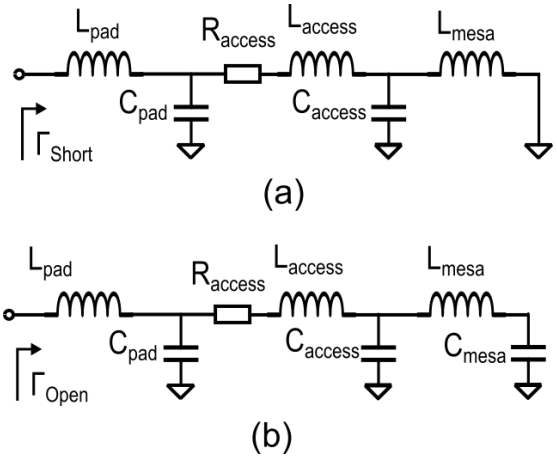

Figure 4.19. Electrical equivalent circuits of the complete (a) Short and (b) Open test structures.

Once the equivalent circuit of the pads and the access regions is accurately extracted, the intrinsic device S-parameter matrix can be determined. The extraction results for the electrical equivalent circuit elements in the intrinsic UTC-PD model, namely the junction capacitance, $C_{jT}(V_d)$, and the series resistance, R_S, (real part of $Z11$ at high frequency) are presented next in Figure 4.21, comparing the three de-embedding methods discussed in this chapter.

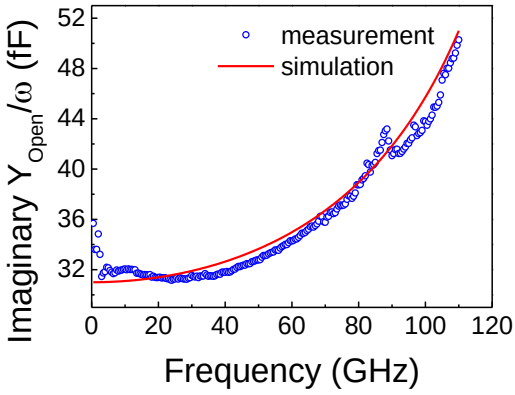

Figure 4.20. Imaginary part of the admittance of the complete Open test structure.

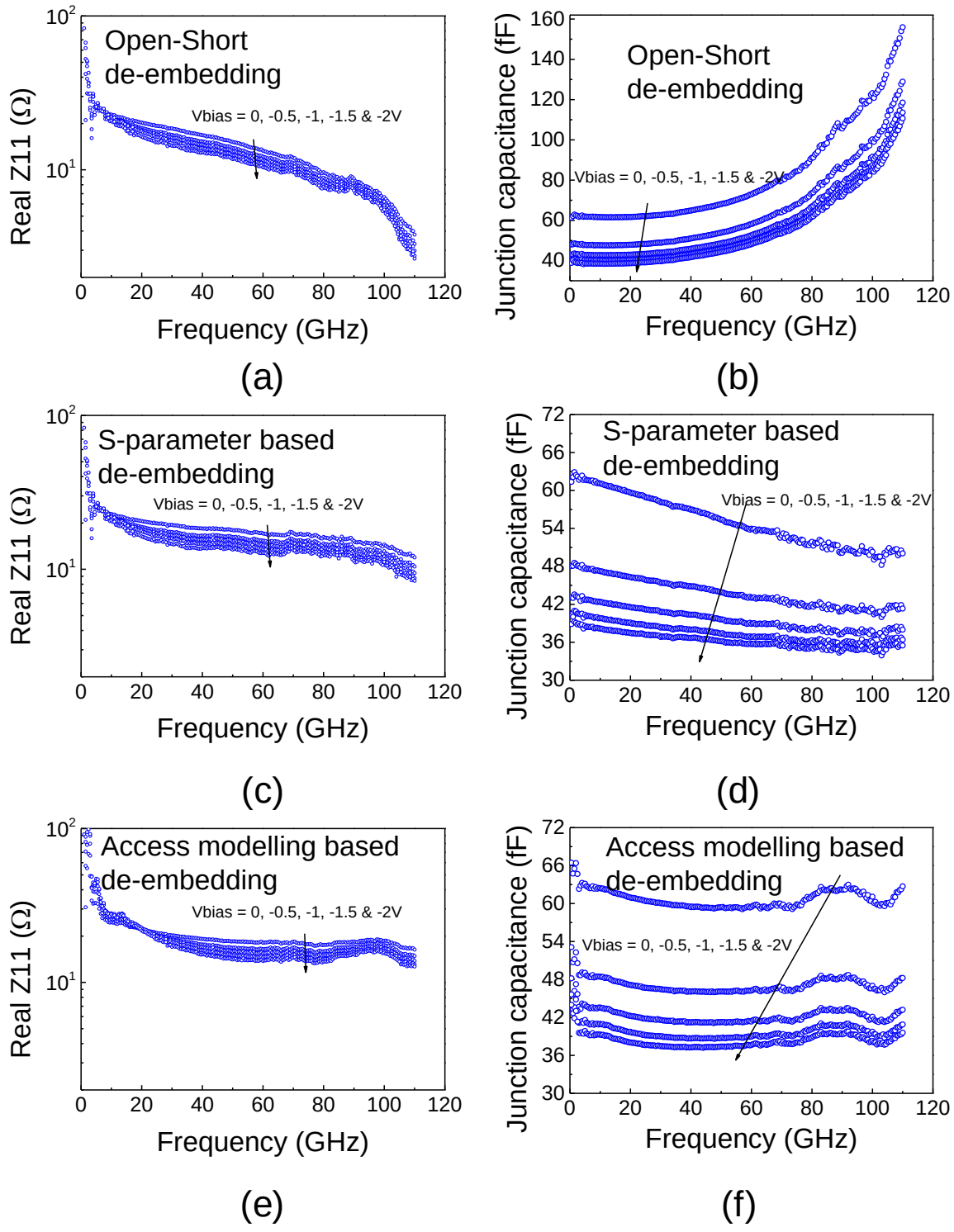

Figure 4.21. De-embedded real part of Z11 and junction capacitance of a InGaAs/InGaAsP UTC-PD, with an active area of 5x25 μm², as function of frequency obtained using the (a) Open-Short method (b) S-parameter based method (c) proposed access modelling-based method.

As expected, the results obtained with the two conventional de-embedding methods (Open-Short and S-parameter based) show a frequency dependence of the equivalent circuit elements (Figure 4.21 (a)-(d)). Among these two conventional methods, the S-parameter based method shows relatively better results over the whole frequency range, given that only one type of test structures, the complete Open and complete Short, were available. Provided that we have all

the test structures necessary to construct the distributed model, our proposed access modelling-based method remains more accurate and reliable up to 110 GHz (Figure 4.21 (e) and (f)), compared to other conventional methods.

4.1.2.3 InGaAs/InP UTC-PD de-embedding

For the InGaAs/InP UTC-PD technology, the TLM based distributed de-embedding method discussed before was applied. Taking advantage of this methodology, a dedicated InGaAs/InP UTC-PD Open test structure was characterized using the same setup and measurement procedure as the one used for the InGaAs/InGaAsP UTC-PDs test structures.

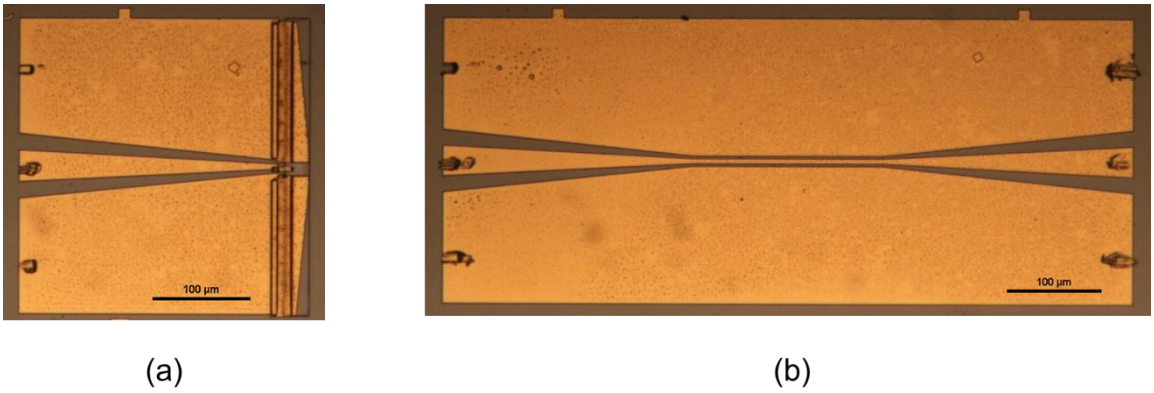

Figure 4.22. (a) Microscope image of the Open test structure (b) microscope image of the Thru test structure.

The Open test structure (Figure 4.22 (a)) was modelled by a $R_nL_nC_n$ network consisting of nine cascaded sections. This was achieved by optimizing the $\sum_{i=1}^{N=9} C/N$ and $\sum_{i=1}^{N=9} L/N$ values on the imaginary part of the measured Y_{Open}/ω, as shown in Figure 4.23 (a). Note here that since we did not have a Short test structure, we used a Thru test structure (Figure 4.22 (b)) to determine the series resistance, $\sum_{i=1}^{N=9} R/N$. This was achieved by first converting the measured two-port S-parameters into an $ABCD$ transfer matrix, then by determining the complex propagation constant, $\gamma = \alpha + j\beta$, and the characteristic impedance of the Thru test structure, Z_c, from the $ABCD$ matrix (Figure 4.23 (b)). Finally, the linear series resistance, R_{Thru}, (Figure 4.23 (c)) was determined from the real part of the product $\gamma \cdot Z_c$ [29]. Multiplying R_{Thru} by the length of the pads and the access lines (278 µm) of the InGaAs/InGaAsP UTC-PDs, we obtain $\sum_{i=1}^{N=9} R/N$. The number of the $R_nL_nC_n$ cascaded stages is determined to be a bit high in this case since, on one hand, we performed the measurements at higher frequencies (up to 110 GHz) thus necessitating more elements to obtain a flat-frequency response, and, on the other hand, because the access lines of the test structures are relatively longer than the previous case. The extracted values of these elements are reported in Table 4.4. Once the external passive electrical equivalent network is accurately modeled, two-port S-parameter simulations of the distributed RLC network were used to determine the intrinsic parameters of the UTC-PDs by applying equation (4.7).

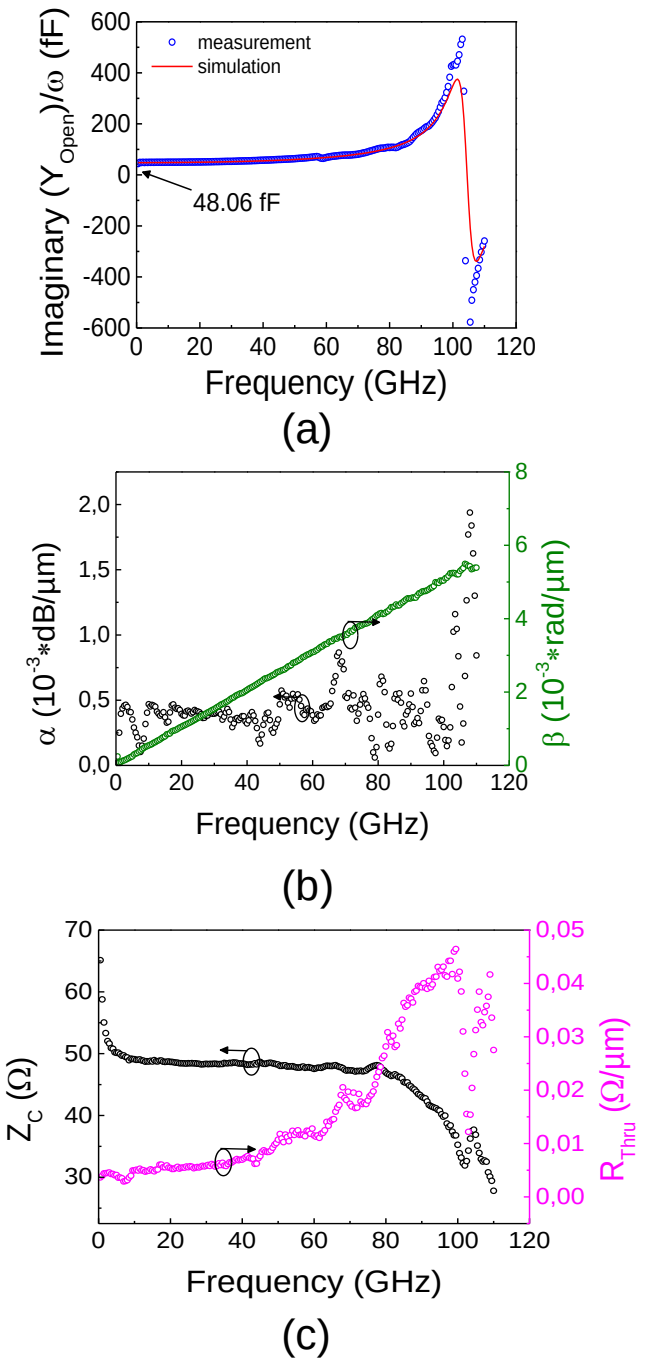

Figure 4.23. (a) Extracted LC parasitics of the equivalent circuit for the InGaAs/InP UTC-PD Open test structure (b) extracted attenuation constant α, and phase constant β of the Thru test structure (c) extracted characteristic impedance, Z_c, and calculated linear series resistance R_{Thru}, of the Thru test structure.

Table 4.4. Extracted values of the R, L, and C lumped elements from InGaAs/InP UTC-PD Open and Thru test structures.

R	L	C
1.5 Ω	106.7 pH	48.1 fF

4.2 Parameter extraction and compact model validation

The parameter extraction method described in this thesis has been developed according to the standard extraction flow used for bipolar transistor technologies. To begin the extraction process, an initialization step for the physical and technological parameters is necessary. Next, a sequence of measurements and parameter extraction steps are followed leading to the determination of the intrinsic and extrinsic parameters for the DUT, as summarized in the flowchart in Figure 4.24. In the subsequent paragraphs, the methodology flow is further detailed.

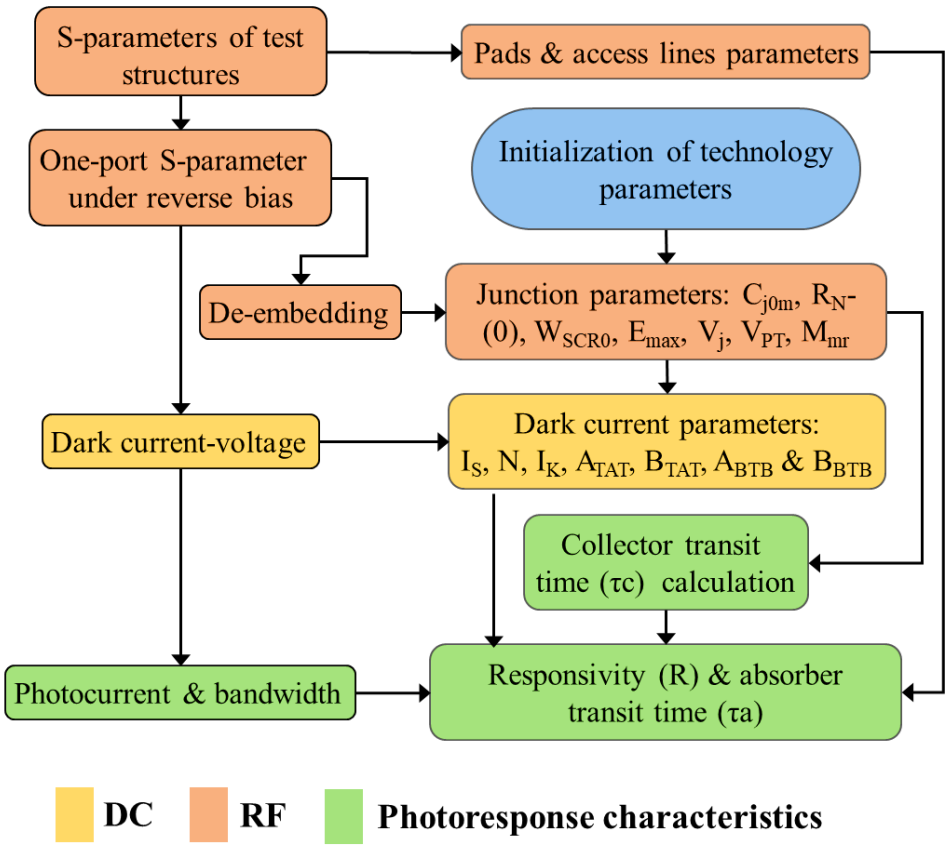

Figure 4.24. Methodology flow of the measurements and the parameter extraction of the UTC PD.

One-port S-parameters of the test structures are first measured to extract the electrical equivalent circuit elements associated with the RF pads and access lines. It is important to note that the design of the test structures can vary from one technology to another. Therefore, the de-embedding method must be adapted each time to the available test structures. Subsequently, one-port S-parameter measurements at various biases, followed by a de-embedding process,

can be performed to access the intrinsic S-parameters of the UTC-PDs. By converting these S-parameters to Y or Z-parameters, junction capacitance and series resistances of the equivalent electrical circuit for the UTC-PD compact model can be extracted. After determining the junction parameters, forward and reverse current measurements without illumination are used to extract the DC characteristics of the UTC-PD junction, as well as the reverse current parameters (band-to-band tunnel current and trap-assisted tunnel current parameters).

Finally, static photocurrent and bandwidth measurements under illumination are exploited to determine the optical parameters such as responsivity, R, and the transit times: the transit time in the absorber, τ_a, and the transit time in the collector, τ_c. It is important to note that unlike conventional one-port S-parameter measurements that can be de-embedded, the bandwidth measurements still include the contributions from the pads and access lines. The extracted values of these extrinsic parasitic contributions are therefore re-injected into the final model to obtain realistic simulation results.

4.2.1 Intrinsic junction capacitance

As mentioned above, the measurements of the device S-parameters (after de-embedding at different bias points and then converted into equivalent Z-parameters) can be used to extract the junction capacitance and its bias dependency. Based on how the equivalent circuit of the compact model has been defined, the total junction capacitance can be extracted from the imaginary part of $Z11$:

$$C_{jT}(V_d) = -\frac{1}{Im\big(Z_{11}(V_d)\big) \cdot \omega} \tag{4.11}$$

The junction capacitance parameters: C_{j0m},V_j and M_{mr}, described in chapter 2, can be extracted by taking the logarithm on both sides of the first term of equation (2.22), in order to linearize it. However, the best linear regression is achieved by performing an iteration on V_j, at low reverse voltages. Once C_{j0m} is determined, the following set of parameters: W_{SCR0}, $E_{max}(V_d = 0)$ and $R_N{-}(0)$, can be calculated. Finally, an optimization on the V_{PT} value at high voltage can be used to determine C_{j0l}.

For InGaAs/InGaAsP UTC-PDs, measurements up to 110 GHz, under a reverse bias ranging from 0 to -2V, were performed and followed by the de-embedding procedure presented previously. Figure 4.25 shows the extracted junction capacitance as a function of the reverse bias for InGaAs/InGaAsP UTC-PD with an active area of 5×25 μm^2.

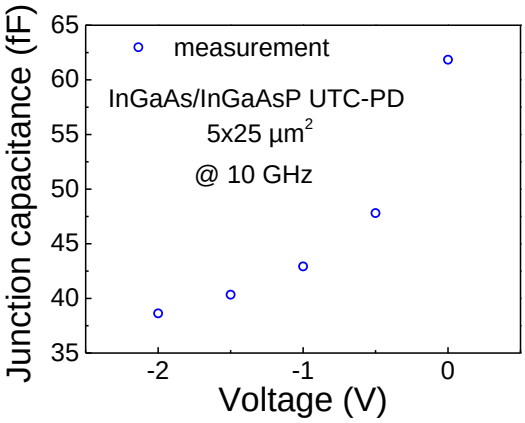

Figure 4.25. InGaAs/InGaAsP UTC-PD junction capacitance as function of reverse bias.

The parameter extraction for the junction capacitance and compact model validation are shown in Figure 4.26 (a) and (b). A comparison between the implemented new model and the one using classical theory (Figure 4.26 (b)) shows that at low reverse voltages, both models are comparable. When the reverse voltage exceeds -1.5 V, the classical model does not follow the real device behavior. This is because, when the collector is completely depleted, the bias dependence of the junction capacitance becomes weaker due to the high doping level of the waveguide (or the N-contact). That is, the dependence of the junction capacitance on the bias voltage follows the doping profile.

It is important to note that the reverse voltage in our measurements has not been pushed beyond -2 V, to avoid the risk of degrading the DUT, as we had only one device per geometry available for our measurements.

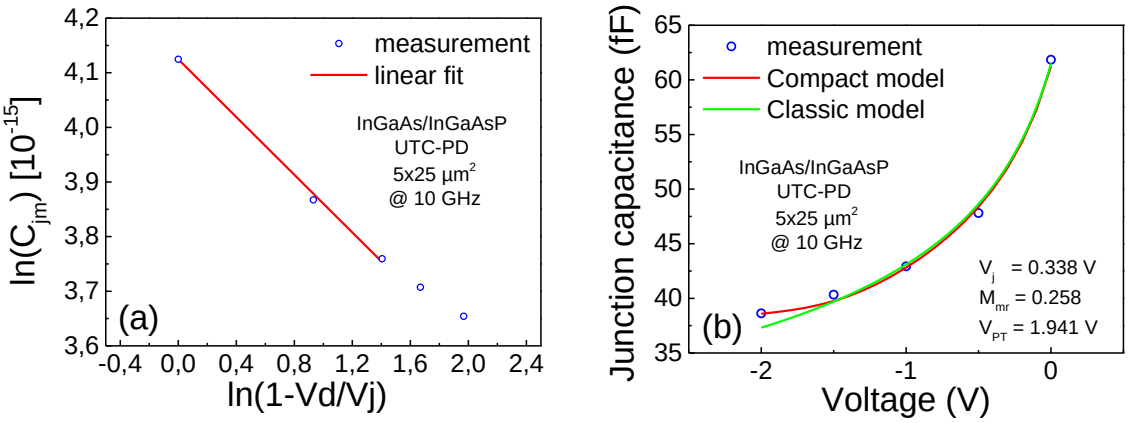

Figure 4.26. (a) Log-log plot of the junction capacitance as function of the bias (b) compact model validation for junction capacitance of InGaAs/InGaAsP UTC-PDs.

Similarly, S-parameter measurements up to 67 GHz, under a reverse bias ranging from 0 to -2.5 V ,were performed on GaInAsSb/InP UTC-PDs with an active area of 64 μm^2, followed by the de-embedding procedure presented previously. The same procedure for extracting junction capacitance parameters was applied in this case. The results shown in Figure 4.27 indicate an excellent agreement between the compact model and the measurement, again highlighting the improvement in simulation accuracy for our proposed model.

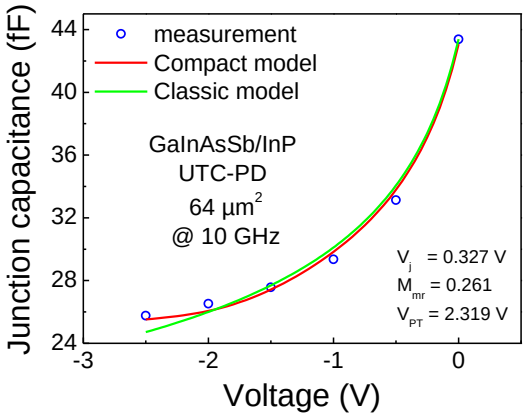

Figure 4.27. GaInAsSb/InP UTC-PD junction capacitance validation: comparison between measurements, classical model and our developed compact model.

Finally, for the InGaAs/In UTC-PDs, similar measurements up to 110 GHz under reverse bias ranging from 0 to -2V were performed followed by the de-embedding procedure presented previously. In contrast to the InGaAs/InGaAsP and GaInAsSb/InP UTC-PDs, the junction capacitance of the InGaAs/InP UTC-PD follows the classical model (see Figure 4.28). This can be attributed to the collector being narrower in the InGaAs/InP UTC-PDs, with a collector thickness of 127 nm compared to that of 425 nm for the InGaAs/InGaAsP and 225 nm for the GaInAsSb/InP UTC-PDs. At zero bias, the collector is fully depleted. As the reverse voltage increases, the depletion region extends mainly into the absorber which is gradually doped.

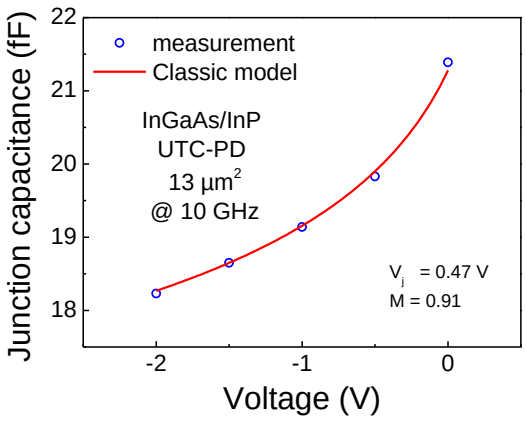

Figure 4.28. InGaAs/InP UTC-PD junction capacitance model validation: classical model.

Since the depletion region of the UTC-PD is located exclusively in the mesa region, the junction capacitance scales with the active area. However, to improve scaling accuracy of the model, a dimensional parameter is introduced to account for the mesa etch error, which can be

added or subtracted from the active area calculation. SEM micrographs can clarify the error to be taken into account due to the etching. For InGaAs/InGaAsP UTC-PDs, an etching error, $\Delta w_{mesa} = \Delta l_{mesa}$, was taken into account for their widths and lengths. For the GaInAsSb/InP UTC-PDs, containing both circular and square geometries, an etching error radius ΔR_{mesa} was considered for the circular geometry and an etching error Δw_{mesa} was considered for the square geometry.

The extracted intrinsic junction capacitance as a function of applied voltage for different geometries under test shows excellent scalability and very good agreement with the measurement results, as summarized in Figure 4.29. Note that, the junction capacitance extraction procedure is performed at 10 GHz to avoid any inductive contribution.

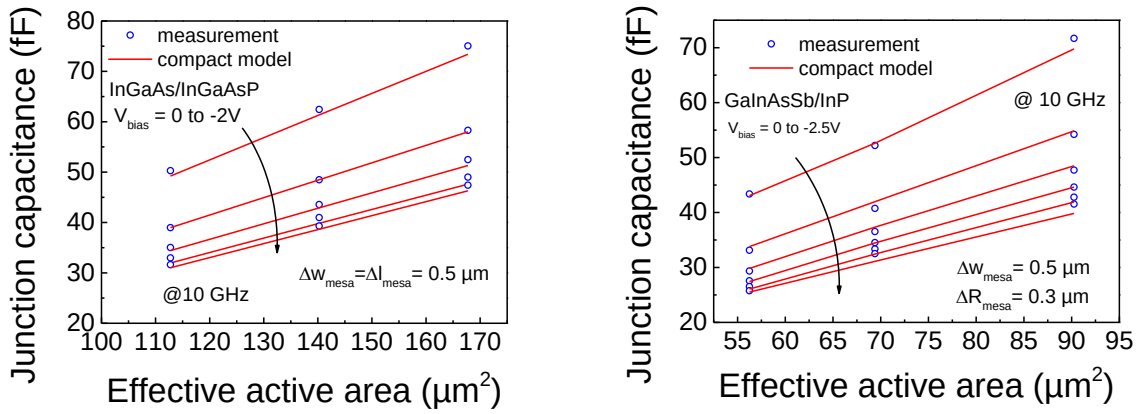

Figure 4.29. UTC-PD junction capacitance as functions of the active device area and the applied reverse bias. Left: InGaAs/InGaAsP UTC-PD. Right: GaInAsSb/InP UTC-PD.

4.2.2 Series resistance

In the case of the InGaAs/InGaAsP UTC-PDs, the global series resistance, R_s, was extracted from the real part of the de-embedded $Z11$-parameter at high frequencies. Since, the contacts cover the entire mesa, it is easy to determine the associated scaling law by analyzing the effective area of the device geometry. However, due to the absence of LTLM structures, equation (2.43) (linking the global series resistance to the UTC-PD geometry and technology parameters) was reduced to:

$$R_s = \frac{\alpha}{l_{mesa}} + R_{N^-}(0) \cdot \frac{w_{Coll} - w_{SCR}(V_d)}{w_{Coll} - w_{SCR}(0)} \tag{4.12}$$

Where, $\boldsymbol{\alpha}$ (in Ω·m) is new fitting parameter.

The first term of the above equation reflects the dependence of the contact and spreading resistances on the length of the UTC-PD. The second term reflects the dependence of the collector resistance on the reverse voltage and it takes into account the geometry of the UTC-PD active area.

Figure 4.30 shows the global series resistance, R_S, extracted at 80 GHz, for the three geometries under test under various bias conditions. Since the collector is not completely depleted, as the reverse voltage increases, the collector resistance, R_{N^-}, decreases until it becomes negligible at full depletion. The global series resistances scale well within the length of the UTC-PD and conforms to the predicted law.

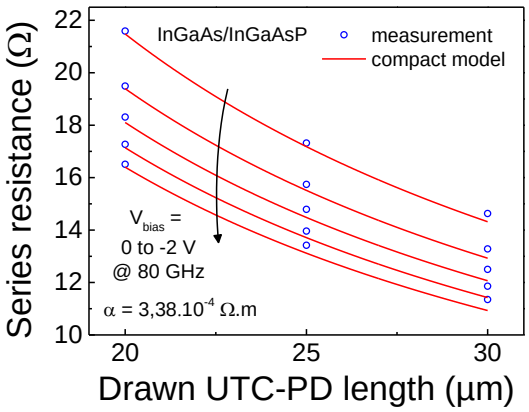

Figure 4.30. The extracted total series resistance at various reverse biases and for several lengths of the InGaAs/ InGaAsP UTC-PDs.

For the GaInAsSb/InP UTCPDs, the global series resistance values are extracted from the real part of $Z11$-parameter at a frequency of 60 GHz (Figure 4.31 (a)). A slight bias dependence was observed. However, this dependence is the opposite of what was expected, given the magnitude of the extracted resistances, this slight dependence might just be attributed to measurement uncertainly. Consequently, mean values have been extracted: 11.6 Ω, 10.7 Ω and 12.4 Ω for the UTC-PD geometries with 64 µm^2, 79 µm^2 and 113 µm^2 active areas, respectively. Contrary to the integrated waveguide InGaAs/InGaAsP UTC-PDs, the metallic contacts of the GaInAsSb/InP UTCPDs are located at the edge of the mesa. Additionally, the contact width varies for each geometry. It is therefore not surprising that the resistance does not scale with the mesa area and remains constant.

The InGaAs/InP UTC-PD have a structure similar to those of the GaInAsSb/InP UTC-PDs where the metal contacts are located at the edge of the mesa. A series resistance of 41.2 Ω was extracted at 80 GHz from the real part of $Z11$-parameter (Figure 4.31 (b)). Since real($Z11$) of the device tends towards the series resistance at high frequencies, we chose the highest possible value of the frequency range for extracting the series resistance (80 GHz for InGaAs/InGaAsP and InGaAs/InP UTC-PDs and 60 GHz for GaInAsSb/InP UTC-PDs) to ensure reliable parameter extraction.

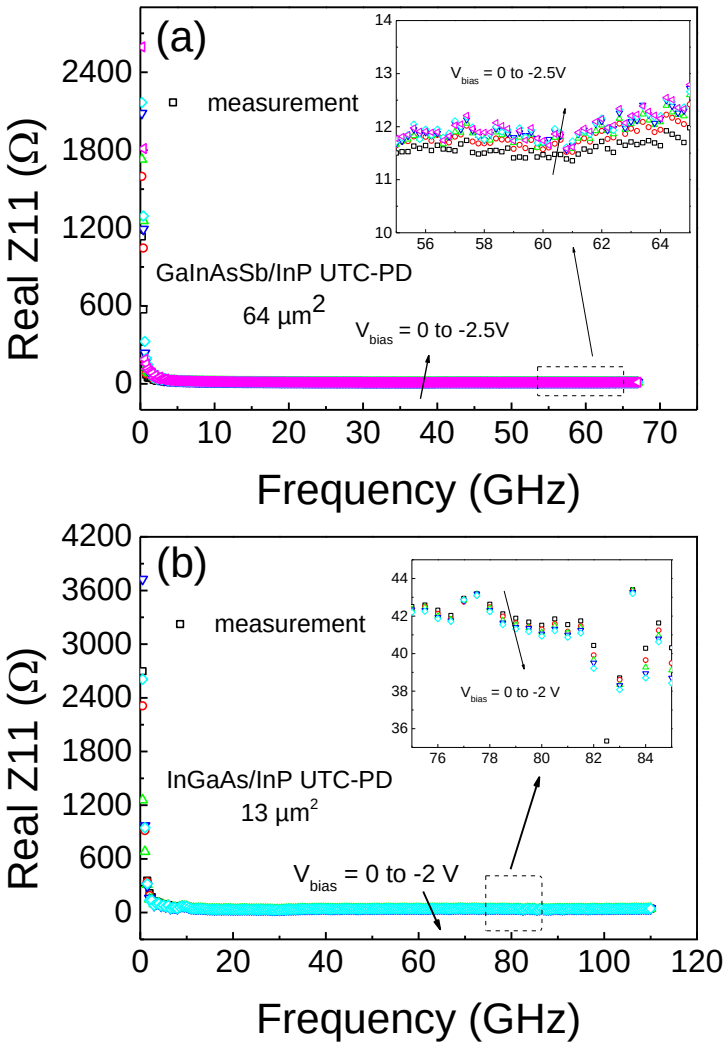

Figure 4.31. Measured real Z11 of (a) GaInAsSb/InP UTC-PD with active area of 64 µm² (b) InGaAs/InP UTC-PD of 13 µm² of active area.

1. Validation of RF characteristics

Once the compact model parameters have been extracted (without illumination), model validation for the S11 parameters is carried out. Figure 4.32 and Figure 4.33 show good model scalability for both the amplitude and phase of measured S-parameters for the different UTC-PDs studied. An excellent agreement between measurement and compact model simulation is observed for all geometries across all UTC-PD technologies, confirming the scalability and versatility of the compact model. Note that some *S*11 measurements (Figure 4.32 (a), (c), (e)) show fluctuations in the 80-100 GHz frequency range, which are not captured by the model.

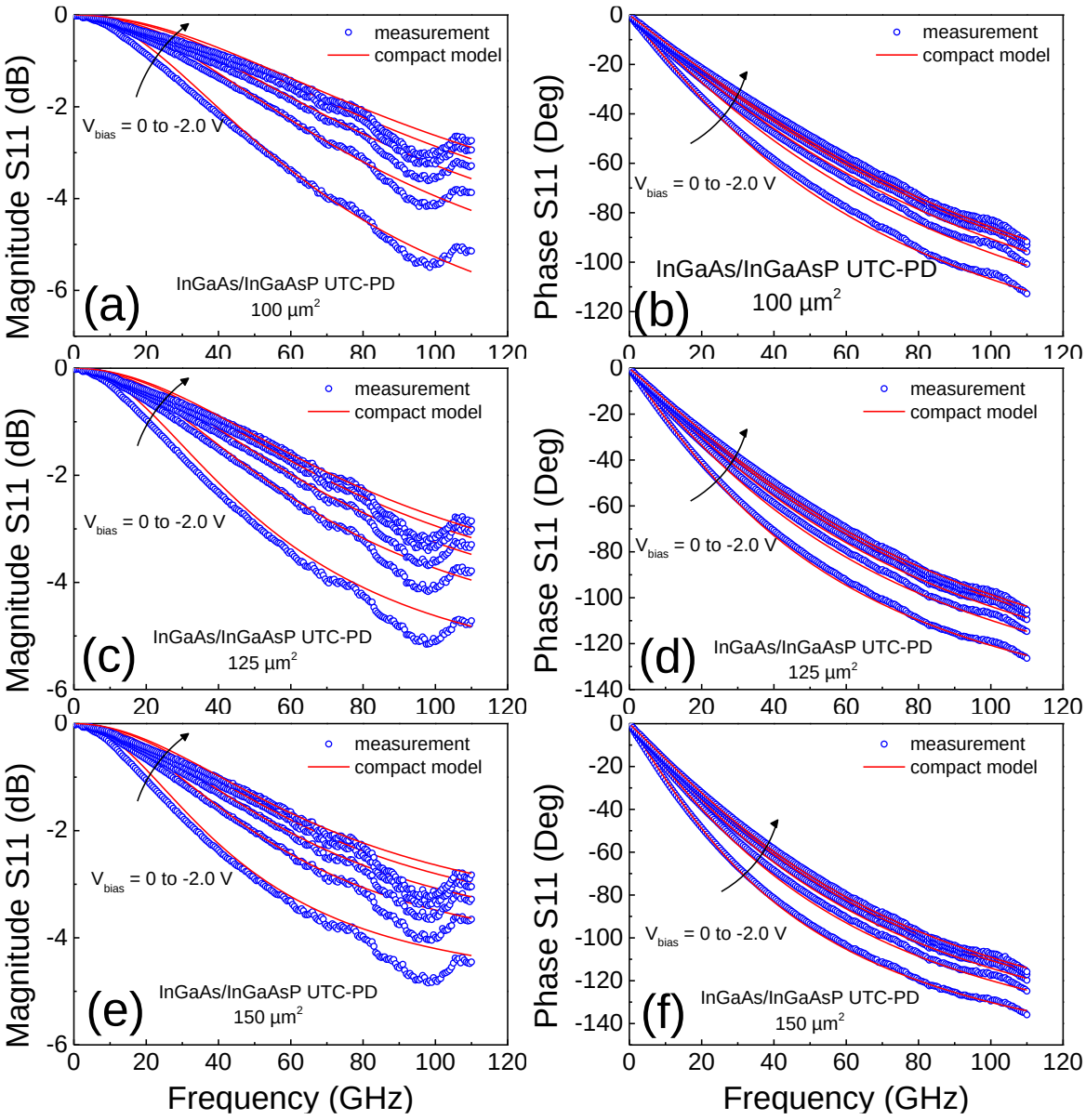

Figure 4.32. Measured (symbol) and simulated (lines) intrinsic S11-parameter for InGaAs/InGaAsP UTC-PDs under test: (a-c-e) magnitude in dB and (b-d-f) phase in degree with actives areas of 100, 125 and 150 µm².

The origin of these fluctuations lies with the reflection of the input signal from the chuck on which the wafer is placed, thus causing these fluctuations in the measured S11. This phenomenon has also been observed previously in other devices on InP substrate. Placing an

absorber between the wafer chuck and the device under test can significantly reduce these fluctuations, which was however not available during these series of characterizations.

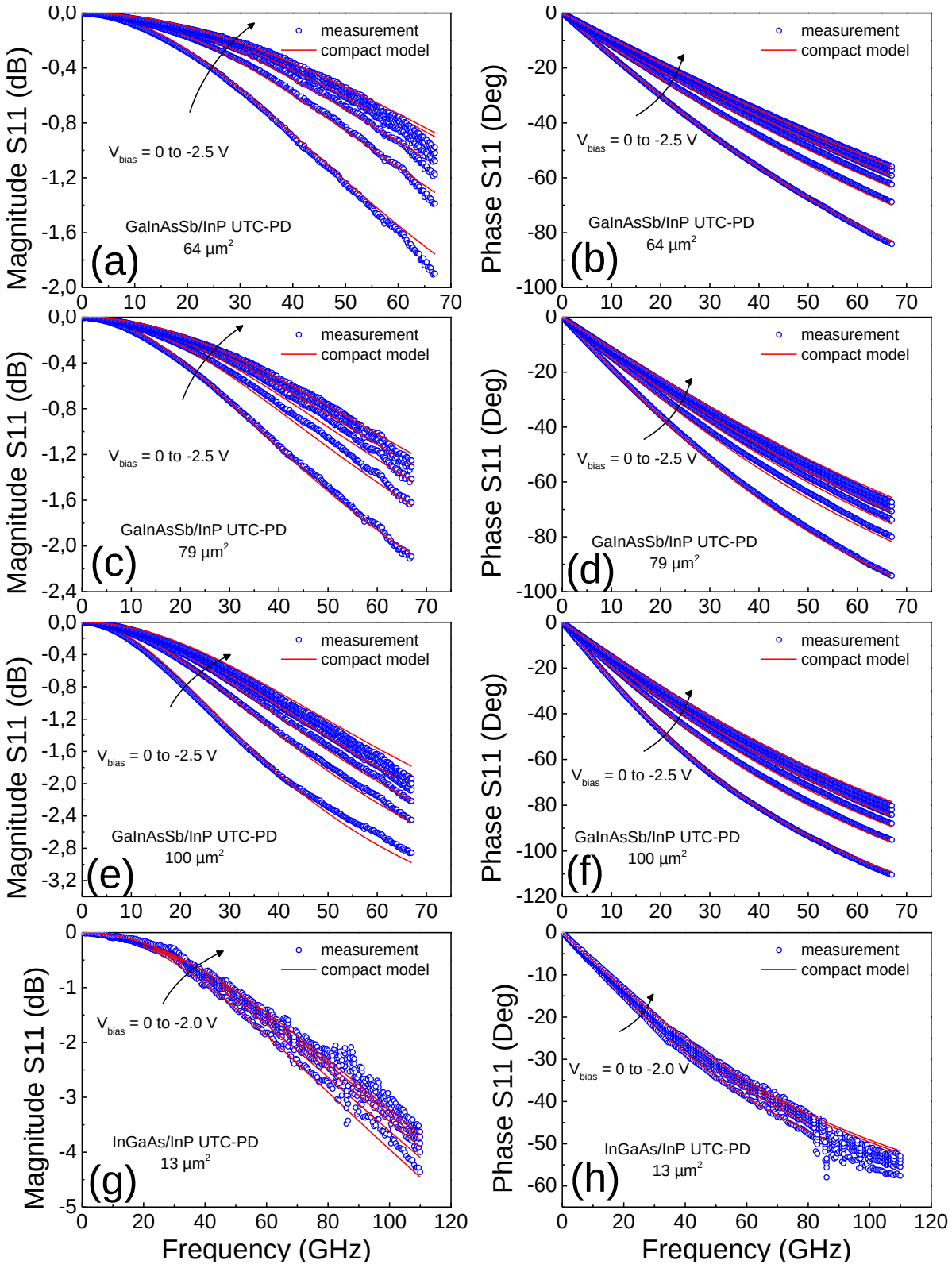

Figure 4.33. Measured (symbol) and simulated (lines) intrinsic S11-parameter for the UTC-PDs under test: (a-c-e) magnitude in dB and (b-d-f) phase in degree of GaInAsSb/InP UTC-PD with active area of 64, 79 and 100 µm² (g) magnitude in dB (h) phase in degree of InGaAs/InP UTC-PD with a 13 µm² active area.

4.2.3 Dark current

In order to extract the dark current and related compact model parameters of the UTC-PDs, current-voltage characterizations were performed under illumination.

For InGaAs/InGaAsP UTC-PDs, current–voltage characterizations were performed under a bias sweep in the range of (−3, 1) V on the three device geometries. Figure 4.34 shows the current-voltage measurements performed on a UTC-PD with an active area of 5×25 μm^2 at 25 °C. We observe a classical behavior under forward bias, with the current varying exponentially with the voltage. However, under reverse bias, we notice a current with at least two distinguishable contributions. As detailed in chapter 2, the compact model has been formulated to include analytical equations of band-to-band and trap-assisted tunneling currents under reverse bias. Model fitting against the measurements has been used for the extraction of different dark current parameters.

More specifically, in Figure 4.34, four regions, A, B, C and D, have been identified on the I-V characteristics of the UTC-PD. Each of these regions can be used for the systematic extraction procedure for compact model parameters specific to the highlighted region of operation, as detailed in the following.

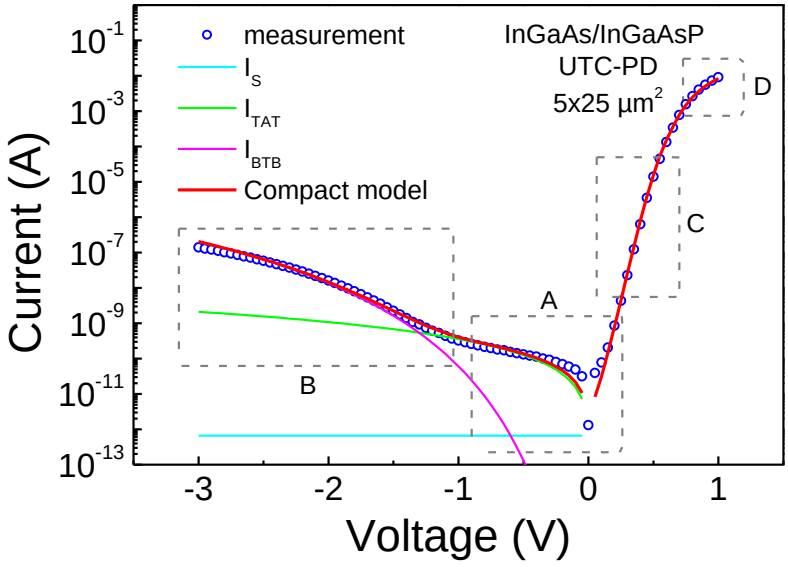

Figure 4.34. Measured (symbol) and simulated (lines) current-voltage characteristics of UTC-PDs with an active area of 5x25 μm^2.

Under low forward and reverse bias voltages (-1V, 0.2V), i.e. in region A, we extract the value of the saturation current, as well as the parameters of the trap assisted tunneling current.

At high reverse bias voltages (-3V, -1V), i.e. in region B, the current is mainly due to the band-to-band tunneling current and thus its associated parameters can be extracted.

At medium forward bias voltages (0.2V, 0.7V), i.e. in region C, the ideality coefficient can be extracted, along with the knee current parameter which reflects the transition from low to high injection.

Finally, in region D, total extracted series resistance (from RF characterization), can be re-injected as model parameter to fit the curve which, in turn, confirm the precision of the extracted value.

To model the temperature-dependence of the dark current parameters, current-voltage measurements were also performed at two additional temperatures: 15 and 35 °C. Note that the temperature dependence of the dark current in the compact model was taken into account through the $I_s(T)$ and $V_j(T)$ parameters.

Figure 4.35 (a) compares the DC characteristics measured at different temperatures with our compact model simulation. A good model accuracy has been demonstrated over the entire range of forward and reverse biases, at different temperatures for a 5×25 μm^2 UTC-PD. In addition, Figure 4.35 (b) shows the I-V characteristics of different device geometries, further confirming very good scalability of the compact model.

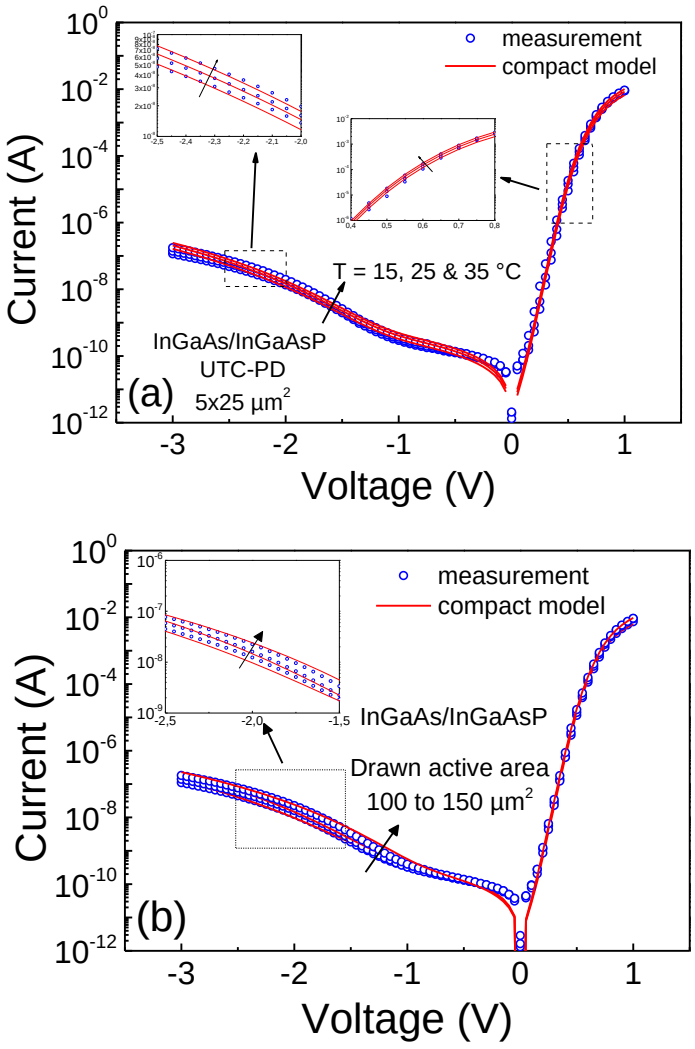

Figure 4.35. Measured (symbol) and simulated (lines) I-V characteristics of InGaAs/InGaAsP UTC-PDs: (a) current-voltage plot at different temperatures for a UTC-PD with an active area of 5x25 µm² (b) current-voltage characteristics of UTC-PDs with several active areas.

Similarly, the dark current compact model was validated on the GaInAsSb/InP and InGaAs/InP UTC-PDs following related parameter extraction from the current-voltage measurements. These measurements were performed in the bias range of (-5V, 1V) and (-3V, 1V) for the GaInAsSb/InP and InGaAs/InP UTC-PDs, respectively. All measurements were performed at room temperature (22 °C). The results presented in Figure 4.36 (a) and (b) compare the measured DC characteristics and the compact model simulations, demonstrating a good accuracy of the model over the entire forward and reverse bias ranges.

It is worth noting that a significant degradation of the InGaAs/InP UTC-PD DC and RF characteristics has been observed under optical illumination since the last set of measurement. This will be shown in the photocurrent discussion.

All UTC-PDs under test showed very low dark current levels (below 25 nA at -2V). The low values of the dark current imply a higher quality of the passivation of the junction in the UTC-PDs. The extracted dark current parameters of the three UTC-PD technologies are summarized in Table 4.5.

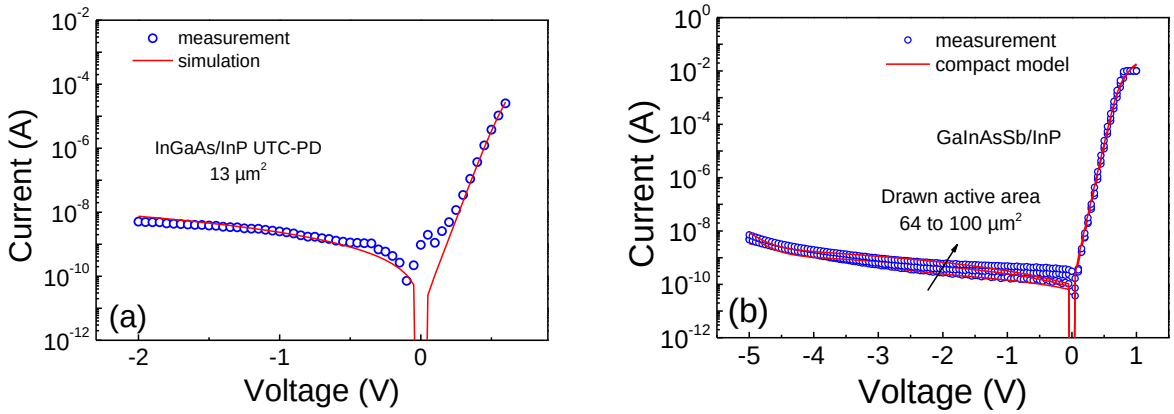

Figure 4.36. Measured (symbol) and simulated (lines) current-voltage characteristics of (a) InGaAs/InP UTC-PD (b) GaInAsSb/InP UTC-PDs with several active areas.

Table 4.5. Extracted parameters for the dark current compact model from measurements for the three UTC-PDs technologies investigated.

UTC-PD	J_s(A/m^2)	A_{TAT} (nA/V^2·m)	B_{TAT}(kV/cm)	A_{BTB} (nA/V^3)	B_{BTB} (kV/cm)	N	J_K (A/m^2)
InGaAs/InGaAsP	5.6×10^{-3}	558.75	5.1	1.95	5.4×10^{2}	1.16	4.01×10^{5}
GaInAsSb/InP	2.8×10^{-1}	86.1	65.0	0.9×10^{-3}	1.1×10^{3}	1.35	2.42×10^{6}
InGaAs/InP	7.0×10^{-1}	7.0×10^{3}	4.8	0.6×10^{-3}	6.6×10^{3}	1.45	3.16×10^{5}

4.2.4 Photocurrent

Once the dark current parameters of the model were extracted, photocurrent measurements under illumination were used for extracting other optical parameters. Among these, the responsivity has been chosen as an input parameter for the reasons discussed in chapter 2. Its value can be determined from current-voltage measurements under illumination and reverse bias.

For the InGaAs/InGaAsP UTC-PDs, photocurrent measurements were performed under an optical power ranging between 1.33 and 19 mW (as measured at the fiber tip) with a laser of 1.551 µm wavelength. Figure 4.37 (a)-(c) show the measured photocurrents for the geometries under test.

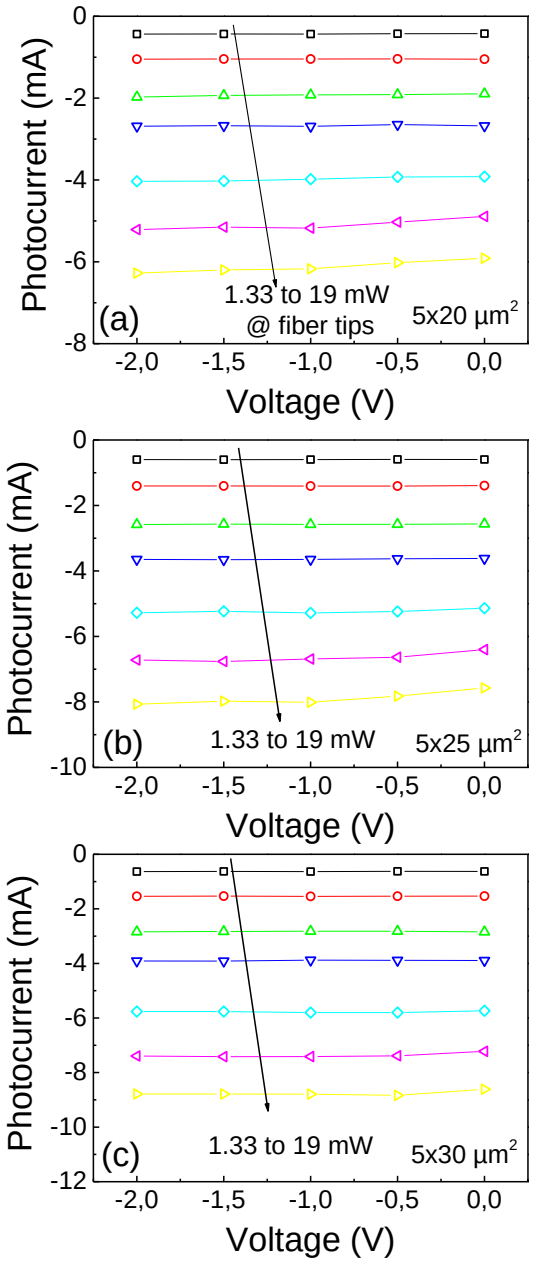

Figure 4.37. Measured photocurrent of InGaAs/InGaAsP UTC-PDs with the active area of (a) 5×20 (b) 5×25 and (c) 5 ×30 µm² as a function of reverse bias at different optical powers, at 22 °C.

Responsivity values of 0.33 A/W, 0.42 A/W and 0.46 A/W were found from the slope of the photocurrent versus optical power curve at -2 V for the 5x20, 5x25 and 5x30 µm² geometries respectively as shown in Figure 4.38.

In comparison, responsivity values greater than 0.7 A/W were measured on similar UTC-PDs at III-V Lab, as shown in Figure 4.39 (a) [82]. The lower responsivity values measured at the IMS laboratory are due to the tolerance of the lensed optical fiber- UTC-PD waveguide

coupling system, which is lower than the resolution of the micro-positioners we used in our setup (Figure 4.39 (b)).

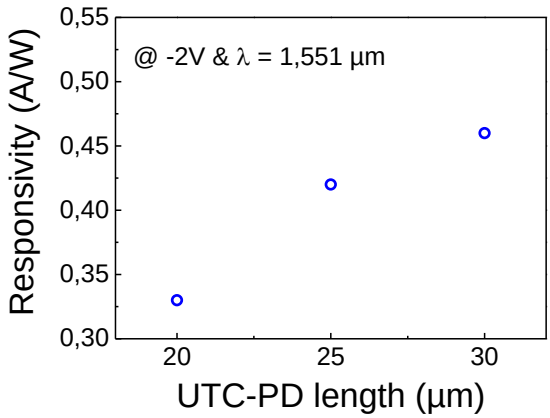

Figure 4.38. Measured responsivities of the InGaAa/InGaAsP UTC-PDs at 1.551 µm wavelength.

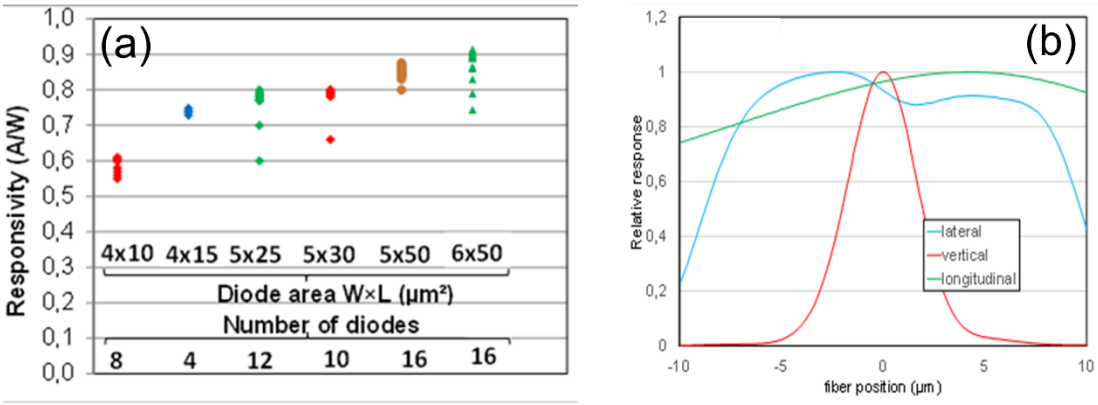

Figure 4.39. (a) Measured responsivities of the InGaAa/InGaAsP UTC-PDs at 1.55 µm wavelength for several UTC-PDs geometry (b) lensed optical fiber-UTC-PD integrated lens coupling tolerance measurements [82].

We recall that the measurements on the GaInAsSb/InP UTC-PDs were all performed at ETHZ, and a responsivity value of 0.094 A/W was measured [120].

For the InGaAs/InP UTC-PDs, the current-voltage measurements under illumination were performed at the IMS laboratory. Figure 4.40 (a) shows a significant degradation of the dark current compared to the first set of measurements. A responsivity of 0.036 A/W extracted at -2V is shown in Figure 4.40 (b).

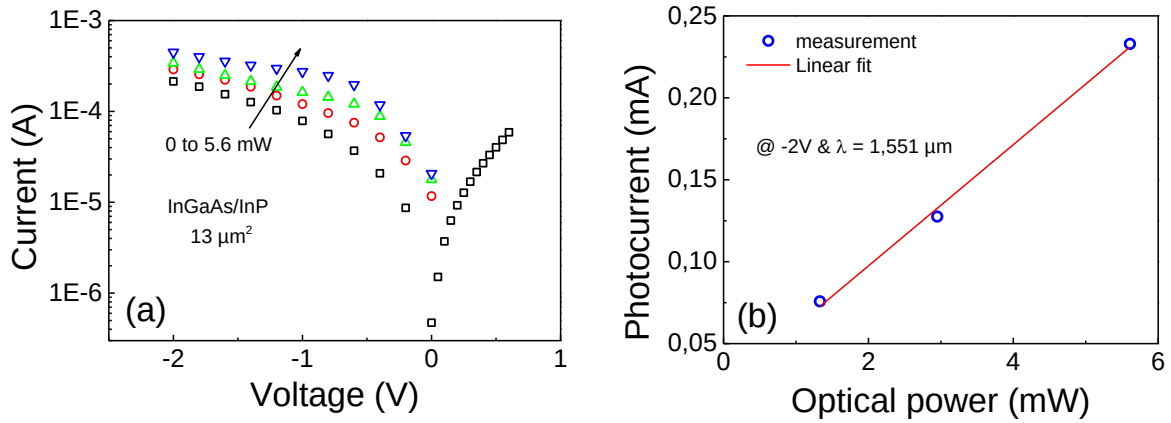

Figure 4.40. (a) Measured photocurrent-voltage characteristics and (b) photocurrent as function of input optical power of InGaAs/InP UTC-PDs.

4.2.5 Bandwidth

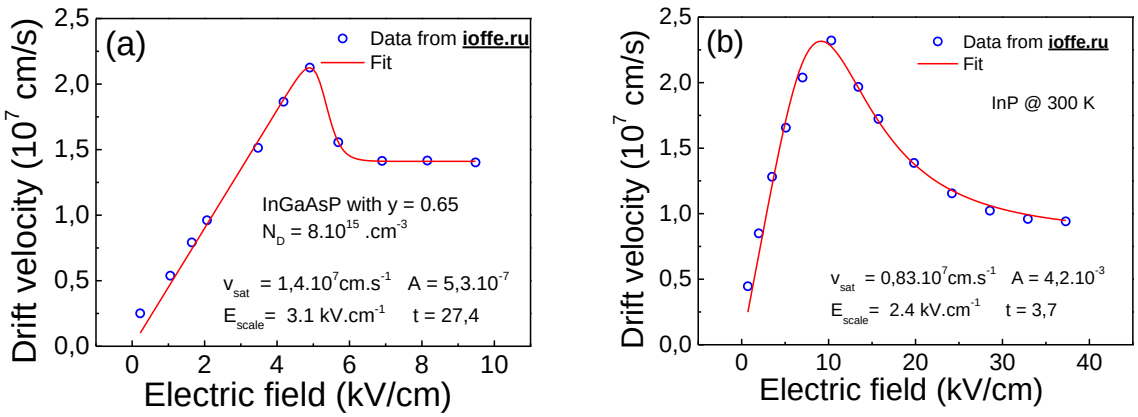

Figure 4.41. Electric field vs electron drift velocity for (a) InGaAsP (b) InP UTC-PDs [138].

According to how the compact model was formulated, the calculation of the electron velocity (or transit time τ_c) at the input of the collector can be used to reduce the number of parameters to be extracted (to only one parameter, τ_a), during bandwidth measurements. The calculation of τ_c can be done using the electric field-electron drift velocity (*E*-*v*) relationship. Figure 4.41 (a) and (b) shows the electric field-drift velocity characteristics taken from the literature for the InGaAsP and InP layers (the two collector materials of the UTC-PDs studied) [138].

Once the UTC-PD compact model was validated against the DC and RF characteristics (under non-illuminated operating conditions) along with the relevant optical parameters extracted from photocurrent measurements, the dynamic photo-response of the compact model was then validated for both InGaAs/InGaAsP and GaInAsSb/InP (UTC-PDs) technologies, for all available geometries and under different applied bias and optical power conditions.

For the InGaAs/InGaAsP UTC-PDs, the frequency-dependent photo-response was measured using two different techniques. The first set of measurements were performed on a calibrated heterodyne measurement bench, at III-V Lab, where all the UTC-PD geometries were biased at -2V under an optical power of 3 dBm. Extrinsic -3dB bandwidths ranging from 40

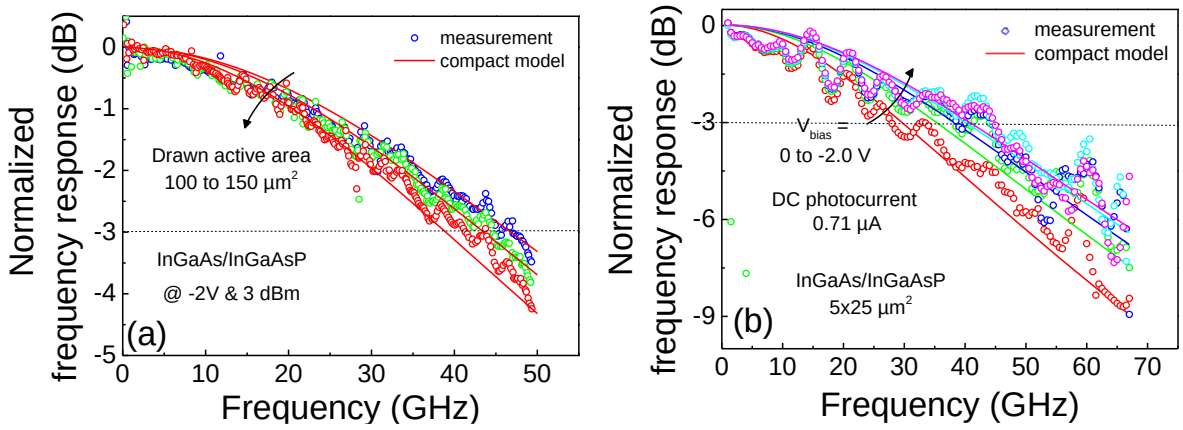

Figure 4.42. Bandwidths of the UTC-PDs: (a) InGaAs/InGaAsP UTC-PDs (b) GaInAsSb/InP UTC-PD.

GHz to 47 GHz was observed for the studied geometries, as depicted in Figure 4.42 (a). The intrinsic bandwidth could then be determined using the calculated/extracted transit times using the compact model. Following this method, intrinsic bandwidths ranging from 45 GHz to 56 GHz were determined, indicating the detrimental impact of the pads and access lines on UTC-PD bandwidths.

The second set of measurements were performed at the IMS laboratory. The frequency-dependent photo-response of the UTC-PDs were measured in the range of 500 MHz to 67 GHz using a ModBox-VNA with a lithium niobate (LiNbO3) Mach-Zehnder modulator (MZM) at 1.55 µm and a ZVA vector network analyzer. The bandwidth measurements were performed after an RF power calibration of the two ZVA ports (ZVA+ RF cables). Once the measurements were completed, loss compensation for the RF probes was taken into account in data treatment. Figure 4.42 (b) shows a good agreement between the measurements and the compact model for the normalized bandwidth of the two UTC-PD technologies. The oscillations observed in the measurements can probably be attributed to multiple reflections between the different RF components (RF Cable and probes, ZVA, Modulator). These components were not calibrated, due to the lack of calibration kit, which probably resulted in these reflections.

It should be noted that for fitting the bandwidth characteristics, v_{th} was set to 2.5×10^7 cm/s and the v_{sat} was re-optimized for a value of 1.7×10^7 cm/s, which are higher than the values considered in the electric field-drift velocity model. The electric field values calculated at the collector input are always in the saturation zone of the electric field-drift velocity characteristics with the lowest value of ~16 kV/cm at zero bias. Moreover, the values reported in the literature (electric field-drift velocity characteristics) are for a particular mole fraction and doping. This slightly differs from what we are studying. Hence, the slight discrepancy in the drift velocity values were observed.

Figure 4.43 compares the on-wafer measurements of the normalized frequency photoresponse with the compact model simulations for InGaAs/InGaAsP UTC-PDs, showing different approximation methods discussed in chapter 2 related to the SPICE implementation of the photo-response. The simulation corresponding to the LPF approximation is also included in the graph for reference. As expected, the LPF approximation overestimates the cutoff frequency, while the Padé (1,1) approximation underestimates it. Interestingly, the Padé (2,1) and Padé (3,1) approximations show acceptable accuracy up to 67 GHz and start to deviate from the analytical solution beyond 110 GHz (as discussed in Chapter 2). Our proposed implementation offers the most accurate and optimal description of the photo-response, remaining accurate to the theorical model even beyond 110 GHz.

With respect to the photocurrent implementation, Figure 4.43 compares the InGaAs/InGaAsP UTC-PD normalized frequency photoresponse on-wafer measurements to the compact model simulations for different approximation methods. The simulation corresponding to the LPF approximation is also included for reference. As expected, the single pole LPF approximation overestimates the cutoff frequency, while the Padé (1,1) approximation underestimates it. Interestingly, the Padé (2,1) and Padé (3,1) approximations show acceptable accuracy up to 67 GHz and start to deviate from the analytical solution beyond 110 GHz (as discussed in Chapter 2). Our proposed implementation offers the most accurate and optimal description of the photoresponse, remaining accurate even beyond 110 GHz.

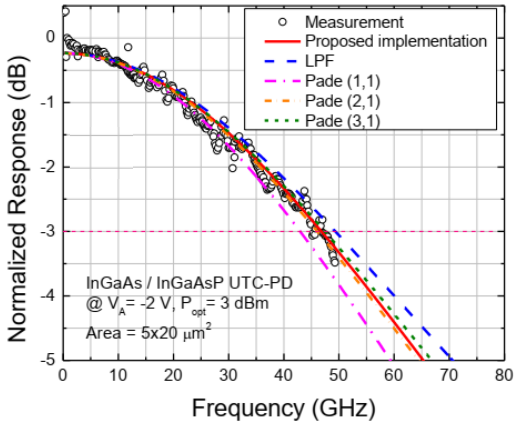

Figure 4.43. Measured (symbol) and simulated (line) normalized photo-response of InGaAs/InGaAsP UTC PD comparing different photocurrent implementations presented in this work.

For the optical characterization of the GaInAsSb/InP UTC-PDs, an optical signal (λ = 1.55 μm) of 3 dBm power, modulated by a Mach-Zehnder modulator (MZM) was used. Measurements were performed with a bias ranging from 0 to -2.5 V. Figure 4.44 (a)-(c) show an excellent agreement between the measurements and the model predictions over the entire frequency and voltage ranges. It should be noted that when fitting the bandwidth characteristics, v_{th} was set to 2×10^7 cm/s and the v_{sat} re-optimized for a value of 1×10^7 cm/s for this technology.

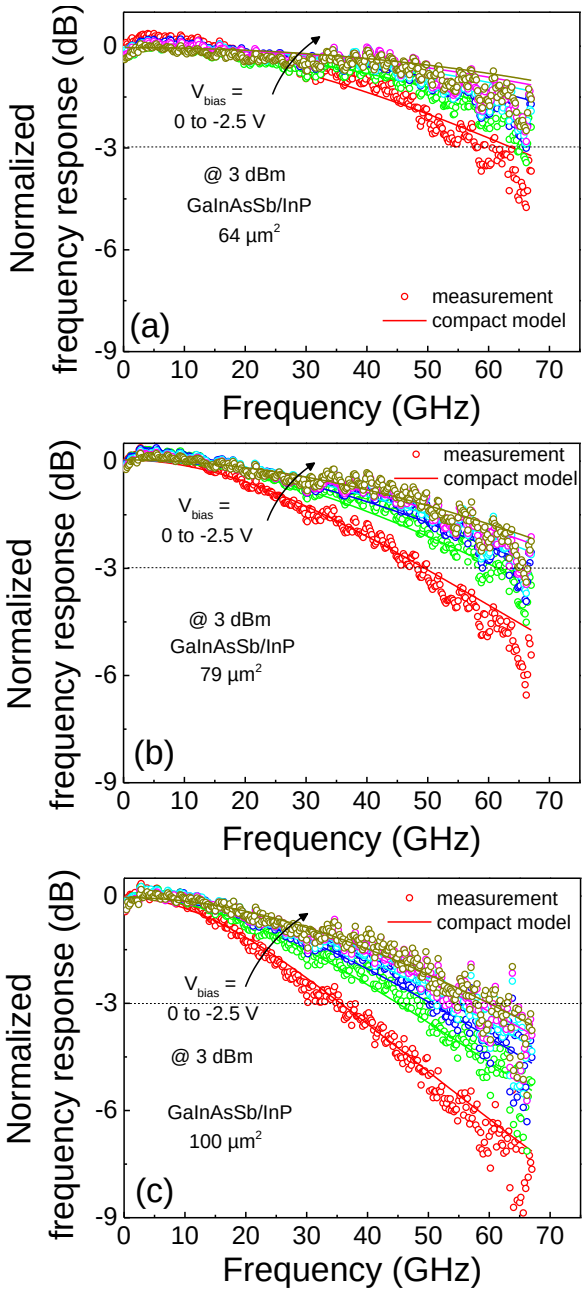

Figure 4.44. Measured (symbol) and simulated (line) normalized frequency response GaInAsSb/InP UTC-PD geometries with active areas of (a) 64 µm² (b) 79 µm² (c) 100 µm².

4.3 Conclusion

In this chapter, we present extensive validation of our compact model against measurements on three UTC-PD technologies under a wide range of operating conditions. Different de-embedding methods and a dedicated compact model parameter extraction flow proposed for UTC-PD have been described. Leveraging on-wafer measurement from various UTC-PD technologies and geometries, the validity of existing and new methods of de-embedding and parameter extraction strategies was demonstrated.

DC and RF behavior without illumination of the compact model have been validated against on-wafer measurements up to 67 GHz and 110 GHz on three UTC-PD technologies developed on the InP substrates. Next, bandwidth measurements, up to 67 GHz, were performed on UTC-PDs for the first time at the IMS laboratory and were also validated against the compact model simulation. The model has demonstrated excellent versatility and scalability for all three types of UTC-PDs under study across several geometries and under a wide range of bias conditions. The proposed modelling framework is comprehensive, accurate and physics-based while remaining compatible with the existing design infra-structure of the electronic circuits.

Conclusion

Conclusion

This PhD thesis work has focused on the development of the first compact model for ultrafast photodiodes to facilitate the co-design of monolithic photonic and nanoelectronic technologies.

Future communication systems should be capable of supporting the expected increase in data traffic. The literature review shows that monolithic integrated OEI circuits and systems seem to be a viable solution. Wide bandwidth, OEIC-based receivers are critical for optical communications. Low power, compact and efficient transceivers are essential in high efficiency wireless communications systems. In OEI circuits and systems, UTC-PDs are a key component. Relying only on electron transport, UTC-PDs demonstrate bandwidths of more than 600 GHz with good power levels [61].

The recent trend in OEIC research indicates that the electronic and photonic communities are looking for an efficient and unified solution to model both elementary devices and complex circuits and systems. As a first step towards the development of a unified modelling solution, we propose a scalable and physics-based compact model for the UTC-PDs. The model is written in Verilog-A and is compatible with existing electronic circuit design methodology/tool/flow. The model has been developed based on the charge carrier transport equations in UTC-PD. Unlike most of the existing small signal models of UTC-PDs reported in the literature, which are purely empirical, our compact model includes comprehensive description of the UTC PD device physics through physical equations, supported by arguments, capturing a wide range of physical phenomena governing the operation of UTC-PDs. As a result, our model also takes into account more material parameters such as doping density, mobility, permittivity as well as geometry scaling laws.

In particular, the dark current, which is a figure of merit governing the noise of the UTC-PDs, has been emphatically analyzed and modeled. Its origins are described by the phenomena of charge carrier diffusion, generation/recombination and tunneling effects. This investigation has shown that tunnel currents dominate the total current, especially at medium and high reverse bias. Additionally, the series resistance and junction capacitance of the UTC-PDs are crucial elements as they determine the R-C delay that characterizes the transient response of the UTC-PD (bandwidth and RF output power). In the case of integrated waveguide photodiodes, dependence of the series resistance on the geometrical as well as technological parameters such as the doping density and the specific resistivity of the metal contacts was determined. Similarly for the junction capacitance, the bias voltage dependence and scaling laws are explored and are accurately captured by the proposed compact model. We also developed the first accurate and physics-based implementation of the Verilog-A compact model of the full analytical form of the photocurrent in the UTC-PDs. The proposed implementation uses an optimal number of

three additional nodes in the equivalent electrical circuit of the UTC-PD offering the best compromise between accuracy (up to 300 GHz) and computational efficiency. The model in its entirety is therefore capable of accurately capturing the DC response, static photocurrent, unilluminated RF response and bandwidth of the UTC-PD.

After elaborating the analytical form of the compact model and implementation strategies, we presented an extensive validation of our model against measurements on three UTC-PD technologies under a wide range of operating conditions. We proposed new de-embedding methods adapted for our test structures and we also proposed a first detailed parameter extraction flow for UTC-PDs. The unilluminated DC and RF behavior of the compact model was validated against on-wafer measurements up to 67 GHz and 110 GHz on three UTC-PD technologies developed on InP substrates. Bandwidth measurements, up to 67 GHz, were performed on UTC-PDs for the first time in the IMS laboratory and were also validated against the compact model simulation. The model has demonstrated excellent versatility and scalability for all three types of UTC-PDs under study across several geometries and under a wide range of bias conditions. The proposed modelling framework is comprehensive, accurate and physics-based while remaining compatible with the existing design infra-structure of the electronic circuits.

Outlook

To begin with, the proposed model, de-embedding methods and parameter extraction techniques of this thesis can be extrapolated to other photodiode technologies (p-i-n PD for example). In the future scope of this work, further improvements can be made on the UTC-PD compact model. In addition, a few other aspects can be explored that could not be addressed in the scope of this thesis, as outlined in the following:

1. UTC-PDs are key components in OEICs because of their very high operating frequency and high RF output powers. High RF output power is desired for transmitting mm-Waves and THz signals over long distances and to improve the signal-to-noise ratio of the signals. Under these high-power operating conditions, the UTC-PDs can exhibit nonlinear behavior and generate output harmonics that affect performances of OEICs and cause signals distortions. Therefore, the linearity of UTC-PDs must be investigated and validated by the compact model under various operating conditions, namely bias voltage, modulation and optical power. In practice, the linearity analysis consists of injecting two optical signals modulated by two near-frequency sinusoids into the DUT. At the output, the distortion of the signals is characterized by the appearance of harmonics. The intercept point of the first and third order components, obtained by plotting the output power versus the input power, can be used to determine the figure of merit of the linearity called as the third order output intercept point (OIP3).

2. Since junction capacitance is a very important element that determines the performance of a UTC-PDs, the junction capacitance model must be further enhanced by modelling and implementation of the differential capacitance phenomenon that occurs at high photocurrents.

Indeed, at high photocurrent densities, an internal electric field induced by the space charge, appears and opposes to the bias-induced electric field. This space charge-induced electric field can be strong enough to collapse the bias-induced electric field and thus reduce the extension of the depletion region. As a result, this leads to a compression of the RF output power and reduced the bandwidth.

3. Thermal effects in UTC-PDs present a significant challenge under high power operation. The increase in temperature within the UTC-PDs reduces the mobility of the charge carriers and therefore increases the transit time which, in term, impacts the dynamic response. Also, rapid temperature increase can cause a thermal failure. In order to take the thermal effect into account, it is necessary to perform a detailed reliability study on the temperature distribution in the UTC-PDs for geometries of interest and in the case of high photocurrent densities. This can help better modelling of thermal effects and also to identify possible heat flow bottlenecks. Finally, experimental investigation are also needed to explored carefully.

4. OEI circuits and systems comprising of UTC-PDs are susceptible to operate at high frequencies and RF powers. Long distance transmission of RF signals generated by UTC-PDs requires amplification. Also, receiving modulated optical signals by an optical communication link using a UTC-PDs requires the conversion of the UTC-PD current into an amplified voltage to read and process the received data. A broadband TIA is the ideal candidate for this purposes. Therefore, a co-simulation study to optimize the operating points of the UTC-PD and the TIA using the same design tool could be a first step towards photonics and electronics co-simulation.

References

[1] P. J. Winzer, D. T. Neilson, and A. R. Chraplyvy, "Fiber-optic transmission and networking: the previous 20 and the next 20 years [Invited]," *Opt. Express*, vol. 26, no. 18, 2018.

[2] Y. Yue, Q. Wang, and J. Anderson, "Experimental investigation of 400 Gb/s data center interconnect using unamplified high-baud-rate and high-order QAM single-carrier signal," *Appl. Sci.*, vol. 9, no. 12, 2019.

[3] "IEEE P802.3bs 400 Gb/s Ethernet Task Force." [Online]. Available: www.ieee802.org/3/bs/.

[4] C. Mukherjee *et al.*, "Efficient compact modelling of UTC-photodiode towards terahertz communication system design," *Solid. State. Electron.*, vol. 170, no. April, p. 107836, Aug. 2020.

[5] U. Koch *et al.*, "A monolithic bipolar CMOS electronic–plasmonic high-speed transmitter," *Nat. Electron.*, vol. 3, no. 6, pp. 338–345, 2020.

[6] X. Pang *et al.*, "Bridging the Terahertz Gap: Photonics-Assisted Free-Space Communications From the Submillimeter-Wave to the Mid-Infrared," *J. Light. Technol.*, vol. 40, no. 10, 2022.

[7] T. Nagatsuma, G. Ducournau, and C. C. Renaud, "Advances in terahertz communications accelerated by photonics," *Nat. Photonics*, vol. 10, no. 6, pp. 371–379, Jun. 2016.

[8] D. Lee, H. Sasaki, H. Fukumoto, K. Hiraga, and T. Nakagawa, "Orbital Angular Momentum (OAM) multiplexing: An enabler of a new era of wireless communications," *IEICE Trans. Commun.*, vol. E100B, no. 7, 2017.

[9] C. Mukherjee *et al.*, "Towards Monolithic Indium Phosphide (InP)-Based Electronic Photonic Technologies for beyond 5G Communication Systems," *Appl. Sci.*, vol. 11, no. 5, p. 2393, Mar. 2021.

[10] Christophe Caillaud, "Photorecepteur intégré SOA-pin pour les applications à 100 gbit/s," TELECOM PARISTECH, 2010.

[11] G. Charlet, "Progress in optical modulation formats for high-bit rate WDM transmissions," *IEEE J. Sel. Top. Quantum Electron.*, vol. 12, no. 4, 2006.

[12] Guillaume Levaufre, "Circuits photoniques intégrés incluant des lasers hybrides iii-v sur silicium pour applications en télécommunication très haut débit," UNIVERSITÉ PARIS-SACLAY, 2016.

[13] "40 Gb/s and 100 Gb/s Fiber Optic Task Force." [Online]. Available: https://www.ieee802.org/3/bm/.

[14] Z. Xuan, R. Ding, Y. Liu, T. Baehr-Jones, M. Hochberg, and F. Aflatouni, "A Low-

Power Hybrid-Integrated 40-Gb/s Optical Receiver in Silicon," *IEEE Trans. Microw. Theory Tech.*, vol. 66, no. 1, 2018.

[15] L. M. Lunardi and S. Chandrasekhar, "Integrated p-i-n/HBT Photoreceivers for Optical Communications," in *Technical Digest - International Electron Devices Meeting, IEDM*, 1996.

[16] A. C. Carusone, H. Yasotharan, and T. Kao, "CMOS technology scaling considerations for multi-gbps optical receivers with integrated photodetectors," in *IEEE Journal of Solid-State Circuits*, 2011, vol. 46, no. 8.

[17] Longfei Shen, "Ultrafast photodetector on the InP-membrane-on-silicon platform," Technische Universiteit Eindhoven, 2016.

[18] W. Kuebart *et al.*, "Monolithically integrated InP-based PIN-HEMT receiver OEIC with a receiver-sensitivity of -19.2dBm at 10 Gbit/s," in *European Conference on Optical Communication, ECOC*, 1994.

[19] R. H. Walden *et al.*, "Broadband optoelectronic integrated receiver front-ends comprising InP-based heterojunction bipolar transistors and base-collector photodiodes," in *Conference on Optical Fiber Communication, Technical Digest Series*, 1994, vol. 4.

[20] L. M. Lunardi, S. Chandrasekhar, A. H. Gnauck, C. A. Burrus, and R. A. Hamm, "20 Gb/s monolithic p-i-n/HBT photoreceiver module for 1.55 μm applications," in *European Conference on Optical Communication, ECOC*, 1995, vol. 2.

[21] A. L. Gutierrez-Aitken, K. Yang, X. Zhang, G. I. Haddad, P. Bhattacharya, and L. M. Lunardi, "16-GHz Bandwidth InAlAs—InGaAs Monolithically Integrated p-i-n/HBT Photoreceiver," *IEEE Photonics Technol. Lett.*, vol. 7, no. 11, 1995.

[22] M. Bitter, R. Bauknecht, W. Hunziker, and H. Melchior, "Monolithic InGaAs-InP p-i-n/HBT 40-Gb/s optical receiver module," *IEEE Photonics Technol. Lett.*, vol. 12, no. 1, 2000.

[23] Vernon Elmo Paul, "Electro-Photonic Integration and Technology Selection for Next Generation Optical Receivers," McGill University, 2017.

[24] J. Michel, J. Liu, and L. C. Kimerling, "High-performance Ge-on-Si photodetectors," *Nat. Photonics*, vol. 4, no. 8, 2010.

[25] G. Masini, L. Colace, G. Assanto, H. C. Luan, and L. C. Kimerling, "High-performance p-i-n Ge on Si photodetectors for the near infrared: From model to demonstration," *IEEE Trans. Electron Devices*, vol. 48, no. 6, 2001.

[26] S. Assefa *et al.*, "A 90nm CMOS integrated Nano-Photonics technology for 25Gbps WDM optical communications applications," in *Technical Digest - International Electron Devices Meeting, IEDM*, 2012.

[27] R. Meade *et al.*, "Integration of silicon photonics in bulk CMOS," in *Digest of Technical Papers - Symposium on VLSI Technology*, 2014.

[28] S. Lischke *et al.*, “Monolithic photonic BiCMOS technology for high-speed receiver applications,” in *International Conference on Transparent Optical Networks*, 2017.

[29] H. Y. Jung *et al.*, “A monolithically integrated 25-gb/s optical receiver based on photonic bicmos technology,” in *2017 Conference on Lasers and Electro-Optics Pacific Rim, CLEO-PR 2017*, 2017, vol. 2017-January.

[30] K. Sengupta, T. Nagatsuma, and D. M. Mittleman, “Terahertz integrated electronic and hybrid electronic–photonic systems,” *Nat. Electron.*, vol. 1, no. 12, pp. 622–635, Dec. 2018.

[31] A. Nakamura, J. I. Nikaido, Y. Aoki, Y. Shirakata, and S. Takase, “High-efficiency low-phase-noise 79-GHz Gunn oscillator module,” in *European Microwave Week 2015: “Freedom Through Microwaves”, EuMW 2015 - Conference Proceedings; 2015 45th European Microwave Conference Proceedings, EuMC*, 2015.

[32] T. Maekawa, H. Kanaya, S. Suzuki, and M. Asada, “Oscillation up to 1.92 THz in resonant tunneling diode by reduced conduction loss,” *Appl. Phys. Express*, vol. 9, no. 2, 2016.

[33] H. Eisele, “Selective etching technology for 94 GHz GaAs IMPATT diodes on diamond heat sinks,” *Solid State Electron.*, vol. 32, no. 3, 1989.

[34] H. Eisele, “355 GHz oscillator with GaAs TUNNETT diode,” *Electron. Lett.*, vol. 41, no. 6, 2005.

[35] J. S. Rieh, D. Yoon, and J. Yun, “An overview of solid-state electronic sources and detectors for Terahertz imaging,” in *Proceedings - 2014 IEEE 12th International Conference on Solid-State and Integrated Circuit Technology, ICSICT 2014*, 2014.

[36] A. Khalid *et al.*, “Terahertz oscillations in an In0.53Ga0.47As submicron planar Gunn diode,” *J. Appl. Phys.*, vol. 115, no. 11, 2014.

[37] J. Wang, L. Wang, C. Li, B. Romeira, and E. Wasige, “28 GHz MMIC resonant tunnelling diode oscillator of around 1mW output power,” *Electron. Lett.*, vol. 49, no. 13, 2013.

[38] A. Al-Khalidi *et al.*, “Resonant Tunneling Diode Terahertz Sources with up to 1 mW Output Power in the J-Band,” *IEEE Trans. Terahertz Sci. Technol.*, vol. 10, no. 2, 2020.

[39] W. Zhang, E. Kasper, and J. Schulze, “An 82-GHz 14.6-mW Output Power Silicon Impact Ionization Avalanche Transit Time Transmitter with Monolithically Integrated Coplanar Waveguide Patch Antenna,” *IEEE Trans. Microw. Theory Tech.*, vol. 67, no. 1, 2019.

[40] A. M. Arabhavi *et al.*, “InP/GaAsSb Double Heterojunction Bipolar Transistor Emitter-Fin Technology with fMAX= 1.2 THz,” *IEEE Trans. Electron Devices*, vol. 69, no. 4, 2022.

[41] B. Heinemann *et al.*, “SiGe HBT with fx/fmax of 505 GHz/720 GHz,” in *Technical Digest - International Electron Devices Meeting, IEDM*, 2017.

[42] A. W. Mahmoud Mohamed, “Integrated photonics for millimetre wave transmitters and receivers,” College London, 2019.

[43] G. Liu, J. Jayamon, J. Buckwalter, and P. Asbeck, “Frequency doublers with 10.2/5.2 dBm peak power at 100/202 GHz in 45nm SOI CMOS,” in *Digest of Papers - IEEE Radio Frequency Integrated Circuits Symposium*, 2015, vol. 2015-November.

[44] T. Kuri and K. I. Kitayama, “Long-term stabilized millimeter-wave generation using a high-power mode-locked laser diode module,” *IEEE Trans. Microw. Theory Tech.*, vol. 47, no. 5, 1999.

[45] T. Wang, M. Chen, H. Chen, and S. Xie, “Millimeter-wave signal generation using four-wave mixing effect in SOA,” in *Optics InfoBase Conference Papers*, 2007.

[46] R. Mohamad, S. M. Idrus, A. S. Supaat, S. Yaakob, A. K. Zamzuri, and S. N. A. Sukito, “Millimeter wave carrier generation based on Brillouin fiber laser with improved tuning capability,” *Optik (Stuttg).*, vol. 125, no. 1, 2014.

[47] A. W. Mohammad *et al.*, “60-GHz transmission link using uni-traveling carrier photodiodes at the transmitter and the receiver,” *J. Light. Technol.*, vol. 36, no. 19, 2018.

[48] Kévin Froberger, “Caractérisation et modélisation de composants terahertz,” Université de Lille, 2019.

[49] M. Born and E. Wolf, *Principles of optics: electromagnetic theory of propagation, interference and Diffraction of Light*, 7th ed., vol. 1. 1999.

[50] M. Martin and E. R. Brown, “Critical comparison of GaAs and InGaAs THz photoconductors,” in *Terahertz Technology and Applications V*, 2012, vol. 8261.

[51] T. Nagatsuma, “Photonic generation of millimeter waves and its applications,” in *Optics InfoBase Conference Papers*, 2012.

[52] T. Nagatsuma *et al.*, “Terahertz wireless communications based on photonics technologies,” *Opt. Express*, vol. 21, no. 20, 2013.

[53] T. Kürner and S. Priebe, “Towards THz communications - Status in research, standardization and regulation,” *J. Infrared, Millimeter, Terahertz Waves*, vol. 35, no. 1, 2014.

[54] S. Koenig *et al.*, “Wireless sub-THz communication system with high data rate,” *Nat. Photonics*, vol. 7, no. 12, 2013.

[55] Y. Niu, Y. Li, D. Jin, L. Su, and A. V. Vasilakos, “A survey of millimeter wave communications (mmWave) for 5G: opportunities and challenges,” *Wirel. Networks*, vol. 21, no. 8, 2015.

[56] T. S. Rappaport *et al.*, “Millimeter wave mobile communications for 5G cellular: It will work!,” *IEEE Access*, vol. 1, 2013.

[57] I. F. Akyildiz, J. M. Jornet, and C. Han, “Terahertz band: Next frontier for wireless communications,” *Phys. Commun.*, vol. 12, 2014.

[58] A. Kanno, P. T. Dat, N. Yamamoto, and T. Kawanishi, “Millimeter-Wave Radio-Over-Fiber Network for Linear Cell Systems,” *J. Light. Technol.*, vol. 36, no. 2, 2018.

[59] T. Harter *et al.*, “Wireless THz link with optoelectronic transmitter and receiver,” *Optica*, vol. 6, no. 8, 2019.

[60] A. W. Mohammad, A. Jankowski, F. Van Dijk, and C. C. Renaud, “Optically Pumped Mixing in Photonically Integrated Uni-Travelling Carrier Photodiode,” in *International Conference on Infrared, Millimeter, and Terahertz Waves, IRMMW-THz*, 2018, vol. 2018-Septe.

[61] H. J. Song and T. Nagatsuma, *Handbook of terahertz technologies: Devices and applications*. 2015.

[62] H. J. Song, K. Ajito, Y. Muramoto, A. Wakatsuki, T. Nagatsuma, and N. Kukutsu, “Uni-travelling-carrier photodiode module generating 300 GHz power greater than 1 mW,” *IEEE Microw. Wirel. Components Lett.*, vol. 22, no. 7, 2012.

[63] T. Nagatsuma, T. Kurokawa, M. Sonoda, T. Ishibashi, M. Shimizu, and K. Kato, “600-GHz-band Waveguide-output Uni-traveling-carrier Photodiodes and Their Applications to Wireless Communication,” in *IEEE MTT-S International Microwave Symposium Digest*, 2018, vol. 2018-June.

[64] C. Castro *et al.*, “32 GBd 16QAM Wireless Transmission in the 300 GHz Band using a PIN Diode for THz Upconversion,” in *2019 Optical Fiber Communications Conference and Exhibition, OFC 2019 - Proceedings*, 2019.

[65] P. Rodriguez-Vazquez, J. Grzyb, B. Heinemann, and U. R. Pfeiffer, “A 16-QAM 100-Gb/s 1-M Wireless Link with an EVM of 17% at 230 GHz in an SiGe Technology,” *IEEE Microw. Wirel. Components Lett.*, vol. 29, no. 4, 2019.

[66] S. Jia *et al.*, “2 × 300 Gbit/s Line Rate PS-64QAM-OFDM THz Photonic-Wireless Transmission,” *J. Light. Technol.*, vol. 38, no. 17, 2020.

[67] I. Dan *et al.*, “A 300-GHz Wireless Link Employing a Photonic Transmitter and an Active Electronic Receiver with a Transmission Bandwidth of 54 GHz,” *IEEE Trans. Terahertz Sci. Technol.*, vol. 10, no. 3, 2020.

[68] S. Nellen *et al.*, “Coherent Wireless Link at 300 GHz with 160 Gbit/s Enabled by a Photonic Transmitter,” *J. Light. Technol.*, 2022.

[69] S. Jia *et al.*, “Integrated dual-laser photonic chip for high-purity carrier generation enabling ultrafast terahertz wireless communications,” *Nat. Commun.*, vol. 13, no. 1, 2022.

[70] C. C. Renaud, M. J. Fice, L. Ponnampalam, M. Natrella, C. Graham, and A. J. Seeds, “Uni-travelling carrier photodetectors as THz detectors and emitters,” in *Quantum Sensing and Nanophotonic Devices XII*, 2015, vol. 9370.

[71] E. Rouvalis, M. J. Fice, C. C. Renaud, and A. J. Seeds, “Millimeter-wave optoelectronic mixers based on uni-traveling carrier photodiodes,” *IEEE Trans. Microw. Theory Tech.*, vol. 60, no. 3 PART 2, 2012.

[72] F. Van Dijk *et al.*, “Integrated InP heterodyne millimeter wave transmitter,” *IEEE Photonics Technol. Lett.*, vol. 26, no. 10, 2014.

[73] T. Ishibashi, N. Shimizu, S. Kodama, H. Ito, T. Nagatsuma, and T. Furuta, “Uni-Traveling-Carrier Photodiodes,” in *Ultrafast Electronics and Optoelectronics*, 1997, p. UC3.

[74] T. Ishibashi and H. Ito, “Uni-traveling-carrier photodiodes,” *J. Appl. Phys.*, vol. 127, no. 3, p. 031101, Jan. 2020.

[75] T. Ishibashi *et al.*, “InP/InGaAs Uni-Traveling-Carrier Photodiodes,” *IEICE Trans. Electron.*, vol. E83-C, no. 6, 2000.

[76] H. Ito, T. Furuta, S. Kodama, N. Watanabe, and T. Ishibashi, “InP/InGaAs uni-travelling-carrier photodiode with 220 GHz bandwidth,” *Electron. Lett.*, vol. 35, no. 18, 1999.

[77] H. Ito, T. Furuta, S. Kodama, and T. Ishibashi, “InP/InGaAs uni-travelling-carrier photodiode with 310 GHz bandwidth,” *Electron. Lett.*, vol. 36, no. 21, 2000.

[78] S. Khanra, “Modeling of uni traveling carrier photodiode for wireless photonic transmitter,” University of Calcutta, 2017.

[79] H. Fukano, Y. Muramoto, K. Takahata, and Y. Matsuoka, “High efficiency edge-illuminated uni-travelling-carrier-structure refracting-facet photodiode,” *Electron. Lett.*, vol. 35, no. 19, 1999.

[80] T. Takeuchi, T. Nakata, K. Makita, and T. Torikai, “A high-power and high-efficiency photodiode with an evanescently coupled graded-index waveguide for 40 Gb/s applications,” in *Conference on Optical Fiber Communication, Technical Digest Series*, 2001, vol. 54, no. 3.

[81] M. Achouche *et al.*, “High Performance Evanescent Edge Coupled Waveguide Unitraveling-Carrier Photodiodes for >40-Gb/s Optical Receivers,” *IEEE Photonics Technol. Lett.*, vol. 16, no. 2, 2004.

[82] C. Caillaud *et al.*, “Ultra Compact High responsivity Photodiodes for >100 Gbaud Applications,” in *2021 European Conference on Optical Communication, ECOC 2021*, 2021.

[83] C. Li *et al.*, “High-responsivity vertical-illumination Si/Ge uni-traveling-carrier photodiodes based on silicon-on-insulator substrate,” *Sci. Rep.*, vol. 6, 2016.

[84] X. Lin *et al.*, “High performance waveguide uni-travelling carrier photodiode grown by solid source molecular beam epitaxy,” *Opt. Express*, vol. 27, no. 25, 2019.

[85] J. R. M. Hermann A. Haus, *Electromagnetic fields and energy*. Englewood Cliffs, N.J: Prentice-Hall, 1989.

[86] Ansys, “Calculating absorbed optical power,” 2022. [Online]. Available: https://optics.ansys.com/hc/en-us/articles/360034915673.

[87] C. Sorace-Agaskar, J. Leu, M. R. Watts, and V. Stojanovic, "Electro-optical co-simulation for integrated CMOS photonic circuits with VerilogA," *Opt. Express*, vol. 23, no. 21, p. 27180, Oct. 2015.

[88] H. Ito *et al.*, "High-power photonic millimetre wave generation at 100GHz using matching-circuit-integrated uni-travelling-carrier photodiodes," *IEE Proc. Optoelectron.*, vol. 150, no. 2, pp. 138–142, Apr. 2003.

[89] F. M. Kuo, T. C. Hsu, and J. W. Shi, "Strong bandwidth-enhancement effect in high-speed GaAs/AlGaAs based uni-traveling carrier photodiode under small photocurrent and zero-bias operation," in *Conference Proceedings - Lasers and Electro-Optics Society Annual Meeting-LEOS*, 2009.

[90] J. M. Wun, R. L. Chao, Y. W. Wang, Y. H. Chen, and J. W. Shi, "Type-II GaAs0.5Sb0.5/InP Uni-Traveling Carrier Photodiodes with Sub-Terahertz Bandwidth and High-Power Performance under Zero-Bias Operation," *J. Light. Technol.*, vol. 35, no. 4, 2017.

[91] J. M. Wun, C. H. Lai, N. W. Chen, J. E. Bowers, and J. W. Shi, "Flip-chip bonding packaged THz photodiode with broadband high-power performance," *IEEE Photonics Technol. Lett.*, vol. 26, no. 24, 2014.

[92] Y. Han *et al.*, "Distributed parameter circuit model for wideband photodiodes with inductive coplanar waveguide electrodes," *Chinese Opt. Lett.*, vol. 18, no. 6, 2020.

[93] M. Natrella *et al.*, "Accurate equivalent circuit model for millimetre-wave UTC photodiodes," *Opt. Express*, vol. 24, no. 5, 2016.

[94] D. Guendouz *et al.*, "Multiscale Compact Modelling of UTC-Photodiodes Enabling Monolithic Terahertz Communication Systems Design," *Appl. Sci.*, vol. 11, no. 23, p. 11088, Nov. 2021.

[95] M. E. Brinson and S. Jahn, "Qucs: A GPL software package for circuit simulation, compact device modelling and circuit macromodelling from DC to RF and beyond," *Int. J. Numer. Model. Electron. Networks, Devices Fields*, vol. 22, no. 4, pp. 297–319, Jul. 2009.

[96] M. Schroter, A. Pawlak, and A. Mukherjee, "HICUM/L2 A geometry scalable physics-based compact bipolar transistor model," 2017.

[97] T. Nardmann, M. Schroter, and P. Sakalas, "A Multiregion Approach to Modeling the Base-Collector Junction Capacitance," *IEEE Trans. Electron Devices*, vol. 63, no. 9, 2016.

[98] C. Mukherjee *et al.*, "Scalable Compact Modeling of III–V DHBTs: Prospective Figures of Merit Toward Terahertz Operation," *IEEE Trans. Electron Devices*, vol. 65, no. 12, pp. 5357–5364, Dec. 2018.

[99] Rosenbaum Tommy, "u shaped junction capacitance and poposal for diode CMC model enhancemnts," 2018.

[100] K. M.C.J.C.M, "Fabrication and characterization of metal-semiconductor contacts for

application in AlxGa1-xN/GaN HEMTs," Eindhoven University of Technology, 2000.

[101] M. Natrella *et al.*, "Modelling and measurement of the absolute level of power radiated by antenna integrated THz UTC photodiodes," *Opt. Express*, vol. 24, no. 11, 2016.

[102] E. F. Chor, W. K. Chong, and C. H. Heng, "Alternative (Pd,Ti,Au) contacts to (Pt,Ti,Au) contacts for In0.53Ga0.47As," *J. Appl. Phys.*, vol. 84, no. 5, 1998.

[103] S. Jain, M. Sysak, M. Swaidan, and J. Bowers, "Silicon fab-compatible contacts to n-InP and p-InGaAs for photonic applications," *Appl. Phys. Lett.*, vol. 100, no. 20, 2012.

[104] M. Cooke, "Making III-V contact with silicon substrates," *Semicond. Today Compd. Adv. Silicon*, vol. 6, no. 3, 2011.

[105] A. Bengi, S. J. Jang, C. I. Yeo, T. Mammadov, S. Özçelik, and Y. T. Lee, "Au and non-Au based rare earth metal-silicide ohmic contacts to p-InGaAs," *Solid. State. Electron.*, vol. 61, no. 1, 2011.

[106] A. Katz, B. E. Weir, and W. C. Dautremont-Smith, "Au/Pt/Ti contacts to p-In0.53Ga0.47As and n-InP layers formed by a single metallization common step and rapid thermal processing," *J. Appl. Phys.*, vol. 68, no. 3, 1990.

[107] C. Kopf, G. Kaiblinger-Grujin, H. Kosina, and S. Selberherr, "Influence of dopant species on electron mobility in InP," in *Conference Proceedings - International Conference on Indium Phosphide and Related Materials*, 1997.

[108] R. Kraus, K. Hoffmann, and H. J. Mattausch, "A precise model for the transient characteristics of power diodes," in *PESC Record - IEEE Annual Power Electronics Specialists Conference*, 1992.

[109] S. M. Sze and K. K. Ng, *Physics of Semiconductor Devices*. 2006.

[110] A. Schmidt, S. Dreiner, H. Vogt, A. Goehlich, and U. Paschen, "Analytical model for thin-film SOI PIN-diode leakage current," *Solid. State. Electron.*, vol. 130, 2017.

[111] J. Xu, X. Chen, W. Wang, and W. Lu, "Extracting dark current components and characteristics parameters for InGaAs/InP avalanche photodiodes," *Infrared Phys. Technol.*, vol. 76, 2016.

[112] ioffe, "Indium Phosphide," 2022. [Online]. Available: http://www.ioffe.ru/SVA/NSM/Semicond/InP/bandstr.html.

[113] S. R. Forrest, R. F. Leheny, R. E. Nahory, and M. A. Pollack, "In0.53Ga0.47As photodiodes with dark current limited by generation-recombination and tunneling," *Appl. Phys. Lett.*, vol. 37, no. 3, 1980.

[114] R. K. Ahrenkiel, R. Ellingson, S. Johnston, and M. Wanlass, "Recombination lifetime of In0.53Ga0.47As as a function of doping density," *Appl. Phys. Lett.*, vol. 72, no. 26, 1998.

[115] A. J. Scholten, G. D. J. Smit, M. Durand, R. Van Langevelde, and D. B. M. Klaassen, "The physical background of JUNGAP2," *IEEE Trans. Electron Devices*, vol. 53, no. 9, 2006.

[116] M. Verdun *et al.*, "Dark current investigation in thin P-i-N InGaAs photodiodes for nano-resonators," *J. Appl. Phys.*, vol. 120, no. 8, p. 084501, Aug. 2016.

[117] F. Pavanello, "Uni-travelling carrier photodiodes and metal mesh filters based on sub-wavelength apertures for THz applications," Université de Lille, 2013.

[118] E. N. Ivanov, S. A. Diddams, and L. Hollberg, "Study of the excess noise associated with demodulation of ultra-short infrared pulses," *IEEE Trans. Ultrason. Ferroelectr. Freq. Control*, vol. 52, no. 7, 2005.

[119] S. Lischke *et al.*, "Ultra-fast germanium photodiode with 3-dB bandwidth of 265 GHz," *Nat. Photonics*, vol. 15, no. 12, 2021.

[120] A. M. Arabhavi *et al.*, "Type-II GaInAsSb/InP Uniform Absorber High Speed Uni-Traveling Carrier Photodiodes," *J. Light. Technol.*, vol. 39, no. 7, pp. 2171–2176, Apr. 2021.

[121] P. Latzel *et al.*, "Generation of mW Level in the 300-GHz Band Using Resonant-Cavity-Enhanced Unitraveling Carrier Photodiodes," *IEEE Trans. Terahertz Sci. Technol.*, vol. 7, no. 6, 2017.

[122] H. Padé, "Sur la représentation approchée d'une fonction par des fractions rationnelles," *Ann. Sci. l'École Norm. supérieure*, vol. 9, 1892.

[123] L. F. Eastman, S. Tiwari, and M. S. Shur, "Design criteria for GaAs MESFETs related to stationary high field domains," *Solid. State. Electron.*, vol. 23, no. 4, pp. 383–389, Apr. 1980.

[124] K. Technologies, "N5260A Millimeter Head Controller Operation and Service Guide." .

[125] A. Rumiantsev and R. Doerner, "RF probe technology: History and selected topics," *IEEE Microw. Mag.*, vol. 14, no. 7, 2013.

[126] D. F. Williams *et al.*, "Calibrations for millimeter-wave silicon transistor characterization," *IEEE Trans. Microw. Theory Tech.*, vol. 62, no. 3, 2014.

[127] Thorlabs, "Thorlabs," 2022. [Online]. Available: https://www.thorlabs.com/.

[128] I. F. OPTIQUES, "IDIL FIBER OPTIQUES," 2022. [Online]. Available: https://www.idil-fibres-optiques.com/fr/.

[129] F. Factor, "Form Factor," 2022. [Online]. Available: https://www.formfactor.com/product/probes/specialty/light-wave-probe/.

[130] J. Švarný, "Analysis of quadrature bias-point drift of Mach-Zehnder electro-optic modulator," in *BEC 2010 - 2010 12th Biennial Baltic Electronics Conference, Proceedings of the 12th Biennial Baltic Electronics Conference*, 2010.

[131] P. Dherbecourt, O. Latry, E. Joubert, P. Dibin, and M. Ketata, "Achieving of an optical very high frequency modulated wave source using heterodyne technique," *Opt. Commun.*, vol. 202, no. 1–3, 2002.

[132] O. Latry, G. Ducournau, P. Dherbécourt, E. Joubert, and M. Kétata, “Experimental considerations on bandwidth measurement of ultra-fast photoreceptors by optical heterodyning,” *Meas. J. Int. Meas. Confed.*, vol. 40, no. 4, 2007.

[133] M. C. A. M. Koolen, “On-wafer high-frequency device characterization,” *Microelectron. Eng.*, vol. 19, no. 1–4, pp. 679–686, Sep. 1992.

[134] H. Xu and E. Kasper, “A de-embedding procedure for one-port active mm-wave devices,” in *2010 10th Topical Meeting on Silicon Monolithic Integrated Circuits in RF Systems, SiRF 2010 - Digest of Papers*, 2010.

[135] Milnes A.G and Feucht D.L., *Heterojunctions and Metal Semiconductor Junctions*. Elsevier, 1972.

[136] M. Anagnosti *et al.*, “Optimized High Speed UTC Photodiode for 100 Gbit/s Applications,” *IEEE J. Sel. Top. Quantum Electron.*, vol. 20, no. 6, pp. 29–35, Nov. 2014.

[137] A. Davidson, K. Jones, and E. Strid, “LRM and LRRM Calibrations with Automatic Determination of Load Inductance,” in *36th ARFTG Conference Digest*, 1990, pp. 57–63.

[138] “SemiconductorsDataBase,” 2022. [Online]. Available: http://www.ioffe.ru/SVA/NSM/Semicond/.

List of Publication

Journal paper

1. **D. Guendouz**, C. Mukherjee, M. Deng, M. De Matos, C. Caillaud, H. Bertin, A. Bobin, N. Vaissière, K. Mekhazni, F. Mallecot, A.M. Arabhavi, R. Chaudhary, O. Ostinelli, C. Bolognesi, P. Mounaix and C. Maneux., "Multiscale Compact Modelling of UTC-Photodiodes Enabling Monolithic Terahertz Communication Systems Design". Appl. Sci. 2021, 11, 11088. doi: 10.3390/app112311088.

2. C. Mukherjee, M. Deng, V. Nodjiadjim, M. Riet, C. Mismer, **D. Guendouz**, C. Caillaud, H. Bertin, N. Vaissiere, M. Luisier, X. Wen, M. De Matos, P. Mounaix and C. Maneux., "Towards Monolithic Indium Phosphide (InP)-Based Electronic Photonic Technologies for beyond 5G Communication Systems". Appl. Sci. 2021, 11, 2393. doi: 10.3390/app11052393.

International conference

1. **D. Guendouz**, M. Deng, C. Mukherjee, C. Caillaud, P. Mounaix, M. De Matos and C. Maneux., "Access Modelling-based De-embedding Method for High-frequency Characterization of Uni-traveling carrier Photodiodes," 2021 51st European Microwave Conference (EuMC), 2022, pp. 401-404. doi: 10.23919/EuMC50147.2022.9784170.

Appendix A

UTC-PD compact model Verilog-A code: tunneling currents and photocurrent

```
module photodiode (Anode, Cathode, Light);

inout Anode, Cathode Light;
electrical Anode, Cathode, Light;

electrical n1, n2; //Virtual nodes
electrical x1, x2, x3; // Virtual nodes for photocurrent implementation

// Virtual branches
branch (Cathode, n1) Rs_branch;  // Rs branch
branch (n1,n2)       RN_branch;   // RN  branch
branch (n2, Anode)   PD_branch ; // UTC-PD currents branch
branch (Light)       br_light ; // UTC-PD CURRENTS
// Photocurrent branches
branch (x1) br_bx1;
branch (x2) br_bx2;
branch (x3) br_bx3;
...
`define attr(txt)

// Model parameters
...
parameter real epsColl =9.2 from [1e-6:inf] `attr(info="Collector permitivity" uni t="A/W")
;
parameter real Mr=0.5 from [1e-6:inf]            `attr(info="grading coefficient");
parameter real Responsivity=0.5 from [1e-6:inf] `attr(info=" responsivity" uni t="A/W") ;
parameter real WA = 100e-9 from [0:inf]    `attr(info="Absorber thickness");
parameter real WC = 225e-9 from [0:inf]    `attr(info="Collector thickness");
parameter real mu = 0.5 from [0:inf]       `attr(info="e mobility in m²/Vs");
parameter real vth = 2.5e5 from [0:inf]  `attr(info="thermionic emission velocity in m/s");
parameter real vsat = 1e5 from [0:inf]    `attr(info="saturation velocity in m/s") ;
parameter real Escale= 3.3e5 from [0:inf] `attr(info="E-vc relationship parameter in v/m")
;
parameter real A_EField= 9.8e-7 from [0:inf] `attr(info="E-vc relationship parameter") ;
parameter real t_EField= 27.9 from [0:inf] `attr(info=" E-vc relationship parameter") ;

...
real Area, Vj_T2, Fmax, IBTB, ITAT, If;
real tauA, tauC, Iph, Popt, De;
real Cjci //Junction capacitance calculated from HiCuM/L2
...

analog begin

// active region Area
Area=(W+DeltaW)*(L+DeltaL);

// Electric field in the collector input
Fmax=(Cjci /(epsColl*8.854E-12))*((pow(Vj_T2,Mr))*pow((Vj_T2-V(PD_branch),1-Mr))/(1-Mr);

// Reverse current contributions
...
ITAT=(V(PD_branch) <= con1) ? Area*ATAT*Fmax* V(PD_branch)*limexp(-BTAT/Fmax):0;
IBTB=(V(PD_branch) <= con1) ? Area*ABTB*pow(Fmax,2)*( V(PD_branch))*limexp(-BBTB/Fmax):0
;
...
// Forward diode current
...
If = forward diode current equations;
...
// All dark current
Id=If+ ITAT+ IBTB+...;
...
```

```
...
// Photocurrent calculation
De=mu*0.026;
tauA=WA*WA/(3*De)+WA/vth;
...

vc   =   vsat*(1+((Fmax/Escale)-1)/(1+A_EField*pow((Fmax/Escale),t_EField)));   //Electric
field vs electron drift velocity
tauC=WC/vc;

Popt = pow(10, 0.1*V(br_light))/1000; // dB to Watt conversion for input optical power
Iph=Popt*Responsivity;
...
// Single pole calculations
I(br_bx1)<+-Iph;
I(br_bx1)<+V(br_bx1);
I(br_bx1)<+ddt(tauA*V(br_bx1));

// Implementation of sinc(w*tauc/2)*exp(-jw*tauc/2): Proposed model

I(br_bx2)<+-V(br_bx1)+V(br_bx3);
I(br_bx2)<+ddt((tauC/2)*V(br_bx2));

I(br_bx3)<+-V(br_bx2);
I(br_bx3)<+V(br_bx3);
I(br_bx3)<+ddt((tauC/6)*V(br_bx3));
...

// photocurrent branch
I5=V(br_bx3);

// CURRENT CONTRIBUTION
...
I(PD_branch)<+Id ; //Diode forward current
I(PD_branch)<+-I5 ; //Photocurrent
...
end
endmodule
```